Exploring the Origin of Coronal Mass Ejection Plasma from In Situ Observations of Ionic Charge State Composition

by

Jacob R. Gruesbeck

A dissertation submitted in partial fulfillment
of the requirements for the degree of
Doctor of Philosophy
(Atmospheric, Oceanic, and Space Sciences)
in The University of Michigan
2013

Doctoral Committee:

- Associate Research Scientist Susan T. Lepri, Co-Chair
- Professor Thomas H. Zurbuchen, Co-Chair
- Associate Professor Michael Liemohn
- Professor Gregory Tarlé
- Research Scientist Eric R. Christian, NASA Goddard Space Flight Center

For my loving and supportive family.

ACKNOWLEDGEMENTS

I would like to begin by thanking my two advisors at the University of Michigan, Thomas Zurbuchen and Susan Lepri for providing me with the opportunity to work with the Solar and Heliospheric Research Group and for their constant support and guidance in conducting the work in this dissertation. I would also like to thank Eric Christian, my advisor through the NASA Graduate Student Research Program, for providing me guidance as well as a place to work so I could follow my wife to Washington, D.C.

I would also like to thank the other two members of my dissertation committee, Michael Liemohn and Gregory Tarlé, for serving on my committee and the evaluation of this dissertation.

I would like to thank all the members of the Solar Heliospheric Research Group for the support through my graduate studies. Jim Raines for first working with me while I was still an undergrad, Jason Gilbert for this great LaTeXtemplate, Jon Thomas for the countless computer questions, Len Fisk for the insights and help with my AGU talk, and all the students from the group Dan, Gina, Liang, Micah, Aleida, Mark, and Pat, for the support with class, research, and stress.

I would like to thank all the administrative staff at the AOSS department, Deborah Eddy, Bryan White, Margaret Reid, Sandra Pytlinski, and Rick Baker just to name a few. You all have always been able to answer any question about the program or at least point me in the right direction.

Finally, I would like to thank all of my friends and family. My wife Sarah for

always supporting me and never giving up on me. My parents for believing in me and everything else they've done. I don't think there are anymore degrees for me to go after. Matt Trantham and Mike Grosskopf for helping me more than they probably know. And all my other friends I've made in my eleven years at the University. Kevin R., Ahmed, Kristin, Colin, Paul, Jim F., Jim H., Steve, Drewie, Kevin Z., and anyone I'm forgetting always remember to go blue!

This work was supported, in part, by the NASA Graduate Student Research Program grant NNX10AM41H, the *ACE* mission 44A-1085637 and NASA grants NNX07AB99G, NNX08AI11G, NNX08AM64G, and NNX10AQ61G. We used the SOHO/LASCO CME catalog developed by NASA, NRL and the Catholic University of America. SOHO is a project of international cooperation between ESA and NASA.

TABLE OF CONTENTS

CHAPTER

LIST OF FIGURES

Figure

LIST OF TABLES

ABSTRACT

Exploring the Origin of Coronal Mass Ejection Plasma from In Situ Observations of Ionic Charge State Composition

by

Jacob R. Gruesbeck

Co-Chairs: Susan T. Lepri and Thomas H. Zurbuchen

Solar wind ionic composition measurements are powerful tools in discriminating between different sources of solar wind as well as identifying interplanetary coronal mass ejections (ICMEs). First, we present a new charge state evolution model which estimates the coronal electron environment from *in situ* ionic composition measurements. The coronal electron profile is not well measured, as direct observations are difficult to obtain due to the extreme heat and radiation near the sun. Using this model, we show that the unique bi-modal charge states, observed in the iron charge state distribution, may be a direct result of the heating and expansion characteristics of a coronal mass ejection (CME). We next turn our attention to very cool charge states which are sometimes observed concurrently with hot charge states during ICMEs. We show that these observations are a result of simultaneous observations of hot plasma and the remnants of an embedded prominence within the same ICME.

We then use the charge state distribution to explore the origin of suprathermal plasma observed during ICMEs. Suprathermal plasma is known to be an important seed population for solar energetic particles (SEPs) which are accelerated at the

CME-driven shock, but the plasma which is being accelerated to the suprathermal energies is not well understood. Using *in situ* measurements from the Suprathermal Ion Composition Spectrometer (STICS) onboard the Wind spacecraft and the Solar Wind Ion Composition Spectrometer (SWICS) on the Advanced Composition Explorer (ACE), we compare the suprathermal ionic composition to the bulk solar wind plasma during ICMEs. We present a comparison of suprathermal iron and oxygen to the co-located bulk plasma distribution during ICMEs as well as the bulk plasma upstream of the CME-driven shock. This is one of the first studies to present the suprathermal composition of heavy ions observed in ICME plasma. We find that there is a strong correlation between the suprathermal plasma and the co-located bulk plasma and not with the upstream bulk plasma. This implies a local acceleration mechanism is energizing the local bulk plasma to suprathermal energies and not due to shock acceleration acting on the heliospheric plasma upstream of the ICME.

CHAPTER I

Introduction

Ionic composition is one of the most fundamental properties of plasmas and energetic particles in the heliosphere. Compositional characteristics provide information about the origin, and transport properties of plasmas. Additionally, compositional differences provide unique patterns to identify the relative importance of the physical process at work (*Geiss et al.*, 1995; *Dayeh et al.*, 2009; *Hill et al.*, 2009). It is particularly important to apply compositional signatures to tools to the origins of space weather - perturbations originating from massive ejections of plasmas and magnetic field from the Sun, and also the origin of solar energetic particles (*Lepri et al.*, 2001; *Tylka et al.*, 2005; *Zurbuchen and Richardson*, 2006). Using these unique capabilities provided from the ionic composition of plasma we will explore the early coronal environment associated with heliospheric transients as well as investigate the potential seed population of energetic particles.

1.1 Coronal Mass Ejections

Coronal Mass Ejections (CMEs) are the rapid and explosive eruptions of coronal plasma entrenched in magnetic field. They are massive events which can act as a significant loss mechanism of plasma and magnetic flux from the Sun (*Low*, 1996; *Webb and Howard*, 2012, and references therein). For a CME to escape the gravitational pull of the Sun, they require a great deal of energy. Large Angle Spectroscopic Coronograph (LASCO) (*Brueckner et al.*, 1995) observations have shown that erupting CMEs can have an average initial energy of $\sim 10^{29}$ ergs (*Vourlidas et al.*, 2010). A CME most likely receives this energy from the solar magnetic field. Flux emergence and surface flow can act to stress the stable equilibrium of a local magnetic flux rope, which if stressed enough can lead to an explosive ejection of coronal plasma (*Forbes et al.*, 2006). Their rate of occurrence is directly tied to the solar cycle, with ejections occurring nearly 10 times more frequently during solar maximum than near solar minimum (*Gopalswamy et al.*, 2004). Their release may actually be tied to the solar cycle variation, through the more tangled and complex magnetic fields observed during solar maximum (*Riley et al.*, 2006; *Owens et al.*, 2008).

CMEs have been remotely observed erupting from the sun since the early 1970's, by early coronagraph observations from *Skylab* (*MacQueen et al.*, 1980, 1974). Since then, CMEs have been further investigated using remote observations from a variety of instruments on board the Solar and Heliospheric Observatory (SOHO) (*Dere et al.*, 1997; *Wiik et al.*, 1997), Solar Terrestrial Relations Observatory (STEREO) (*Harrison et al.*, 2008) and the Solar Dynamics Observatory (SDO) (*Patsourakos et al.*, 2010), all measuring the emissions from a vast array of wavelengths. White-light observations of CMEs have also been produced from instruments such as the LASCO, as seen in figure 1.1. From all of these different remote measurements, it has been seen that CMEs are closely associated with enhanced plasma heating and energization during their ejection from the corona. Additionally, heating of the CME plasma is also further observed in the extreme ultraviolet (EUV) and soft X-ray emissions (*Krucker et al.*, 2010). This heating is often related back to flares, which can occur during and immediately after the eruption (*Harrison*, 1995; *Vršnak et al.*, 2005), as well as the reconnection processes occurring back at the Sun (*Lynch et al.*, 2004). Energetic particles produced from these events are often observed in the observations of soft

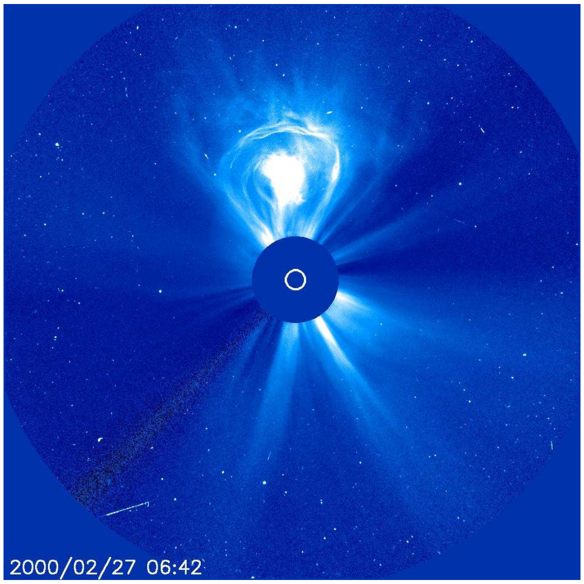

Figure 1.1: LASCO C3 coronagraph showing the three part structure of a CME. Noticeable in the image is the bright leading front, the dark cavity, and the bright core in the center of the ejecta. Adapted from similar figure in *Riley et al.* (2008).

X-rays (*Dauphin et al.*, 2006), hard X-rays (*Goff et al.*, 2005; *Temmer et al.*, 2010), and gamma-rays (*Lin et al.*, 2003).

CMEs are often observed to have three distinct components when observed in coronagraph images. For example, the CME observation shown in figure 1.1, shows the bright leading front, the dark cavity, and the bright core (*Illing and Hundhausen*, 1986, 1985). The bright front may be composed of the compressed plasma that has been swept up by the ejecta or was present in overlying magnetic fields above a flux rope before the eruption. Once ejected, the CME pushes this surrounding plasma out with it, compressing it as more and more plasma piles up in front of the event. The dark cavity is a region with very little plasma and dominated by strong magnetic field. The cavity may be the result of an entrenched flux rope in the CME. Finally, the bright core is a dense plasma dominated by very cool temperatures. Often, this feature is interpreted as embedded prominence material confined in the CME (*Rouillard*, 2011, and references therein). This three-part structure is observed in nearly $\sim 70\%$ of all

CMEs observed in coronagraphs (*Munro et al.*, 1979; *Webb and Hundhausen*, 1987; *Gopalswamy et al.*, 2003).

Prominences have been observed to erupt along with CMEs in Thompson-scattered white-light coronagraphs (e.g. *Gosling et al.*, 1974). Solar prominences are large loop-like structures, with lengths up to 100,000 km or more, that can be suspended above the Sun for long periods of time, sometimes up to months. Even though they are suspended in the hot coronal environment, they are observed to radiate in visible light, indicative of cool plasma and even neutral gas (*Tandberg-Hanssen*, 1995). During eruption, the prominences have been observed to undergo heating (*Ciaravella et al.*, 1997, 2001), but are still observed to exhibit very low-charge ions in remote observations out to 3.5 solar radii (*Akmal et al.*, 2001; *Ciaravella et al.*, 2003). Prominences are believed to be an important component for the eruption process for some CMEs. One eruption model describes prominence as a gravitational anchor, preventing the magnetic flux rope from erupting (*Low et al.*, 1982; *Low*, 1999). Gravitational forces will act to drain the plasma from the prominence, disrupting the force balance between the gravitational anchor of the prominence and the magnetic tension force from the flux rope. The flux rope can then violently eject from the corona dragging the prominence with it (*Low et al.*, 2003). Other models suggest that prominences form around neutral lines, where the surrounding magnetic field is highly sheared (*Aulanier et al.*, 2000; *Karpen et al.*, 2001). Prominence plasma is then confined along these neutral lines, which they then call filament channels. When reconnection occurs, during the eruption of the CME, closed magnetic fields in the corona reconnects with the filament channel allowing the prominence plasma to flow along the field lines of the ejecting flux rope (*Lynch et al.*, 2004).

1.2 Ionic composition of CME Plasma

Ionic-composition measurements are critical in the exploration of coronal plasma escaping into the heliosphere. The ionic composition of a plasma describes the distribution of ions over all possible charge states throughout a given atomic species. A particle in the corona can have its ionization state altered in a number of ways. An ion can become ionized by collisional ionization, wherein an electron from the ion's outer shell is lost when it collides with free electrons in the plasma, and excitation autoionization, where an electron from the outermost shell is lost due to the relaxation of an inner shell electron (*Cowan and Mann*, 1979; *Hundhausen et al.*, 1968). The ion can also recombine with free electrons in the plasma through either radiative or dielectric recombination (*Hundhausen et al.*, 1968; *Ko et al.*, 1997). The efficiency of any of these processes is dictated by the density of the free electron pool and the ionization and recombination reaction rates, which are dependent on the temperature of the electrons (*Mazzotta et al.*, 1998). When determining the full charge-state distribution of the plasma, photo-ionization can be neglected as it generally only plays a significant role for singly charged ions (*Marsch et al.*, 1995).

Very low in the corona, the time-scales for both recombination and ionization are much shorter than the expansion time-scales of the plasma. The expansion time-scale of the plasma describes the length of time a parcel of plasma has to adapt to the local thermal environment. When the atomic physics scales are much shorter, then the ions are approximately in ionization equilibrium, meaning the ionic distribution would reflect the local electron temperature. However, as the plasma propagates further away from the corona, its flow velocity begins to increase and the volume expands, which in turn causes the density to rapidly decrease. This reduction in density leads to an increase in the ionization and recombination time scales, meaning the plasma takes a longer time to adapt to the surrounding plasma. At the point when the plasma expands faster than its ionization states can adapt to the thermal

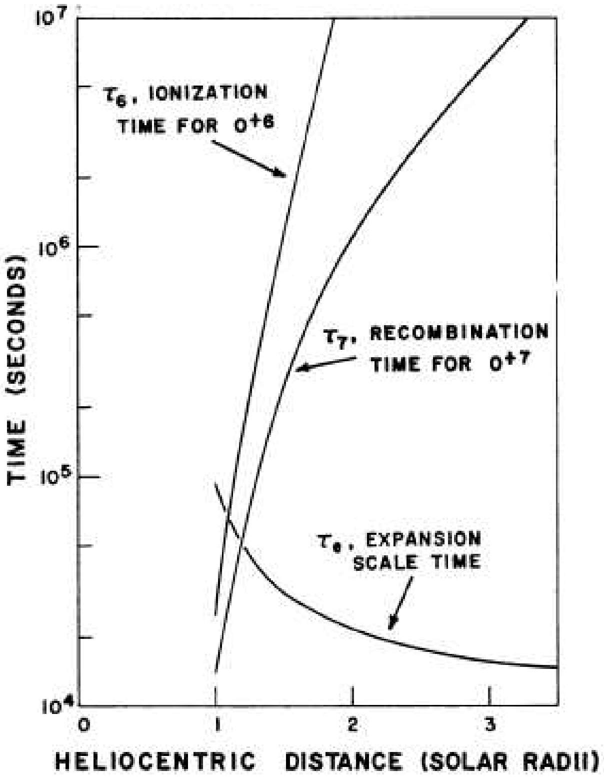

Figure 1.2: Illustration of the ionization, τ_6, recombination, τ_7, and expansion, τ_{e}, timescales for O^{6+}. The freeze-in location occurs when the expansion time scale becomes smaller than the recombination time scale. Figure published in *Hundhausen et al.* (1968).

environment, the plasma is said to become frozen-in. After this point, the charge state distribution remains static (*Hundhausen et al.*, 1968). Due to the inherent atomic difference of each element, the freeze-in height can vary widely, but generally occurs within the first 5 solar radii (*Hundhausen et al.*, 1968; *Hundhausen*, 1972; *Bame et al.*, 1974; *Buergi and Geiss*, 1986; *Geiss et al.*, 1995).

As previously mentioned, once the plasma has become frozen-in, the charge state distribution no longer evolves as the plasma propagates through the heliosphere. This enables *in situ* measurements of the charge state distribution to be used as a probe of the coronal atmosphere, over regions that are not always able to be directly observed. The relative abundance of an ionic species is dictated by the temperature and density of the surrounding electrons. By taking the ratio of the observed *in situ* density of two adjacent ionization states, we can obtain an estimate of the electron temperature at the freeze-in height of the ions by comparing the ionization and recombination rates. This is a reasonable assumption in the low corona, when the expansion of the plasma takes a long time and the ions are able to fully adapt to the surrounding environment. For example, if the *in situ* measurements consist of higher charge states, then this implies that the plasma originated from a hotter coronal environment, causing the increased amount of ionization. If, however, the charge states are lower than usual, then this could imply cooler temperatures. The ionic composition is a powerful tool in understanding the plasma environment of the low corona, which aids to further investigate the acceleration and heating mechanisms of the solar wind as well as the origination of the heliospheric transients.

The flow velocity of a plasma dictates the expansion timescale, thereby playing a critical role in the evolution of the plasma's charge state distribution. The expansion timescale describes the amount of time that the plasma has to adjust to the surrounding electron environment. When the plasma expands slowly from the corona due to a small flow velocity, the plasma will be able to fully adapt to the surrounding environment. However, when the flow velocity is large, enabling a fast expansion, the plasma is not capable of fully adapting, eventually causing the charge state distribution to remain static throughout the rest of the expansion. Figure 1.2 plots the competing ionization and recombination timescales to the plasma's expansion timescale. At the point the expansion timescale becomes smaller than the rate of recombination for the ion, the plasma is said to be frozen-in since the charge state distribution will then remain static for the rest of the plasma's expansion throughout the heliosphere. In turn, *in situ* observed ionic composition is able to estimate the coronal electron temperatures at the height when the plasma freezes-in.

The composition of heliospheric plasma is often measured with time-of-flight mass spectrometers, such as the Solar Wind Ion Composition Spectrometer (SWICS) (*Gloeckler et al.*, 1992, 1998) on both the Ulysses spacecraft (*Wenzel et al.*, 1992) and the Advanced Composition Spectrometer (ACE) (*Stone et al.*, 1998). Particles enter this type of an instrument through a deflection system which only allows particles with a particular energy-per-charge to enter the detector. For SWICS on Ulysses, the energy range covered is $0.16-59.6$ keV/e spanning the entirety of the bulk solar wind energies. Ions making it through the deflection system undergo a post-acceleration voltage which speeds the ions up enough to penetrate a carbon foil at the entrance of the time-of-flight (TOF) telescope. While passing through the carbon foil, the ion scatters secondary electrons from the foil, triggering a start signal for the time-of-flight determination. After traveling the length of the TOF telescope, the ion hits a solid state detector (SSD) which measures the total kinetic energy of the ion. When the ion impacts the SSD it scatters more secondary electrons, triggering the stop signal for the time-of-flight calculation. With both the start time and stop time of the ion, the time the ion spent traveling through the TOF is known. This leads directly to the ability to calculate the velocity of the ion. With both the total kinetic energy and the velocity of the ion known, it is possible to estimate the mass of the ion, aiding in the identification of the atomic species. Finally, measurements of the energy-per-charge, velocity, and total energy of the particle make it possible to identify the ionic species as well as calculate the phase space distribution of the plasma observed by the instrument.

1.3 Observations of ICMEs

A CME propagating through the heliosphere is typically referred to as an Interplanetary Coronal Mass Ejection (ICME). ICME plasma has many distinct properties (*Zurbuchen and Richardson*, 2006, and references therein) that make discriminating it from the background heliospheric plasma possible. Studies by *Jian et al.* (2006) and

Richardson and Cane (2010) have used these features to create lists of ICME plasma observed *in situ* by the ACE and Wind (*Acuña et al.*, 1995; *Harten and Clark*, 1995) spacecraft.

Figure 1.3 shows data from ACE measured in early 2005, adapted from a figure originally published in *Gilbert et al.* (2012). During this time period, two different ICMEs were observed, each illustrating a few examples of some of the typical plasma indicators. The two ICMEs are bounded by the vertical blue and black lines, with solid lines indicating the start times and the dashed lines indicating the end times, as determined by *Richardson and Cane* (2010). The top three panels show the usual bulk plasma parameters, measured from both the SWICS and the Solar Wind Electron, Proton, and Alpha Monitor (SWEPAM) (*McComas et al.*, 1998). In the second ICME, denoted by the black line, we see a decreasing plasma velocity. Decreasing plasma velocity is typically observed in an ICME due to the expansion of the event as it propagates through the heliosphere (*Klein and Burlaga*, 1982; *Russell and Shinde*, 2003; *Zurbuchen and Richardson*, 2006). The expansion of the plasma also decreases the density, since the ICME is magnetically confined with no significant source or loss mechanisms for the plasma. This is seen in the second ICME. The proton density steadily decreases throughout the duration of the event. As the plasma expands it, in turn, will also cool adiabatically(*Gosling et al.*, 1973; *Richardson and Cane*, 1995; *Zurbuchen and Richardson*, 2006), resulting in decreasing bulk plasma temperatures. Both of the ICMEs exhibit this expected decrease in the proton temperature, with it being more noticeable in the second ICME.

The next three panels of Figure 1.3 show compositional measurements of the ICME plasma for iron, oxygen, and carbon, from the SWICS instrument on ACE. Charge states indicative of hot plasma temperatures, such as those experienced by the ICME during the ejection process, have been shown to be a strong indicator of ICME plasma (*Hirshberg et al.*, 1971; *Bame et al.*, 1979; *Fenimore*, 1980; *Henke*

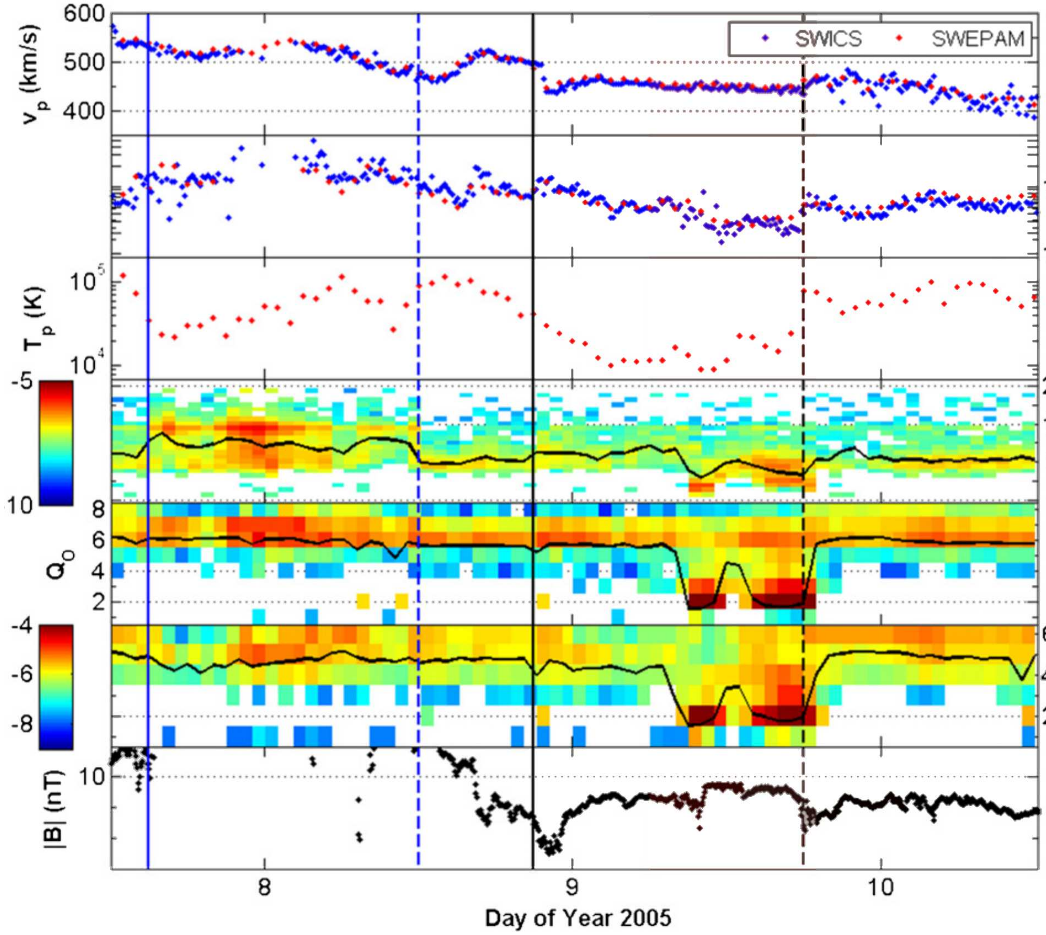

Figure 1.3: *In situ* observations of two ICME during 2005. The first is bounded with blue lines and the second is bounded by black. The start periods are denoted by solid lines and the end of the periods are denoted by dashed lines, as determined by *Richardson and Cane* (2010). Figure adapted from *Gilbert et al.* (2012).

et al., 2001; *Lepri et al.*, 2001; *Rodriguez et al.*, 2004; *Lepri and Zurbuchen*, 2004). During the ejection process, as we have previously discussed, CME plasma can be heated by reconnection. This heats the plasma to higher temperatures, which is then observable in the hot charge states of all three species appearing during the first ICME, bounded by the blue lines of Figure 1.3. In addition to hot ionic charge states, there have also been a very small number of ICMEs observed with cooler charge state composition (*Gosling et al.*, 1980; *Zwickl et al.*, 1982; *Gloeckler et al.*, 1999; *Skoug et al.*, 1999; *Lepri and Zurbuchen*, 2010; *Gilbert et al.*, 2012). These have been explained as direct observations of the very dense cold prominence that is often remotely observed accompanying CMEs. An example of this can be seen towards the end of the second ICME in Fig 1.3, where all three atomic species exhibit very low ionization states, indicative of cold plasma temperatures. In addition, to the cold charge states of carbon, oxygen, and iron, singly charged helium can be observed during ICME plasma (*Gosling et al.*, 1980; *Schwenn et al.*, 1980; *Gloeckler et al.*, 1999). These helium observations are related to prominence observations as well.

The bottom panel shows the magnitude of the magnetic field, as measured by the Magnetic Field Experiment (MAG) (*Smith et al.*, 1998) on ACE. In both the ICMEs, we observe an enhancement of the magnitude of the magnetic field during the ICME time period. This has been shown to be indicative of a Magnetic Cloud (MC) embedded in the ICME. An MC is described as a magnetic flux rope that dominates the configuration of the magnetic field in the ICME (*Lepping et al.*, 1990; *Mulligan and Russell*, 2001). MCs are observed to occur with enhanced magnetic fields which smoothly rotate with depressed proton temperatures and plasma beta (*Zurbuchen and Richardson*, 2006; *Klein and Burlaga*, 1982; *Hirshberg and Colburn*, 1969). MCs only occur in a subset of ICMEs (*Zurbuchen and Richardson*, 2006), while others have a very complex magnetic field configurations, not easily relatable to a flux-rope structure (*Burlaga et al.*, 2002).

It is important to remember that ICMEs often do not exhibit all of the features described in *Zurbuchen and Richardson* (2006). As can be seen in Figure 1.3, the first ICME, denoted by the blue lines, show expected hot charge states but do not show the typical bulk plasma parameter characteristics. The inverse is true in the second ICME, denoted by the black lines. The bulk plasma density, velocity, and temperature all decrease throughout the duration of the ICME due to expansion, but the charge state composition does not exhibit ionic states indicative of hot plasma temperatures. Instead, the plasma shows cold plasma ionic states towards the end of the time period. This is not unexpected, as *in situ* observations are only taken along the path the spacecraft takes through the event. This ends up being a very small observation of a very large structure. Through the advent of state-of-the-art models and multiple spacecraft observations, *in situ* determinations of the global structure have begun to be explored (*Reinard et al.*, 2010; *Lynch et al.*, 2011; *Lepri et al.*, 2012; *Reinard et al.*, 2012) using ACE, Ulysses, Wind, and the STEREO spacecrafts.

1.4 CMEs and Space Weather

As previously mentioned, ICMEs are very large ejections of solar plasma and magnetic flux from the surface of the Sun. It is not surprising then, that they are a primary driver of space weather events near Earth. ICMEs which impact Earth have been observed to be a possible cause of non-recurrent geomagnetic storms. A geomagnetic storm is a period of time when the magnetosphere becomes intensely energized causing an enhanced convective electric field. This occurs when an ICME, or some other strong heliospheric feature, compacts the magnetosphere which then can trigger a sudden storm commencement (*Veenadhari et al.*, 2012). The sudden storm commencement may precede the beginning of the geomagnetic storm and is described as a period of time when the Earth's horizontal magnetic field, measured by surface magnetometers, changes drastically. If the magnetic field lines of the

ICME are oriented southward, they can then reconnect with the magnetic field of Earth, connecting the ICME magnetic field lines directly to the Earth's magnetic field. Plasma from the ICME is then able to precipitate down the field lines into the ionosphere, thereby intensifying the aurora and even allowing it to be observable at lower latitudes than normal. These field lines are swept behind the Earth, by the solar wind, which compresses the magnetotail as they pile up. This increases reconnection occurring in the tail, enhancing the amount of plasma flowing from the tail back to the Earth's inner magnetosphere. This plasma flow produces a strong enhancement of the ring current(*Gonzalez et al.*, 1994). This flow of flux and energy transfer in the magnetosphere is called a geomagnetic storm (*Tsurutani et al.*, 1988; *Gonzalez et al.*, 1994; *Koskinen and Huttunen*, 2006; *Gopalswamy*, 2008).

Figure 1.4 shows an observation, from the ISEE-3 spacecraft, of the magnetic field and bulk plasma parameters during a strong geomagnetic storm on August 28 of 1978, as published in *Gonzalez et al.* (1994). The geomagnetic storm is noticeable in the disturbance storm time index, D_{st}. The D_{st} measures the variation of the horizontal magnetic field at the magnetic equator. When this value varies greatly, it is indicative of compressed magnetospheric fields and increased ring currents. On August 28, we can see a dramatic drop in the D_{st} reaching nearly -200 nT. Immediately preceding the geomagnetic storm we observe many of the common features of an MC, as described early. Occurring near the beginning of August 28, we observe a large increase in the magnitude of the magnetic field as well as a smooth rotation in the vector components. During the MC we also observe the expected decrease in velocity and density. Further preceding this, on August 27, we observe a shock. All of these are indicative of an expanding ICME, with a preceding driven shock, which then triggers the observed geomagnetic storm.

Geomagnetic storms can be the direct ramifications of space weather events on the Earth's magnetosphere and can cause a variety of hazards in the Earth system.

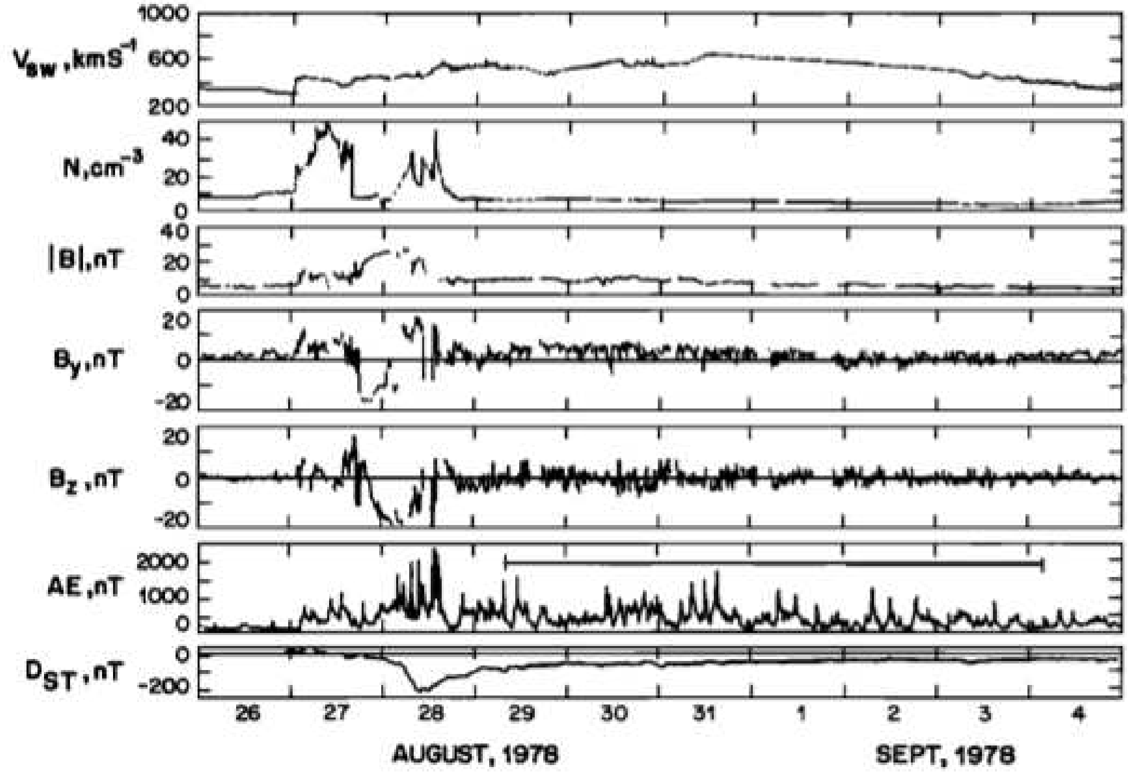

Figure 1.4: Magnetic field and plasma measurements from the ISEE-3 spacecraft. A large MC can be observed on August 27 with the accompanying large geomagnetic storm occurring on August 28. Figure published in (*Gonzalez et al.*, 1994).

Enhanced ring currents and increased flux propagating down the auroral field lines has direct impacts on the radiation environment along spacecraft orbits which can then effect them in a variety of ways. First, the larger flux and currents will increase the incident radiation which the spacecraft has to endure, potentially damaging critical components. Additionally, the increased flux will increase the density of the plasma that the spacecraft is traveling through. The increase of density will cause the spacecraft to experience greater atmospheric drag during its travel. The altitude which a satellite orbits at is directly related to its velocity. An increased drag on the spacecraft will decrease the velocity of the satellite, which can greatly effect the orbit of the satellite. Skylab re-entered the Earth's atmosphere early due to increased drag on the spacecraft from a storm (*Compton and Benson*, 1983). Finally, the enhanced flux may cause the spacecraft to become charged. As more electrons impact the spacecraft, they can become embedded on the satellite increasing the potential on the vessel. A strong potential on the spacecraft can result in arcing of the components which damages the spacecraft.

The effects can be felt on the surface of the Earth as well. The enhanced currents occurring in the ionosphere during geomagnetic storms can induce currents on the surface of the Earth. Oil pipelines, electrical grids, and communication grids can all become damaged by the induced currents. The blackout of 1981 in Quebec, Canada was caused by a geomagnetic storm. The induced currents blew circuit breakers, melted transformers, and heavily overloaded the entire system. The entire system failed for nearly 9-hours as a direct result (*Boteler et al.*, 1998).

Finally, geomagnetic storms can cause radiation hazards to humans during spaceflight or onboard planes flying over the poles. Aircraft fly at high altitudes, into the stratosphere, when they fly over the poles. This takes the aircraft into the region where the flux precipitates down polar field lines, causing them to experience a much larger dose of radiation than flights at lower latitudes. During geomagnetic storms the dose of radiation for both space travelers and polar flight passengers is greatly increased (*Singh et al.*, 2010). This can increase the risk of radiation sickness and even cancer for these individuals (*Reitz et al.*, 1998; *Cole*, 2003).

ICMEs have other impacts other than just causing geomagnetic storms of the magnetosphere, they can also drive interplanetary shocks (IP) preceding the events. ICMEs often travel at velocities greater than the local magneto-sonic speed causing the shock to form (*Zurbuchen and Richardson*, 2006; *Corona-Romero et al.*, 2012). Figure 1.5 shows an illustration of this driven shock. Upstream of the ICME we see the driven shock. The region in between the ICME and the shock is called the sheath. The sheath consists of piled up shocked heliospheric plasma that is being pushed through interplanetary space by the event as well as coronal plasma which gets pushed out during the ejection of the CME. Sometimes a reverse shock can also be observed to form behind the CME, occurring with events that originate from high latitudes (*Gosling et al.*, 1988, 1994). Their cause is not fully understood yet, but they may be formed by the over-expansion of the ICME (*Gosling et al.*, 1988, 1994), or from the interaction of deflected slow and fast wind streams in the rear of the ICME (*Manchester and Zurbuchen*, 2006).

These ICME driven shocks are one possible source of Solar Energetic Particles (SEPs) (*Reames*, 2013, and references therein). SEPs are particles with energies ranging from hundreds of keV all the way to GeV. The shock produces these particles through diffusive shock acceleration. Particles can gain energy at shocks through adiabatic heating in the compressed plasma downstream of the shock. During diffusive shock acceleration particles experience these compressions multiple times if they become magnetically bottled between the turbulent magnetic field upstream and downstream of the shock. Particles that are energetic enough can then bounce back and forth across the shock, continually gaining more energy each time it becomes heated in the compressed region. Eventually the particles will gain enough energy

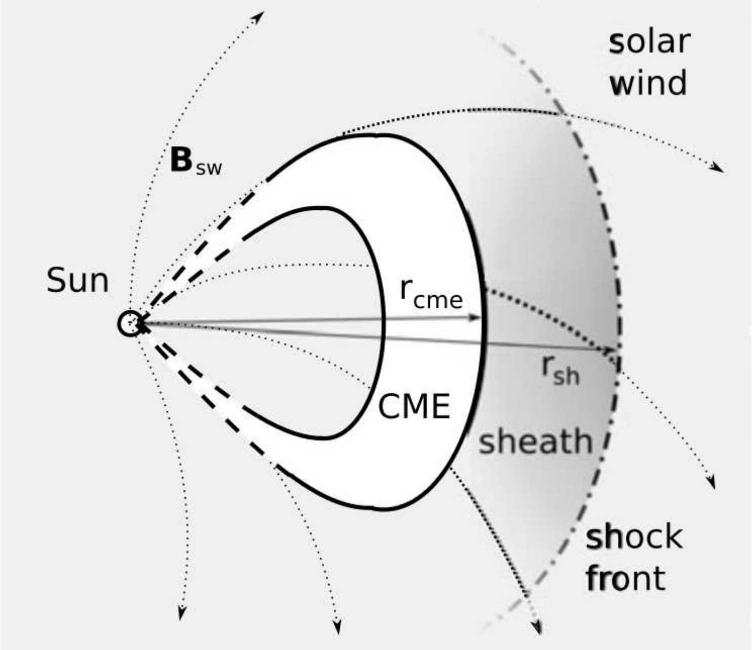

Figure 1.5: Illustration of the ICME-driven shock directly preceding the event. The plasma in between the shock and the ICME is referred to as the sheath. Adapted from *Corona-Romero et al.* (2012).

that they escape the shock front altogether, leaving the region with much greater energies (*Drury*, 1983). Bulk particles are not necessarily mobile enough to jump across the shock multiple times, but the suprathermal particles may be. By comparing compositional measurements of the SEP particles streaming from the ICME to the suprathermal plasma composition of the ICME, it has been observed that the two plasmas are related (*Desai et al.*, 2006; *Mewaldt et al.*, 2006). The suprathermal plasma may be a very important seed population for the SEP particles which are accelerated by ICMEs.

Energetic particles from ICMEs can also pose problems for spacecraft in the heliosphere. They can be caused by the SEP mechanism, as previously described, or can be produced in the flare and reconnection sites during the ejection of the CME. They can negatively effect many instrument measurements as they saturate detectors with increased noise. One example of this, is the particle ”snow” that occurs in LASCO coronagraph images just after the observation of a CME ejection. These particles can also damage spacecraft, as the most energetic ions can travel through the radiation shielding protecting critical components, such as onboard memory and the computer systems, and damage them (*Larson and Wertz*, 2005).

1.5 Suprathermal Particles

Heliospheric suprathermal particles are composed of ions ranging in energies from 1 keV to $>$ 100 keV. Figure 1.6 shows a long term accumulation of a distribution function of heliospheric protons measured by Ulysses/SWICS near 5 AU. The distributions are not Maxwellian, but exhibit two additional contributions. The first one is coming from interstellar pickup ions - interstellar gas penetrating into the heliosphere and being ionized and picked up by the expanding magnetic field. The second contribution is a near power-law expansion referred to as a suprathermal tail that consist of particles that have been accelerated to energies greater than both the solar wind and the pick-up ions. It can be seen that the the suprathermal plasma occurs at much lower densities than the normal solar wind, nearly a factor of 10^6 smaller on average. Particles from all of the usual solar atomic species have been observed with suprathermal energies, with compositions reflecting that of the solar wind (*Mason et al.*, 2012). Particles with these energies can be an important seed population for even more energetic particles, as they can more easily be accelerated to even higher energies than the bulk solar wind plasma. Suprathermal ions are known to be further accelerated at co-rotating interaction regions (CIRs) (*Mason et al.*, 2012), as well as other IP shocks, as one mechanism for producing SEPs (*Tylka et al.*, 2005; *Reames*, 2013). The phase space distribution of the observed suprathermal tail has the form of a power law, as seen in figure 1.6 (*Fisk and Gloeckler*, 2006, 2007; *Gloeckler et al.*, 2008).

The acceleration responsible for suprathermal particles has been widely debated, with two processes being the most discussed, namely diffusive shock acceleration and

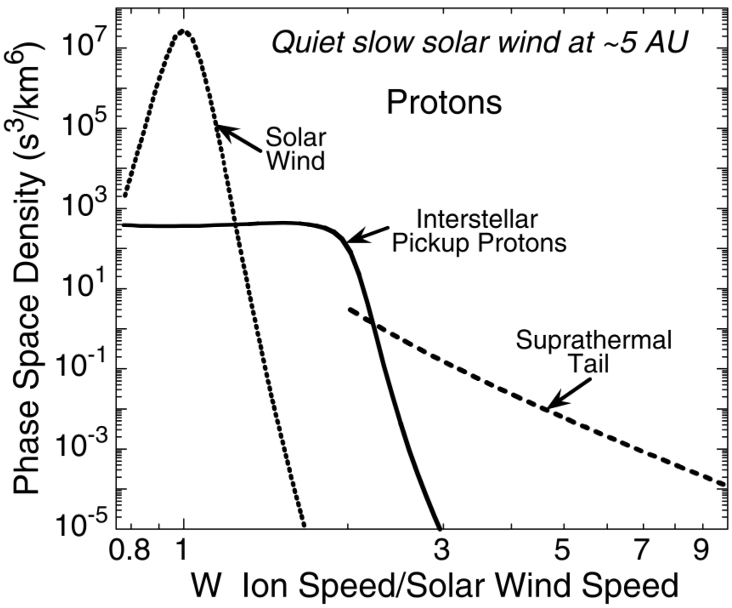

Figure 1.6: Long duration accumulation of the proton distribution function observed during slow solar wind. The three main populations of the proton distribution are denoted. Observations made by Ulysses/SWICS. Figure published in *Fisk and Gloeckler* (2007).

stochastic acceleration such as the pump mechanism (*Fisk and Gloeckler*, 2012a). Diffusive shock acceleration has long been associated with energetic particle acceleration, including being invoked in an attempt to understand the origin of the suprathermal plasma (*Bell*, 1978; *Blandford and Ostriker*, 1978; *Drury*, 1983; *Lee et al.*, 2012). *Jokipii and Lee* (2010) and *Giacalone* (2012) have both proposed that IP shocks can accelerate the local solar wind plasma up to the suprathermal energy regime using a diffusive shock acceleration mechanism. The bulk solar wind particles experience scattering across the shock front, causing them to bounce back and forth, continually experiencing the shock potential and increase in energy. *Fisk and Gloeckler* (2012a) have argued that the efficiency of solar wind particles being accelerated by the shock is too low to account for the propensity of the common spectral index in the suprathermal population. In order for the particles to bounce back-and-forth across the shock, they must have initial energies greater than the local thermal velocity. This enables the random motions of the particles to diffuse back and forth across the shock.

Instead they argue for a pump mechanism, in which particles experience expansions and contractions in the local plasma (*Fisk and Gloeckler*, 2008, 2012a). When the local plasma becomes contracted it undergoes adiabatic heating, which energizes the plasma. Conversely, expansions causes a decrease in the overall energy of the particles. The most energetic particles are able to escape the local compression region, before the plasma expands, retaining a higher energy than what the particle initial had. As the plasma experiences a number of expansions and contractions, the plasma's particles diffusive throughout the energy spectrum forming the suprathermal tail. These expansions and contractions can come from many places, with turbulence in the magnetic field being the most likely source in the heliosphere. The robustness of the mechanism has made it possible to employ it in a wide array of applications. They have used the pump mechanism outside of the heliosphere, to attempt to understand particle acceleration in the heliosheath, producing Anomalous Cosmic Rays (ACRs) (*Fisk and Gloeckler*, 2009) and even in interstellar space, producing the Galactic Cosmic Rays (GCRs) (*Fisk and Gloeckler*, 2012b).

1.6 The Suprathermal Ion Composition Spectrometer

Suprathermal plasma has been traditionally measured by *in situ* mass spectrometers, such as SWICS on ACE and Ulysses. The deflection system of both SWICS instruments allow particles with an energy up to ~ 100 keV/e to be measured. This enables the highest energy measurements from these sensors to sample the low energy portion of the suprathermal tail. These instrument were specifically designed to observe the lower energy bulk plasma. In order to avoid saturation of the sensors, the instruments were designed to accommodate the higher density observations of the solar wind. This hinders the ability of these instruments to make accurate high-cadence observations of the suprathermal tail. Therefore, many studies have had to use long time accumulations of the suprathermal plasma, to minimize the statistical error of the suprathermal measurements. Instruments have been built to specifically observe the suprathermal energy regime have begun to be used, such as the Plasma and Suprathermal Ion Composition (PLASTIC) investigation (*Galvin et al.*, 2008) on the Solar Terrestrial Relations Observatory (STEREO) (*Kaiser et al.*, 2008) and the Suprathermal Ion Composition Spectrometer (STICS) (*Gloeckler et al.*, 1995) on the Wind spacecraft.

STICS is a time-of-flight mass spectrometer, similar to SWICS but without a post acceleration voltage applied to the incoming particle. STICS measures particles with energies between $6.2 - 223.1$ keV/e, enabling full ion composition measurements focused on the ions in the suprathermal energy regime, producing a similar data product to SWICS. Wind is a spin-stabilized spacecraft with the field-of-view of STICS oriented perpendicular to the spin axis. This, coupled with three distinct telescopes observing different elevation angles, STICS is able to observe the full three-dimensional distribution function of the suprathermal plasma (*Gloeckler et al.*, 1995; *Chotoo*, 1998).

Prior to 2004, the Wind spacecraft focused primarily on observing the interaction between the heliosphere and the Earth's magnetosphere through a large number of petal orbits crossing the bow shock. Using a 5 year span of orbits taking the spacecraft into the heliosphere, *Posner et al.* (2002) discuss observations of low charge state heavy ions upstream of Earth's bow shock. They found occurrences of these events as far as 130 R_{e} upstream of the bow shock. Additionally, the occurrence of such events is seen to increase during solar maximum. They conclude that these events are produced from substorm activity occurring at the Earth when the IMF is such that magnetic field lines are able to be mapped from the dayside reconnection site out to Wind. *Posner et al.* (2003) builds upon this study by analyzing in greater detail one such observation of O^+ and N^+ upstream of the bow shock to determine the spatial structure of the outflow. Using the full 3-dimensional distribution function they are able to put constraints on the geometry of the flux tube containing these escaping ions. The petal orbits of Wind crossed the trajectory of the moon a number of time, providing a the chance to observe lunar pick-up ions (*Mall et al.*, 1998). Observations such as this give insight into the composition of pick-up ions from the lunar source, namely O^+, Al^+, Si^+ and even maybe P^+.

After mid 2004, the Wind spacecraft moved out into a stationary orbit about the first Lagrange point (L1) in order to continually observe heliospheric plasma. Before this though studies have been conducted singing out heliospheric plasma observations. (*Chotoo et al.*, 1998) presented a combination of the helium observations from both STICS and the high mass resolution spectrometer (MASS) to span particle velocities of $v/v_{\rm sw} \approx 0.8 - 1.6$. They then show that a kappa function produces the best fit to this extended distribution. (*Chotoo*, 1998; *Chotoo et al.*, 2000) continue to combine STICS and MASS observations from the Wind spacecraft as well as using data from the Suprathermal Energetic Particle (STEP) instrument to investigate the seed population for particles that are accelerated at co-rotating interaction regions (CIRs). This study made a number of important conclusions such as the fact that suprathermal CIR ions are accelerated in the inner hellosphere and not the outer heliosphere as previously believed (*Fisk and Lee*, 1980). Additionally, in at least one of the CIRs they investigated they concluded that the acceleration was not associated with a shock mechanism, but instead most likely from a statistical or compressional mechanism.

1.7 Science Questions

Compositional measurements have been shown to be powerful discriminators of CME plasma, constraining the origination site of the solar wind, either streamer source or coronal-hole source (*Geiss et al.*, 1995; *von Steiger et al.*, 2000; *von Steiger*, 2008). They have also been used to make estimates of the plasma environment in the corona, near the heights at which the ions become frozen-in. This region is important in the acceleration and heating of the solar wind and the physical process at play during the eruption of solar transients. However, these processes are still not fully understood, as the ability to make observation of coronal plasma is difficult. In this work, we push the uses of composition measurements further in order to investigate important questions relating to the origin of observed plasma. Namely,

1. What are the characteristic of the early coronal environment during CME eruptions?
2. What is the origin of the seed population for the suprathermal plasma?

1.7.1 What are the Characteristic of the Early Coronal Environment During CME Eruptions?

During their early eruption, reconnection processes in the corona and plasma interactions with the ambient coronal plasma and solar wind, shape the thermodynamic evolution of CMEs. As a CME erupts, magnetic field lines reconnect back to the sun closing off both the transient and the solar field it originated from, thereby dissipating magnetic energy as well as accelerating particles. Associated with the eruptions, flares are occasionally observed. Flares and reconnection jets are likely consequences of the magnetic reconfiguration during the eruption and its subsequent relaxation process. Compressions of the plasma occurring during the reconnection process can act to heat the plasma rapidly after the CME erupts. Further downstream the transient begins to expand and adiabatically cools. This causes the temperature and density of the CME to decrease as it travels through the heliosphere. These drastic temperature environments that the CME experiences are not without consequence on the ionic composition. The ionic composition of the plasma can be pushed further away from the equilibrium distribution. Utilizing the *in situ* measured ionic composition states, we can estimate the early coronal electron environment that the CME plasma experiences during the ejection, as well as understand how the unique expansion properties of the CME effect the plasma environment. To address this important question, we have developed a model for ionic charge states that helps to relate the violent plasma interactions in the corona and can predict *in situ* charge states.

First, in chapter II we discuss the results of the *Gruesbeck et al.* (2011) study. In this study, we develop the dynamic charge state evolution model that will be used to recreate the *in situ* ionic composition using an imposed electron density, temperature, and bulk flow velocity profiles. Using this model we investigate the compositional observations of hot plasma co-located with cooler plasma during ICMEs. Doing this,we are able to place constraints on the electron environment and the effect of the ICMEs expansion on the resulting composition. Chapter III focus on the unusually cool charge states that are sometimes observed in ICMEs. We discuss the results of the *Gruesbeck et al.* (2012) study. Even though we had earlier shown that hot charge states can be produced concurrently with colder states because of the expansion effects of the CME, we show that these incredibly cool charge states are not capable of being produced from a single plasma. Instead we determine that these observations are in fact *in situ* measurements of both ICME plasma and remnant prominence plasma. Finally, in chapter IV we discuss a few innovative studies that have been facilitated by the charge state evolution model. We discuss the studies of *Landi et al.* (2012a), *Landi et al.* (2012b), and *Zurbuchen et al.* (2012) which uses the charge state evolution model to constrain the coronal environment where solar wind originates from. We also discuss the use of the charge state model as a validation tool for MHD solar wind models and the use of bridging remote observations to *in situ* measurements.

1.7.2 What is the Origin of the Seed Population for the Suprathermal Plasma?

By utilizing the unique ionic compositional characteristic of ICMEs, we can explore the source of the suprathermal plasma observed in an ICME by comparing it to the bulk plasma upstream of the transient. If the shock is the primary mechanism then the suprathermal composition will resemble that of the unshocked plasma upstream. However, if a local mechanism is at play, the suprathermal plasma will resemble that of the co-located bulk plasma. Either one of these mechanisms will have strong implications on the resulting composition of the suprathermal particles observed *in situ* during the event.

To address the acceleration process of suprathermal particles, we develop new data from the STICS sensor, as discussed in Chapter V. We focus on two new analysis techniques, we have developed, to investigate the ICME suprathermal particle composition. First, we describe a new accumulation method to produce the phase space distribution. Typically, we accumulate the observed counts for a specified period of time and then calculate the phase space distribution. Instead, we have devised an accumulation method where the cadence varies in order to achieve a minimum threshold of statistical error in each measurement period.

In Chapter VI, we present the study comparing the suprathermal particle composition to that of the thermal bulk composition during a select number of ICMEs. ICMEs events to study were determined using the adaptive cadence method in which the statistical error was the smallest for heavy ion observations. This is presented in chapter VI. We find that the suprathermal plasma is strongly correlated to the co-located bulk plasma and not very related to the bulk plasma upstream of the CME-driven shock. This result has strong implications on the origin of the suprathermal seed population.

CHAPTER II

Constraints on Coronal Mass Ejection Evolution from in Situ Observations of Ionic Charge States

The text in this chapter was published in: Gruesbeck, J. R., S. T. Lepri, T. H. Zurbuchen, and S. K. Antiochos (2011), Constraints on Coronal Mass Ejection Evolution from *in Situ* Observations of Ionic Charge States, *ApJ, 739*, 103.

Abstract

We present a novel procedure for deriving the physical properties of Coronal Mass Ejections (CMES) in the corona. Our methodology uses *in situ* measurements of ionic charge states of C, O, Si, and Fe in the heliosphere and interprets them in the context of a model for the early evolution of ICME plasma, between 2 - 5 $R_\odot$. We find that the data is best fit by an evolution that consists of an initial heating of the plasma, followed by an expansion that ultimately results in cooling. The heating profile is consistent with a compression of coronal plasma due to flare reconnection jets and an expansion cooling due to the ejection, as expected from the standard CME/flare model. The observed frozen-in ionic charge states reflect this time-history and, therefore, provide important constraints for the heating and expansion time-scales, as well as the maximum temperature the CME plasma is heated to during

its eruption. Furthermore, our analysis places severe limits on the possible density of CME plasma in the corona. We discuss the implications of our results for CME models and for future analysis of ICME plasma composition.

2.1 Introduction

Coronal Mass Ejections (CMEs) are an important source of plasma and magnetic field in the heliosphere and the drivers of space weather events near Earth. They are characterized by the rapid and explosive release of large quantities of coronal material entrapped in its magnetic field. The rate of occurrence of CMEs is directly tied to the solar cycle (*Gopalswamy et al.*, 2004) making them one important consequence of solar activity. Ejections from the Sun are more prevalent during solar maximum conditions and occur nearly 10 times less frequently (*Gopalswamy et al.*, 2004) in the deepest of the solar minimum.

CMEs are observed remotely in many wavelengths including white-light observations, by the Large Angle Spectroscopic Coronagraph (LASCO) (*Brueckner et al.*, 1995), for example. Indeed, many CMEs are observed to be closely associated with enhanced plasma heating and energization, often relating to flare events during and immediately following the eruption (*Harrison*, 1995; *Vršnak et al.*, 2005). Extreme ultraviolet (EUV) and soft X-ray emissions are most often used to analyze such heating (*Krucker et al.*, 2010). These energization events can release energetic particles which are observed in remote observations of soft X-ray (*Dauphin et al.*, 2006), hard X-ray (*Temmer et al.*, 2010; *Goff et al.*, 2005), and gamma-ray (*Lin et al.*, 2003). Energetic particles can further interact with plasma near the Sun, in particular near the chromosphere, and lead to chromospheric evaporation events. We can directly observe the heliospheric manifestations of the erupted plasma, the so-called Interplanetary CMEs (ICMEs) which are characterized by specific plasma characteristics (*Zurbuchen and Richardson*, 2006).

ICMEs are usually associated with magnetically dominated plasma, which appear to be approximately in a Taylor state with smooth and near force-free magnetic fields (*Burlaga et al.*, 1981). ICMEs observed near 1 AU often have bulk speeds that exceed that of the surrounding solar wind and therefore are associated with interaction signatures, such as compressions or shocks (*Zurbuchen and Richardson*, 2006, and references therein). Additionally, there are important expansion signatures, such as steadily decreasing velocity profiles, and depressed proton temperatures and densities (*Gosling et al.*, 1973; *Richardson and Cane*, 1995). Unusual charge states of heavy ions in the ICME plasma is another important signature (*Bame et al.*, 1979; *Henke et al.*, 1998; *Lepri et al.*, 2001; *Lepri and Zurbuchen*, 2004; *Rodriguez et al.*, 2004; *Zurbuchen et al.*, 2003). In fact, these compositional signatures were recently shown to be more prevalent than initially assumed, making them a powerful tool in ICME identification (*Richardson and Cane*, 2004, 2010).

Figure 2.1, shows the plasma, magnetic field and compositional signatures of an example ICME as observed with the Advanced Composition Explorer (ACE) (*Stone et al.*, 1998). The steadily decreasing velocity profile, the low density and depressed temperatures are all signatures of an expanding magnetic cloud. The ICME is magnetically dominated and has the key characteristics of a flux-rope configuration.

Figure 2.1G-K show measurements of the ionic distribution of C, O, Si and Fe. Unusually high charge states in C, O, Si, and Fe are the most important compositional signatures of this ICME, and many others; indicative of enhanced collisional ionization near the Sun. In fact, it has been reported that 50% of all ICMEs exhibit elevated charge states in Fe (*Lepri et al.*, 2001) and generally, exhibit elevated states in the other species as well. The oxygen charge distribution, which usually peaks at O^{6+} in the solar wind, peaks at O^{7+}, which is also observed in the O^{7+}/O^{6+} ratio, and has important contributions of O^{8+}. Similarly, carbon charge distributions in ICMEs are observed to be strongly dominated by C^{6+}, the fully ionized state. The most unusual

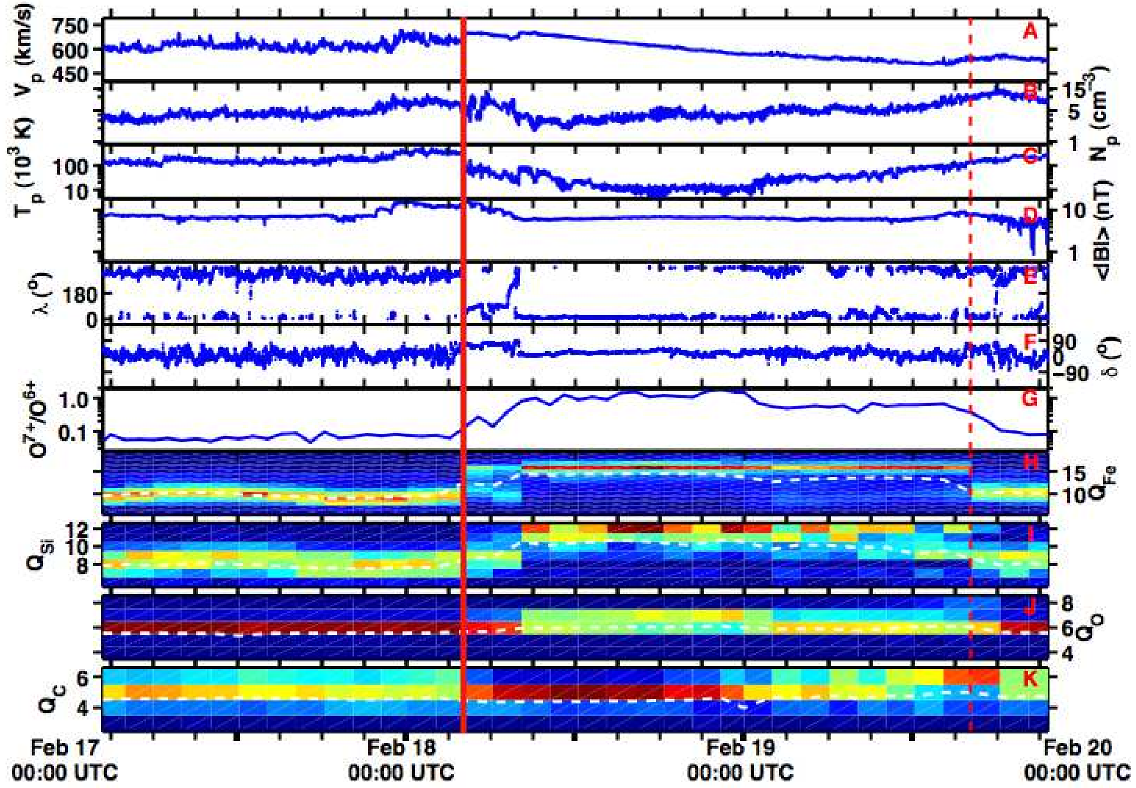

Figure 2.1: Summary of plasma parameters and charge state distribution for an ICME observed on February 18, 2003 by the ACE spacecraft. From top to bottom we show proton velocity (V_p), proton density (N_p), proton temperature (T_p), magnetic field magnitude ($|B|$), RTN longitude (λ), RTN latitude (δ), O^{7+}/O^{6+} ratio, Fe charge state distribution (Q_Fe), Si charge state distribution (Q_Si), O charge state distribution (Q_O), and Ca charge state distribution (Q_Ca). The ICME plasma field begins at the solid red line, at 0400 UT on February 18, 2003, and ends at the dashed red line, at 1600 UT on February 19, 2003, where these boundaries were determined by (*Richardson and Cane*, 2010). It can be seen that the all four charge state distributions experience an enhancement during the ICME interval.

ionic charge state related to ICME plasma is the Ne-like charge state of Fe ($q = 16$) clearly visible in Figure 2.1H (*Lepri et al.*, 2001). Similarly, as we will discuss later, that silicon tends to be observed preferentially with a He-like charge state, ionized to Si^{12+}, as shown in Figure 2.1I.

The exact configuration of the observed ionization state is affected by collisional ionization, from electrons colliding with the ions in the plasma, and excitation autoionization , where electrons from the outermost shells are lost due to the relaxation of an inner shell electron (*Cowan and Mann*, 1979; *Hundhausen et al.*, 1968; *Hundhausen*, 1972). The observed ionization states are an important indicator of the CME's thermal environment close to the Sun. They are formed through a freeze-in process within 1-5 solar radii ($R_\odot$) (*Bame et al.*, 1974; *Buergi and Geiss*, 1986; *Hundhausen et al.*, 1968; *Hundhausen*, 1972). Very close to the Sun, while time-scales for recombination and ionization are much shorter than the plasma's expansion time-scale, the ionization states of heavy ions are approximately in ionization equilibrium, reflecting the local electron temperature. Due to the CME's expansion into the heliosphere, the electron density decreases rapidly and thus the recombination time-scale increases as well. At a given heliocentric distance - depending on the specific characteristics of each ion, and the electron environment - the ionic charge states freezes in and no longer changes. At this point, the charge-state is said to be "frozen in." Due to the characteristic differences of atomic physics for each ion, the heliocentric distance where freeze-in occurs varies widely, and simultaneously observed charge-state distributions become a sensitive measure for the thermal evolution of the CME plasma near the Sun during the entire radial range where freeze-in occurs.

The unique nature of ICME charge states is further illustrated by Figure 2.2, showing a comparison of a time-period of slow solar wind composition observed from 0000 UT to 0200 UT on July 30, 2003 with observation of an ICME from 0200 UT to 0400 UT on January 27, 2003. It is evident from Figure 2.2, that there is a noticeable

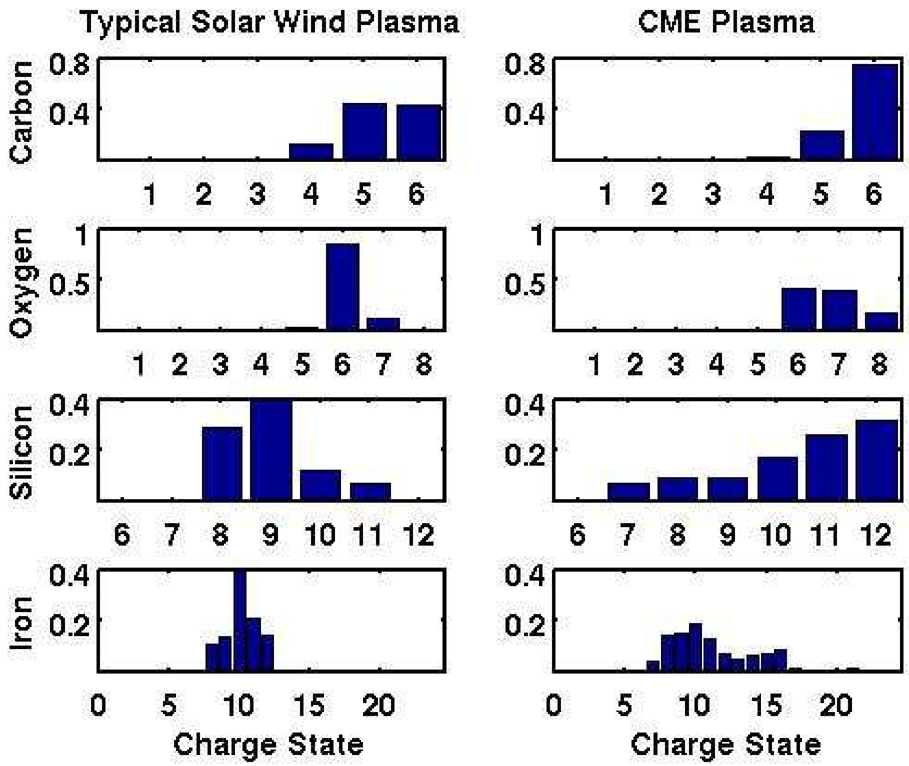

Figure 2.2: A comparison of the slow solar wind (left) and of ICME plasma (right). The ICME plasma shows enhanced charge states for all four atomic species compared to the typical solar wind. Note the bimodal structure of Fe with peaks at Fe^{10+} and Fe^{16+}. For more details, refer to text.

increase in ionic charge states for each element in the ICME plasma compared to the typical wind. There is also a significant change in the qualitative nature of the distributions. Specifically: (1) a significant fraction of C becomes fully ionized; (2) O shows large deviations from O^{6+}, a He-like charge state that dominates solar wind measurements; (3) Si charge states are substantially increased for the ICME period and peak at Si^{12+}, the He-like charge state; and (4) Fe transitions into a bi-modal charge-distribution peaked around Fe^{10+} and Fe^{16+}, the Ne-like charge state discussed earlier. Such bi-modal charge distributions have been anecdotally reported before, but it is not generally known how common they are within ICMEs.

The purpose of this paper is two-fold. First, we survey ionic charge states in ICME plasma to determine the rate of occurrence of bi-modal Fe charge state distributions. Secondly, we develop a model to determine physical constraints for the ICME expansion especially focused on bi-modal Fe charge state distributions, while simultaneously, qualitatively re-creating the C, O, and Si observations. Using this methodology, we will develop constraints for the temperature and density evolution of CMEs near the Sun.

2.2 Observations

This research is enabled, in part, by plasma observations from composition sensors such as the Solar Wind Ion Composition Spectrometer (SWICS) on board the Advanced Composition Explorer (ACE) (*Gloeckler et al.*, 1998). These instruments independently determine speed, mass and charge of incident ions and therefore enable the measurement of full charge distributions in ICMEs. The time-resolutions of these measurements are limited by counting statistics of incident ions, and are typically limited to 2 hours for ACE-SWICS. The O^{7+}/O^{6+} ratio is typically measured with 1 hour time-resolution. For each time-period, ions are accumulated and analyzed largely using the methodology described by *von Steiger et al.* (2000). The analysis of Fe charge states is rather straightforward because its mass of approximately 56 amu substantially exceeds the mass of other heavy ions of similar abundance in the solar wind. C and O are the most abundant heavy ions in the wind and are therefore easily discernible. Our Si measurements currently are limited to charge states between 8+ and 12+ due to significant overlap with other neighboring ions in time-of-flight and energy space. Using these data, charge-state calculations are successful approximately 99% of the time. Data-gaps occur due to low counting statistics or operational events on ACE independent of the solar wind plasma and compositional properties.

The analysis of each ICME includes composition data, as well as plasma and field observations, as demonstrated in Figure 2.1. The proton moments obtained by the Solar Wind Electron, Proton and Alpha Monitor (SWEPAM) (*McComas et al.*,

1998) are averaged over a 64 second time period. The magnetic field observations are provided by the Magnetic Field Experiment (MAG) (*Smith et al.*, 1998), averaged over 64 second intervals as well. ICME times and plasma boundaries are taken from *Richardson and Cane* (2010), which were determined primarily by magnetic and plasma signatures, while using composition and charge state data to confirm identification.

Richardson and Cane (2004) have previously discussed the observations of generally enhanced ionization of C and O within ICMEs as compared to solar wind of the same speed. Indeed, such signatures were observed in $70\% - 90\%$ of all CMEs irrespective of their field configuration. ICMEs associated with a magnetic cloud are shown to have a higher concurrence of compositional anomalies than non-cloud ICMEs.

Here, we focus on the bimodal nature of Fe distribution, generally with peaks at Fe^{10+} and Fe^{16+}. Inspecting the ACE data it is easily observed that bi-modal Fe charge states are often present in ICMEs. However, these signatures often don't extend throughout the event. For example, bi-modal distributions are observed in Figure 1 during the first 4 hours, from 0400 UT to 0800 UT. The bi-modal nature of the ICME is not easily discernable from time 0800 UT untill the beginning of February 19, but is seen again from then on until the end of the ICME passage at 1600 UT. In contrast, bi-modal Fe charge states are equally likely to be observed during any time periods within ICMEs.

Figure 2.3 shows ACE observations of a second ICME, observed on January 27 2003, presented in a format identical to that of Figure 2.1. The ICME boundaries were once again taken from the study by *Richardson and Cane* (2010).

The plasma composition during this ICME looks qualitatively similar to the event shown, in Figure 2.1: All four ionic distributions show significant enhancement during the event leading to higher than average charge states, indicative of temperature

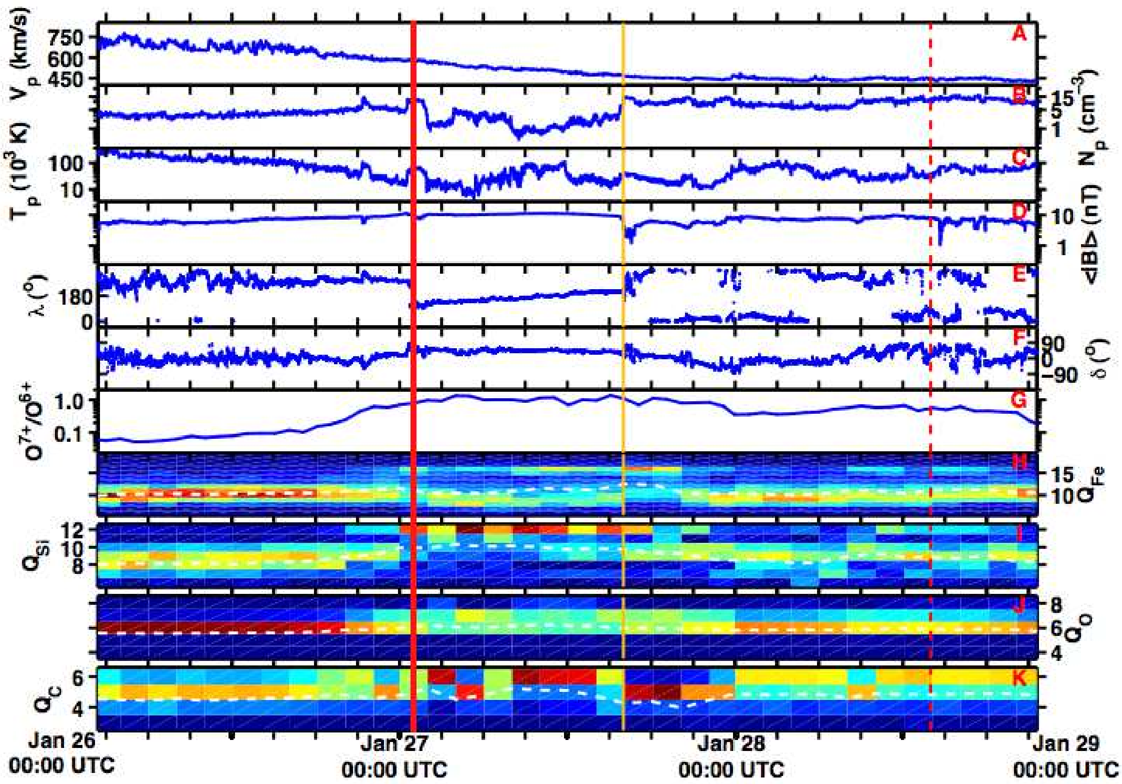

Figure 2.3: Summary of plasma parameters and charge state distribution for an ICME observed on January 27, 2003 by the ACE spacecraft. The ICME plasma field begins at the solid red line, at 0100 UT on January 27, 2003, and ends at the dashed red line, at 1400 UT on January 28, 2003. All ionic charge distributions show a significant enhancement during the event. It can also be seen that a majority of the Fe distribution displays a bi-modal shape. Note the qualitative compositional change at time 1600 UT of January 27, when the magnetic field abruptly changes, denoted by the gold line. A bimodal characteristic can also be observed in the middle of day 28.

enhancements. Also, the Fe charge state distribution is bi-modal for a majority of the ICME's duration.

It is well known that ICMEs often include identifiable sub-parts (*Mulligan and Russell*, 2001), with each having specific magnetic field configurations or plasma characteristics with well-defined transitions between them. The ICME in Figure 2.3 includes such a qualitative transition at time 1600 UT on January 27. Prior to this, the magnetic field configuration is that of a magnetic flux-rope with the characteristic suppressed magnetic field turbulence, and reduced density characteristic of a magnetic cloud (*Klein and Burlaga*, 1982; *Richardson et al.*, 2000; *Zurbuchen and Richardson*, 2006). The plasma temperature exhibits some interesting sub-structure during this time-period. At 1600 UT we observe a distinct transition visible in all plasma quantities - except for the plasma velocity. After 1700 UT, the magnetic field is again rather smooth; however, its axis has changed direction.

The compositional signatures appear to reflect this transition as well. SWICS does not have a high enough time-resolution to analyze this change in compositional signatures with the same time-accuracy as SWEPAM and MAG, however there are discernible differences between the compositional signatures before and after 1600 UT. The heavy ion composition during the first part of the ICME has substructures which have qualitative correspondence with variability in plasma temperature. It has also been argued that this plasma heating is strongly associated with flares (*Lepri and Zurbuchen*, 2004; *Rakowski et al.*, 2007; *Reinard*, 2005). Based on this observation, as well as analogous observations in Figure 2.1, and in many other ICMEs studied, we conclude that compositional structure reflects the plasma-structure and topology in ejecta.

An interesting question to ask is,how prevalent are bi-modal Fe distributions in ICME plasmas? We address this by surveying all ICMEs from 2000 till 2007 identified and characterized by *Richardson and Cane* (2010). For each ICME in this time-

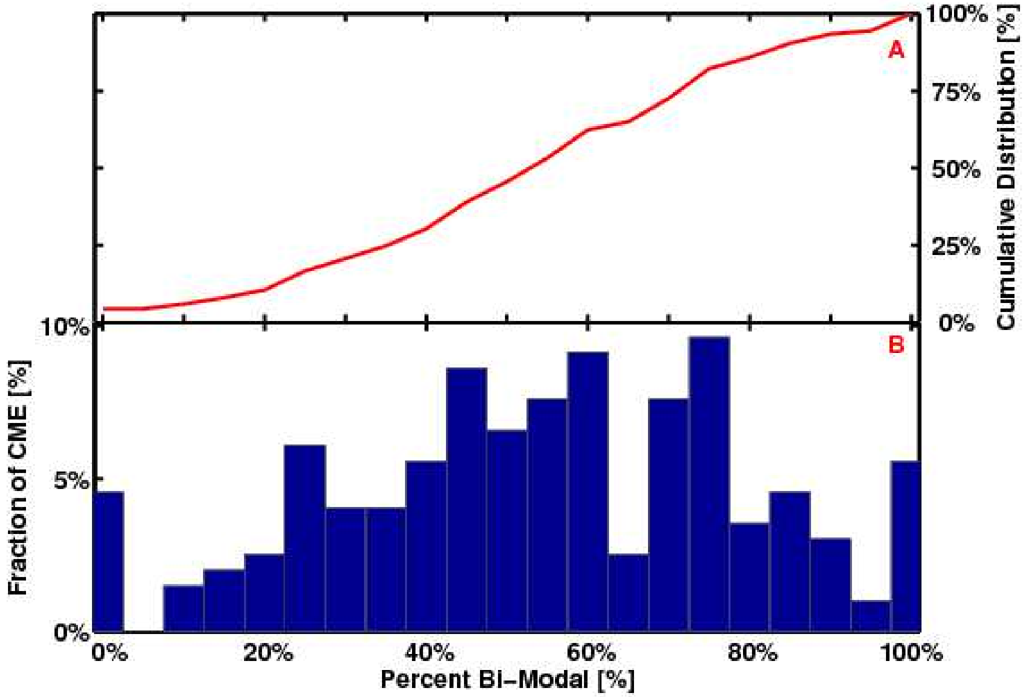

Figure 2.4: Statistical survey of bi-modal Fe distributions in ICME plasma. The bottom panel is a histogram showing the results of the survey. Percentage of total CMEs investigated is the vertical axis, while percentage of bi-modal plasma in the CME is on the horizontal axis. The top panel shows a cumulative distribution function (CDF) of the resulting dataset. This vertical axis is the probability that a given CME will have at least percentage of bi-modal Fe in the plasma field as the corresponding percentage on the horizontal axis.

period, the percentage of bi-modal plasma is determined. This percentage is defined as the ratio of the time with bi-modal Fe observations divided by the total time during the ICME period during which composition data exist. The bi-modal characteristic is assumed to be present if there was a significant minimum in the ionic charge distribution, which includes more than one single charge state. This limits spurious minima caused by poor statistics in the data.

Figure 2.4 shows the results of this survey, including approximately 200 ICMEs. Figure 2.4A shows the cumulative probability distribution function (CDF) computed from 2.4B, which shows a probability distribution of ICMEs according to the fraction that is observed in the bi-modal state normalized to 1. It is immediately noticeable that more than 95% of ICMEs in this study include a measurable fraction of bi-modal Fe plasma. This finding also indicates that 95% of ICMEs exhibit elevated Fe charge states within their boundaries. High charge states in ICMEs are therefore much more ubiquitous than reported in previous studies, which indicated that the prevalence of high charge states was 50% (*Lepri and Zurbuchen*, 2004; *Lepri et al.*, 2001). Using the CDF plot in the top panel, it can also be seen that 50% of ICMEs have at least 55% bi-modal Fe charge distributions. This bimodal condition is thus found to be common in nearly all ICMEs and therefore becomes a critical observational criterion for our understanding of thermal properties of all CMEs near the Sun.

It has been previously argued that bimodal Fe observations are the result of plasma mixing between hot and cold populations (*Gibson et al.*, 2006; *Gopalswamy et al.*, 2001; *Rakowski et al.*, 2007). However, our analysis together with the qualitative analysis of transitions in ICMEs, suggest that bimodal charge distributions are an intrinsic property of a given plasma flow and not likely a mixing signature, which might be more diffusive in nature and more focused on specific boundaries and locales between cold and hot parts of a given CME. Using a simple ionization model, we show that bimodal charge states can result from a rapidly heated plasma close to the Sun, which then cools as the plasma expands moving downstream. If the bimodal distribution were truly a mixing signature, one would not expect to observe it nearly as often as we have shown in Figure 2.2. The nearly ubiquitous presence of some bimodal material suggests that its distribution is a result of an inherent property of the plasma and not a mixing phenomenon.

2.3 Model

The authors have developed a freeze-in code, which solves for the final charge state distribution of a given atomic species under simple assumptions on a given

CME's heating and expansion properties. To obtain the relative density of a given ion, $y_{\mathrm{i}} = n_{\mathrm{i}} / \sum_{\mathrm{i}=0}^{Z} n_{\mathrm{i}}$, and in particular, the freeze-in condition, the following continuity equation, valid in the rest-frame of the ejected CME (*Ko et al.*, 1997), is solved:

$$\frac{\partial n_{\mathrm{i}}}{\partial t} = n_{\mathrm{e}}(y_{\mathrm{i}-1}C_{\mathrm{i}-1}(T_{\mathrm{e}}) - y_{\mathrm{i}}(C_{\mathrm{i}}(T_{\mathrm{e}}) + R_{\mathrm{i}-1}(T_{\mathrm{e}})) + y_{\mathrm{i}+1}R_{\mathrm{i}}(T_{\mathrm{e}})). \tag{2.1}$$

It is important to note that n_{i} is the number density of charge state i of the atomic species of interest, while y_{i} is the relative number density. To solve this equation, the ion-specific recombination rates, R_{i}, and ionization rates, C_{i}, from *Mazzotta et al.* (1998) are used. These rates include electron ionization and auto-ionization as well as radiative and dielectronic recombination under the assumption of locally Maxwellian electron distribution functions, which has been used as reasonable approximation in previous studies (*Laming and Lepri*, 2007, eg). These depend only on the electron temperature T_{e} and are valid for all temperatures greater than 10^4 K. Photo-ionization is neglected here, as it plays a significant role for only singly and some doubly-charged ions (*Marsch et al.*, 1995).

Equation 2.1 can be solved using a given electron density and temperature history ($n_{\mathrm{e}}(t)$, $T_{\mathrm{e}}(t)$), which can be assumed, or constrained by observations. The system of ordinary differential equations described by Equation 2.1 is generally stiff as recombination and ionization rates can vary over many orders of magnitude. To address this, we use a 4^{th} order Runge-Kutta method that is specially suited for stiff equations (*Press et al.*, 2002). For computational efficiency, the method also uses an adaptive step-size. At each time, the method solves for the number density of an atomic species ionized to charge state i. We also check the accuracy of the integrator by testing the condition $\sum y_{\mathrm{i}} = 1$. Our integrations are accurate to better than 10^{-6}.

To model the heating and expansion of the plasma using the equations above, we calculate the CME bulk parameters at each time t. We examine two types of evolution, one in which the CME plasma close to the corona is assumed to be in an elevated temperature and density state and then undergoes a pure adiabatic expansion. We show below that this evolution is not compatible with the composition data. The other evolution is one in which we include an initial rapid heating phase while the plasma is in the lower corona, and then impose the adiabatic expansion. Such a heating would be expected from the energy release due to the flare reconnection that forms the ejected CME flux rope in the breakout model (e.g., *Lynch et al.*, 2004).

Since the heating of the ejected plasma is not well-known from first-principles models, we assume a simple, *ad hoc* form for this heating that has the minimum possible parameters. The plasma is taken to have some initial plasma temperature T_0 at $t = 0$, which rapidly increases to a specified maximum temperature (T_{max}), in a specified heliospheric distance (r_{heat}). Generally, the heating distance is chosen to be some value between 0-0.5 $R_\odot$ from the surface. In addition to the heating profile, some assumption must be made as to the evolution of the density. The simplest is to allow the density to evolve adiabatically; in other words, the heating is due to a pure compression of the plasma. Such a compression is, indeed, seen in simulations of CME/flare evolution. The reconnection jets coming out of the flare current sheet drive plasma compression both in the flare loop system remaining in the corona and in the escaping CME plasmoid. However, we also expect there to be some direct heating of the plasma due to magnetic dissipation *throughout* the CME/ICME evolution. This direct heating is highly model specific; therefore, to keep our results in this paper as general as possible, we consider only an adiabatic compression for the initial heating evolution, as well as an adiabatic expansion for the ejection. Of course, given some quantitative model for CME temperature and density evolution, it would be straightforward to use it, instead of the adiabatic assumption, in our analysis.

Equation 2.2 shows the forms of the temperature and density evolution that we use for the initial heating. Note that the model has only four free parameters: the initial temperature and density, the maximum temperature, and the radius at which this maximum temperature occurs. This is the minimum possible number of free parameters for any such model.

$$\left.\begin{array}{rcl} T(t) & = & (T_{\max} - T_0)\sin(2\pi\frac{([r(t)/R_{\mathrm{Sun}}]-1)}{4*[r_{\mathrm{heat}}/R_{\mathrm{Sun}}]}) + T_0 \\ n(t) & = & n_{\max}\left(\frac{T(t)}{T_{\max}}\right)^{3/2} \end{array}\right\} \text{where } r(t) \leq r_{\mathrm{heat}}. \tag{2.2}$$

The particular functional form for the temperature evolution, a quarter sinusoid, was used to qualitatively match the rapid heating near the corona, but its exact shape is not critical to create bimodal distributions. Additionally it ensures that the temperature has a continuous derivative, which is necessary for greater accuracy of the numerical method. The evolution of the density is derived directly from the adiabatic expansion formula, assuming a monoatomic ideal gas. After the rapid heating phase, the plasma cools as its volume expands. Again, the adiabatic equations couple the density and temperature evolution. Equation 2.3 shows the equation that describes the evolution of these parameters.

$$\left.\begin{array}{rcl} T(t) & = & T_{\max}\left(\frac{n(t)}{n_{\max}}\right)^{\gamma-1.0} \\ n(t) & = & n_{\max}\left(\frac{r_{\mathrm{heat}}}{r(t)}\right)^{\beta} \end{array}\right\} \text{where } r(t) > r_{\mathrm{heat}}. \tag{2.3}$$

The parameter β is an expansion factor of the plasma, typically set to a value between 2 and 3. The cooling is dependent on the adiabatic index, γ, which is set 5/3, the value for an ideal monoatomic gas. Note that $n_{\max}$ and $T_{\max}$ occur at the end of the heating period and define the beginning of the expansion cooling phase.

Motivated by observational characteristics of CMEs, our model allows for a non-constant velocity profile of the plasma. It is particularly important to model rapid acceleration of CMEs near the Sun. CMEs rapidly accelerate to a maximum velocity, which remains nearly constant, much like the velocity profile of the solar wind (*Gallagher et al.*, 2003). Using LASCO coronagraph images, a linear acceleration can be determined for some CMEs (*St. Cyr et al.*, 2000). The SOHO/LASCO CME catalog makes these values available for CMEs when the calculation is possible. In our model, therefore, the CME plasma undergoes linear acceleration from the corona until the velocity reaches the observed *in situ* velocity, from ACE. After this, the velocity is set to the observed value and remains constant.

Note that the total mass of CME plasma is assumed to be constant during the evolution: there is no net gain or loss of particles. Furthermore, as the plasma is continually ionized, the free electrons remain in our plasma volume. This allows the plasma to experience as much recombination as is possible by the available electrons, creating quasi-local ionization and recombination. In addition, we have no specific requirements on the velocity distribution of the electrons. The model also assumes that all electrons have a Maxwellian distribution. Additionally, we initialize the charge state of our plasma from the local thermodynamic equilibrium solution from the ionization equations discussed earlier. Finally, the computed temperature is used to determine the ionization and recombination rates at each time step.

To study the various physical characteristics of freeze-in within CMEs, we study a CME with an associated linear acceleration. This allows us to determine a velocity profile. Specifically, we use a velocity profile matching the January 27, 2003 CME determined from the linear acceleration (*St. Cyr et al.*, 2000) and ACE observations and whose velocity profile is shown in Figure 2.5. We then perform a parametric study to understand the temperature profiles that may lead to the observed characteristics. To demonstrate the impacts of the various model parameters on the freeze-in ionization rates, we perform a series of combinations of the following three characteristics, which we found to be crucial for this calculation: rapid heating, rapid expansion and an elevated initial bulk density. We want to show that the absence of one of these key characteristics leads to qualitative disagreements to the observations summarized in Figure 2.2. The key assumptions of three illustrative calculations are shown in

Figure 2.5.

First, results shown that include a with rapid heating and rapid expansion, but with relatively low initial density, close to typical solar wind densities (*Wilhelm et al.*, 1998). Second, results from the case having rapid expansion and an enhanced bulk density are shown. However, no heating is present and the plasma only cools. Third, results are shown that include all three ingredients. This is the only case that reproduces, qualitatively, the observed freeze-in distributions. To determine the relative accuracy of these cases, we use the January 27, 2003 event shown in Figures 2.3; however, it should be noted that our model is not sophisticated enough to match the data quantitatively. We can only to match the general characteristics of the observed ionic charges states of heavy ions, such as the Fe bi-modal distribution.

Figure 2.5 summarizes the basic assumptions for each set of input profiles used; different colored lines represent a different case. The top panel shows the density evolution for each model. The second panel shows the temperature evolution. Here, the red and blue lines are on top of each other, since they both experience rapid heating, while the blue line diverges initially. The initial temperature of the cooling only case was chosen such that it becomes similar to the temperature curves of the other cases downstream of the corona. This was done to ensure that any difference in results was due only to the near coronal heating profile and not to any other portions of the temperature profile. It is also important to note that the shape of each case's temperature curve qualitatively matches the shape of its respective density curve. This is a result of the temperature and density evolutions being tied together by the adiabatic relation. Finally, the last panel shows the velocity, which is identical for all three cases, as this curve was determined from LASCO and ACE observations of this particular CME by the method described above. Below, we show the final charge state results and evolution for these three model cases.

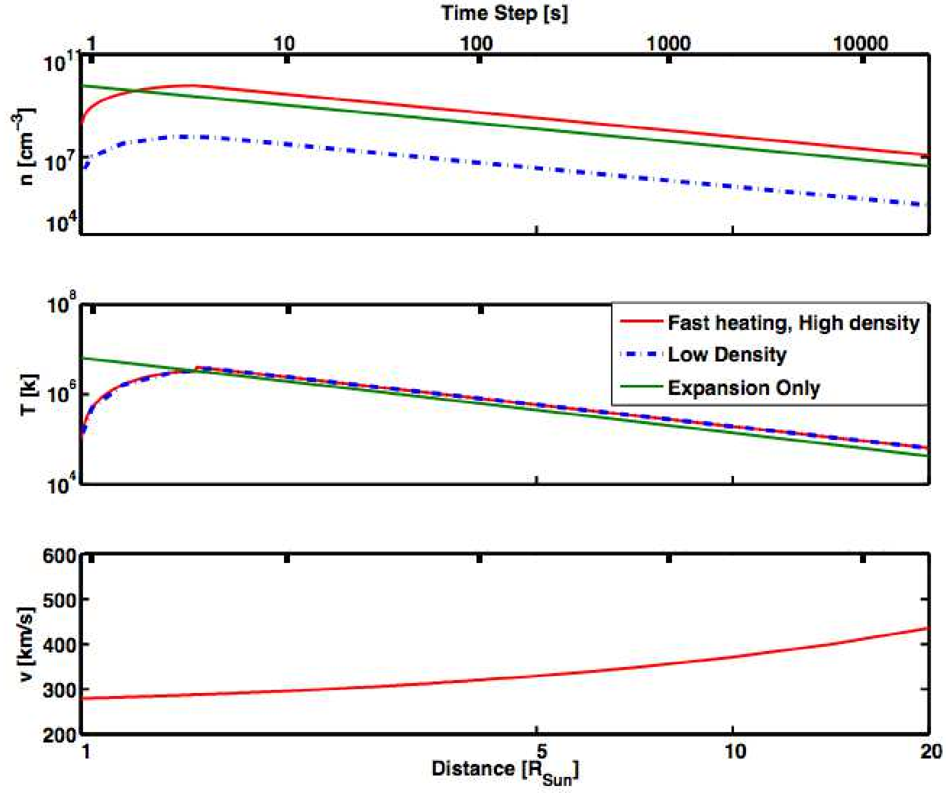

Figure 2.5: The bulk plasma parameters for the model run of the January 27, 2003 CME. From top to bottom volume, density, temperature and velocity are shown. The red line is the case with both fast heating and high density. The blue line is the case with only rapid heating, but a depressed density. Finally, the cyan line is the case for no heating of the plasma, only the rapid expansion of the plasma.

2.4 Results and Discussion

As discussed in the previous section, we ran our freeze-in and CME expansion model for three different cases attempting to recreate the charge state observations from the January 27, 2003 CME (Figure 2.3). The first case simulates a CME plasma that undergoes rapid heating near the corona, along with rapid expansion of its volume. However, the initial electron bulk density is low, 6×10^7 cm^{-3}, which is in qualitative agreement with nominal solar wind densities at the corona (*Wilhelm et al.*, 1998). Figure 2.6 shows the resulting charge state distributions of four atomic species (C, O, Si and Fe) plotted at specific time-intervals during the expansion. Expansion times were translated into radial scale using the integrated velocity profile shown in Figure 2.5.

The bottom four panels of Figure 2.6 show the evolution of the charge state distribution, for each species, from the coronal surface to a distance of 10 solar radii ,R$_\odot$, after which the ionic charge states remain frozen-in for all considered cases. In fact, charge states are generally frozen-in within a distance of 5 R$_\odot$ (*Buergi and Geiss*, 1986; *Hundhausen*, 1972), and our model agrees with this result showing the charge states to be frozen-in at a distance of approximately 3 solar radii. After this point, the charge states distribution remains constant. The top series of panels show the final resulting and frozen-in charge state distributions observed at 1 AU, the approximate location of in situ composition observations. It is immediately apparent, based on the data in Figures 2.2 and discussed in § 2.2, that the resulting charge states are much too cool . Without a significant density increase over solar wind profiles, the resulting ionic charge distributions are not sufficiently ionized, leaving the charge states of all the species at values much lower than are observed in ICMEs.

In Figure 2.7, we present the resulting charge state distribution from the case with initial high density and initial high temperature which only models the rapid expansion of an ICME.

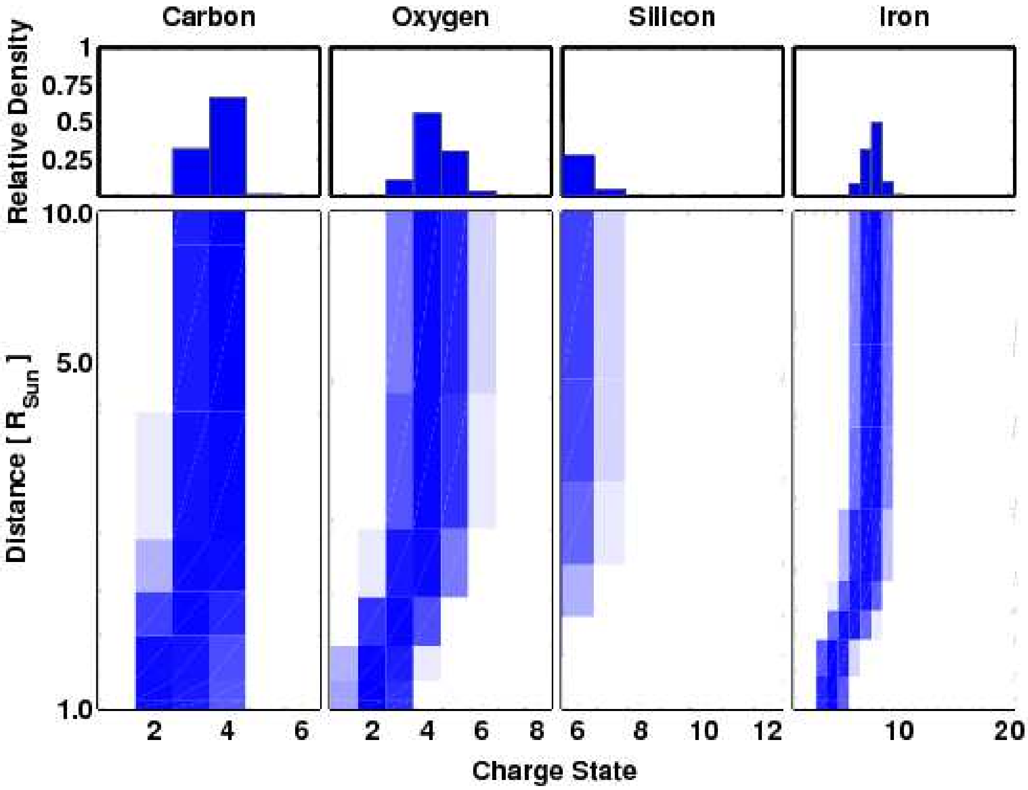

Figure 2.6: The results from the model which includes rapid heating and expansion, but with the omission of an enhanced initial density. The bottom set of panels show the evolution of the charge states from the coronal surface to a distance of 10 $R_{\odot}$ away plotted for arbitrary instances during the expansion. For all four atomic species, it can be seen that freeze-in occurred around 3 $R_{\odot}$. The top panels show the frozen-in charge state distribution observed at 1 AU.

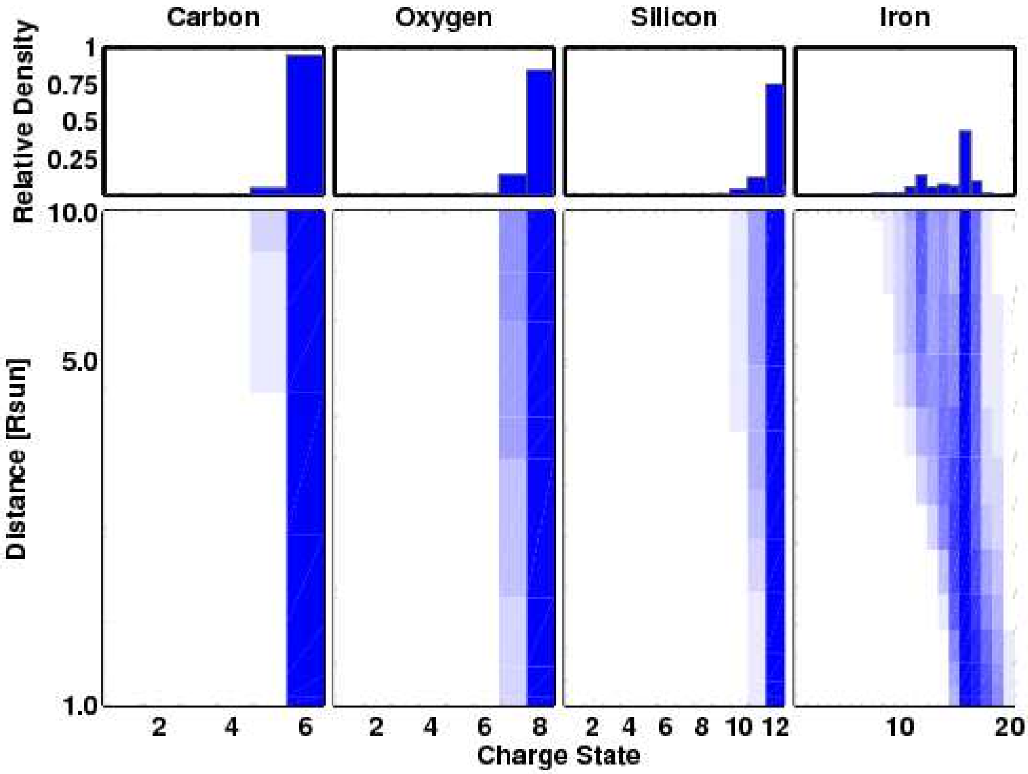

Figure 2.7: The results from the model which includes rapid expansion and also has a sufficiently large initial bulk density, but omits rapid heating. Format as in Figure 2.6.

It is evident that the resulting plasma in this case of pure expansion has more enhanced charge states for all atomic species than the previous low density case. The problem, however, is that the charge states at 1 AU are much hotter than is observed. The C, O, and Si are all essentially fully ionized. The reason is that the plasma has simply not had enough time to recombine down to the observed charge states due to the rapid expansion and accompanying density decrease. We note that the Fe distribution does exhibit bi-modality, but the peak at Fe^{16+} is much stronger than that at Fe^{10+}, which does not agree with observations. These results suggest that rapid expansion combined with high initial density may be critical ingredients for producing bimodal Fe distributions, but it is unlikely that these two ingredients by themselves cannot be made consistent with all the compositional data.

Finally, in Figure 2.8 we present the case where all three ingredients (high density, rapid coronal heating, and rapid expansion) are present in the model.

This case also shows a freeze-in behavior comparable to the previous case. Again, charge states freeze in within the first few solar radii from the corona, and the model matches the CME-like states of C and O as well as key characteristics of Si. However, under this set of assumptions, a qualitatively similar bimodal Fe distribution results, creating a consistent set of results under the assumption of a single density, temperature and velocity profile. Specifically, enhanced C and O charge states are seen, yet neither are fully ionized. Additionally, we see enhanced silicon charge states, and two distinct peaks in iron at Fe^{10+} and Fe^{16+}. The formation of bi-modal iron peaks is in part a result of high initial electron density and rapid expansion along with rapid heating, as can be seen by comparing Figures 2.7 and 2.8.

Figure 2.9 compares the results in Figure 2.6 and 2.8 with representative observations of the January 27, 2003 CME from 0100 to 1400 hours on January 28, which is representative of the bimodal distribution usually observed.

The top row of charge state distribution in Figure 2.9 shows the result of the

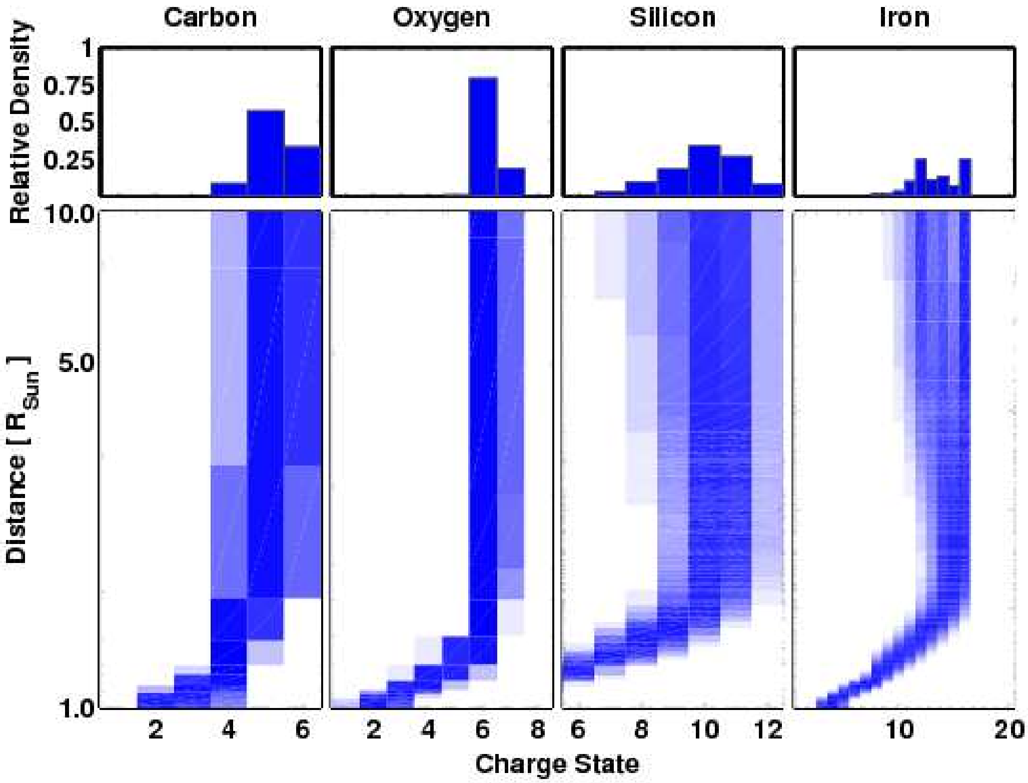

Figure 2.8: The results from the model for the case where the plasma is rapidly heated, experiences rapid expansion, and has a sufficiently high initial density. Format as in Figure 2.6.

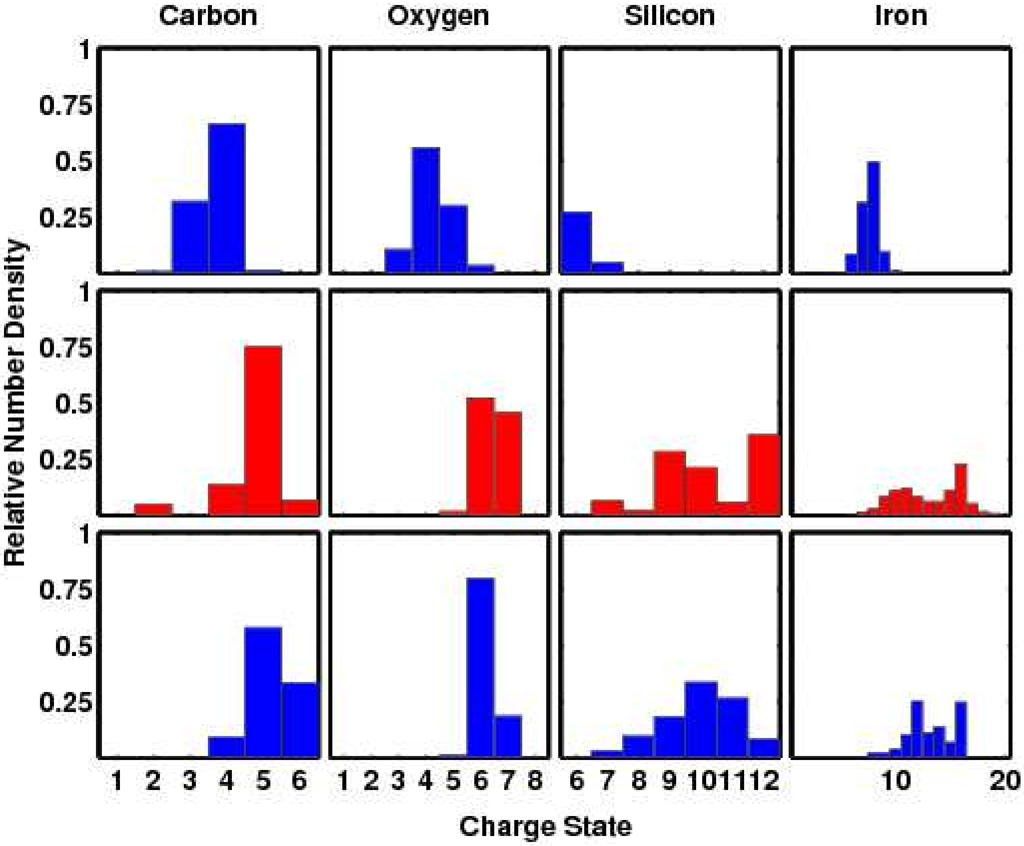

Figure 2.9: Charge state distributions for carbon, oxygen, silicon, and iron. The top row is the final distribution result from the model in Figure 2.6. The middle row is the observed ACE/SWICS charge state distribution for a two hour span of the January 27, 2003. The final row is the final distribution from the model in Figure 2.8.

model that had rapid heating and expansion, but lacked a high initial density, the results of the case shown in Figure 2.6. The bottom row, from Figure 2.8, shows the result when the density is high and rapid heating and expansion are present. We left out the case shown in Figure 2.7 because peaks are generally in the same place, and only the relative number density in the peaks differ. In addition, the Fe distribution of Figure 2.7 is primarily unimodal. The middle row shows the actual charge state distribution observations from ACE/SWICS of the January 27, 2003 ICME, which we are modeling here. All the charge states in the top-line are much lower than what is observed, while the relative shapes of the results in the bottom row are in qualitative agreement with observations, perhaps to a lesser degree for Si. Silicon from our model has a single peak, around charge states $Si^{9+,10+}$, while ACE observes a bimodal silicon distribution with peaks at Si^{9+} and Si^{12+}. Our model results in a considerable amount of Si^{11+}; which would be ionized further if the temperature curve was modified slightly to have a shorter heating period. Finally, experimental issues limiting Si data were already discussed previously and may also effect this comparison.

In order to test the robustness of our model's code, we verified that a population of hydrogen would be fully ionized, using the assumptions made for the third case. It was found that hydrogen became fully ionized, as expected. Additionally, we repeated this test for helium. Again, we found that helium becomes fully ionized; however, a small population recombines in the He^{+} population, 10^{-4} in relative density. This is due to the models assumptions, as this small recombination only occurs once the temperature of the plasma drops below the range of valid temperatures for the reaction rates. As previously stated, the rates used in the model are valid only for temperatures greater than $10^4 K$ (*Mazzotta et al.*, 1998), however, during the full evolution of our plasma, the temperature does fall below this value.

We also conducted tests to put a limit on how much the maximum density can vary with the particular temperature profile chosen. For the third case, which successfully recreated a bi-modal Fe distribution while matching C and O distributions, an initial electron density of 6.0×10^9 $[cm^{-3}]$ was used. By incrementing this value up and down we were able to determine a range of valid densities resulting in the Fe bimodal distribution, which is $4.75 \times 10^9 \leq n_e \leq 8.5 \times 10^9$ cm^{-3}.

2.5 Conclusions

The presence of high charge state ions in the solar wind is known to be a sufficient condition for identification of ICMEs, and was previously thought to exist in <70% of ICMEs. The current study reveals that 95% of ICMEs in fact have high ionic charge states, exhibiting bimodal characteristics in Fe. These findings reinforce the crucial role heavy ion composition signatures play in identifying ICME material. The pervasive nature of the observed ICME charge state characteristics at 1 AU (*Lepri et al.*, 2001; *Richardson and Cane*, 2010) suggest a simple and ubiquitous physical process or explanation. From running a large number of test models, we conclude that charge state distributions are powerful tools for constraining the thermal properties of CME plasma near the Sun. We find that bimodal Fe charge distributions can evolve from a plasma that rapidly expands from a high initial density. We also find that bimodal Fe observations and elevated Si observations can only be made consistent with concurrent C and O data, if the elevated initial density goes through a rapid heating before it cools in the expansion. No further assumptions are needed to fit qualitatively these data.

Based on our simulations, we also believe that there is a robustness to this result. For example, *Neukomm and Bochsler* (1996) focus on the evolution of charge state distributions of heavy ions in closed magnetic structures. Although they did not explore their models at sufficiently high temperatures, we see that certain key processes are consistent.

For example, the model suggests the importance of noble gas like charge states, such as O^{6+} and Fe^{16+}. These ionic states have recombination rates that are substantially smaller than their adjacent charge-states. Thus, these charge-states freeze in earlier than their adjacent charge-states, such as Fe^{15+}. Thus, subsequent cooling of initially hot plasma will tend to have Fe^{16+} to remain prevalent, whereas Fe^{15+} can further cascade to lower states, such as 14+, 13+, etc. This is the inherent cause for the dual-peaked nature of the observed Fe charge characteristic, and thus expected to be a robust result, independent of the details of the heating and cooling of the plasma.

We cannot exclude the possibility that other candidate processes, such as non-thermal electron characteristics near the Sun, or more complex evolutions involving multiple sources of plasma can achieve similar agreement with observations. We would argue, however, that the basic plasma evolution derived in this work - a rapid compression followed by an expansion - is the simplest and most likely explanation for the in situ observations. In order to observe Fe^{16+} at 1 AU, the plasma must reach fairly high temperatures, several MK, before the radius at which the freeze-in condition sets in. But if the plasma is in thermal equilibrium at this point, then the resulting charge states for the lighter elements would be too high at 1AU, as in Figure 2.7. The only way to avoid this discrepancy is to heat the plasma rapidly so that the lighter elements never reach their fully ionized state, while the iron achieves high ionization. Furthermore, since the velocity and expansion properties of CMEs are fairly accurately known from coronagraph observations, the observed charge states distributions impose tight constraints on the plasma density during this heating and expansion evolution. Too low a density implies that the various elements never reach the observed ionization states; whereas too high washes out the bimodal peak in iron. These straightforward and compelling arguments demonstrate the power of our compositional analysis techniques for deriving the detailed properties of the solar origins of space weather from *in situ* measurements in the heliosphere,

Note that the evolution determined by our composition analysis: a rapid compressive heating to high density followed by expansion cooling is fully consistent with the expected effects of flare energy release on the thermodynamics of CME plasma (*Harrison*, 1995; *Vršnak et al.*, 2005). These effects have been discussed by many authors (e.g., *Canfield and Reardon*, 1998; *Li et al.*, 2008) and typically relate to reconnection processes going on near the Sun (*Lynch et al.*, 2004). The upward directed reconnection jets from the flare current sheet are expected to compress and heat the CME plasma, as derived above. By combining our data and modeling techniques with sophisticated MHD simulations (*Antiochos et al.*, 1999; *Gombosi et al.*, 2000; *Linker et al.*, 1990), we can obtain a powerful tool for the analysis of CMEs and their evolution near the Sun. The computations presented in Figure 2.8 provide predictions of the presence of certain ions at specific times during the CME's evolution and should be testable, especially by forward modeling in which the calculation of the charge state evolution is included in the MHD simulation. A key point is that the various models for CME onset predict different locations for the initial heating of the coronal plasma that is ejected into the heliosphere as an ICME (e.g., *Forbes et al.*, 2006). Of course, many of these differences are expected to be washed out during the propagation to 1 AU; however, with the advent of composition measurements near the Sun from missions such as Solar Orbiter, our analysis may be able to determine not only the coronal evolution of CME plasma, but the fundamental mechanism responsible for the eruption itself.

CHAPTER III

Two-Plasma Model for Low Charge State ICME Observations

The text in this chapter was published in: Gruesbeck, J. R., Lepri, S. T., and T. H. Zurbuchen (2012), Two-plasma Model for Low Charge State Interplanetary Coronal Mass Ejection Observations, *ApJ, 760*, 141.

Abstract

Recent ACE/SWICS observations have revealed that $\sim 5\%$ of all *in situ* observed ICMEs include time-periods with very low charge state ions found to be associated with prominence eruptions. It was also shown that these low charge state ions are often observed concurrently with very high charge state ions (*Lepri and Zurbuchen*, 2010). But, the physical process leading to these mixed charge states is not known and could be caused by either the mixing of plasmas of different temperatures or by non-local freeze-in effects as discussed by *Gruesbeck et al.* (2011). We provide a detailed and multi-stage analysis that excludes this latter option. We therefore conclude that time-periods of very low charge-states are the heliospheric remnants of plasmas born in prominences. We further conclude that the contemporaneously observed low and very high charge states are an indication of mixing of plasmas of different tem-

peratures along magnetic field lines, suggesting that silicon and iron are depleted over carbon and oxygen in the cold, prominence associated plasma. This represents the first experimental determination of elemental composition of prominence associated plasma.

3.1 Introduction

Violent and spectacular eruptions of solar mass and magnetic field from the corona are called coronal mass ejections (CMEs). These explosive transient events have been remotely observed using coronagraphs since the 1970s, from *Skylab* (*MacQueen et al.*, 1974) and their understanding has been further revolutionized by observations from Solar and Heliospheric Observatory (SOHO), Solar Terrestrial Relations Observatory (STEREO), and Solar Dynamics Observatory (SDO) (*Dere et al.*, 1997; *Wiik et al.*, 1997; *Harrison et al.*, 2008; *Patsourakos et al.*, 2010). CMEs are a key ingredient of space weather in the heliosphere and near Earth. They are also an important source of plasma and magnetic fields in the heliosphere (*Hundhausen*, 1987); their release is thought to contribute to the solar cycle variation (e.g., *Riley et al.*, 2006; *Owens et al.*, 2008). Common in many of these coronagraphs is a three-part structure which characterizes the CMEs (*Illing and Hundhausen*, 1986). First is the bright leading edge of a CME, presumably made up of compressed and heated plasma. Next is the dark cavity, a region of less dense plasma dominated by an enhanced magnetic field. Finally is the bright core, a very dense population of colder plasma, associated with prominence material (*Rouillard*, 2011, and references therein). Such three-part structures are observed in coronographs in $\sim 70\%$ of all CMEs (*Gopalswamy et al.*, 2003; *Webb and Hundhausen*, 1987; *Munro et al.*, 1979).

Solar prominences are observed as spectacular bright features in the corona, often in a loop-like shape of typical length-scales of 100,000 km or longer. Despite being immersed in coronal plasma of temperatures around 1MK, prominences radiate visible light, indicative of much cooler plasmas and even neutral gas that is frictionally coupled to the plasmas in these structures (*Tandberg-Hanssen*, 1995). The arcade-like prominence field is associated with magnetic neutral lines in the photosphere (*Antiochos et al.*, 1994). These structures can be quasi-stable for many months, but can erupt into the heliosphere as part of CMEs, and are mostly observed in Thompson scattered white light of coronagraphs (*Gosling et al.*, 1974). During these eruptions, prominence material is observed to undergo heating (*Ciaravella et al.*, 1997, 2001). Yet, emission lines from neutrals and low-charge ions in erupted prominences have been observed out to 3.5 solar radii (*Akmal et al.*, 2001; *Ciaravella et al.*, 2003).

As the CMEs expand and propagate into the heliosphere, becoming an interplanetary coronal mass ejection (ICME), they can be detected using a variety of *in situ* signatures (*Zurbuchen and Richardson*, 2006), provided by a number of spacecraft, such as the Advanced Composition Explorer (ACE), Wind and others. Among these signatures, composition measurements have proven to be a particularly powerful tool in detecting ICME plasma (*Richardson and Cane*, 2004). For the past ∼20 years, mass spectrometers, such as the Solar Wind Ion Composition Spectrometer (SWICS) on both ACE and Ulysses, have enabled unprecedented observations of the compositional signatures of heavy ions with sufficient time-resolution to resolve ICMEs and their substructures (*Gloeckler et al.*, 1992, 1998).

Since the beginning of these observations, there has been a substantial discrepancy regarding the likelihood to observe prominences *in situ*: 85% or more of ICMEs exhibit compositional anomalies; they exhibit plasma with very high freeze-in temperatures that exceed those of regular solar wind, but only few are compositionally cold (*Richardson and Cane*, 2004; *Zurbuchen and Richardson*, 2006). The observed hot compositional anomalies are perhaps the most powerful identifying signatures of ICME plasma. Recently, *Lepri and Zurbuchen* (2010) found that only ∼ 4% of observed ICMEs contain significant densities of low charge state ions. *Lepri and Zur-*

buchen (2010) used a strict set of compositional selection criteria, so this number could effectively be higher, but it is in any case far removed from the 85% number of remote observations.

It is the purpose of this work to quantitatively analyze the observational results by *Lepri and Zurbuchen* (2010) and also the follow-up study of *Gilbert et al.* (2012) in the context of a recently developed ionization model. Specifically, we want to use this model to constrain the thermal conditions that govern the coronal and heliospheric evolution of prominence plasma. We focus on the contemporary presence of very hot and unusually cold ions of the same atomic species within ICME observations. We will determine if the presence of the cold ions are a result of the cooling inherently experienced by an adiabatically expanding CME or if the cold ions are indicative of a cold plasma mixing with hot plasma during the eruption.

The ionization model described in detail by *Gruesbeck et al.* (2011) showed that a dense plasma undergoing rapid heating followed by adiabatic cooling from expansion, much like what a flare heated CME plasma would experience, recreates bi-modal iron charge state distributions much like those seen in many ICME plasma observations, with two peaks around 10^+ (1.0 MK) and 16^+ (7.3 MK). We will expand upon this and show that- under a set of specific conditions - we can achieve simultaneously enhanced Fe charges states around 7^+ (0.4 MK) and 16^+ (7.3 MK).

3.2 Methodology

Using the freeze-in code from *Gruesbeck et al.* (2011), we are able to simulate the evolution of the ionic charge state distribution for a given atomic species, by specifying an electron temperature and density profile as well as the bulk flow speed of the plasma. The code solves the set of ion charge state continuity equations described by *Ko et al.* (1997) using reaction rates from *Mazzotta et al.* (1998). These equations compute ionic charge states for a given electron density, temperature, and velocity profile of the plasma as it expands from the corona into the heliosphere. As with the previous study, we have chosen to model a representative ICME with charge state distributions from ACE/SWICS. Electron density and temperature profiles were determined by analyzing numerous iterations of the simulation to find the best qualitatively matching charge state distribution for carbon, oxygen, silicon, and iron. The velocity profile was determined in part by *Solar and Heliospheric Observatory/Large Angle Coronagraph-Spectrograph* (SOHO/LASCO) height-time observations of the CME which we are reproducing (*St. Cyr et al.*, 2000).

Figure 3.1 shows ACE observations of the May 20, 2005 event (*Lepri and Zurbuchen*, 2010) which we chose as a case study for this investigation. Panel A shows the proton velocity, panel B shows the proton density, and panel C shows the proton temperature as observed by the Solar Wind Electron, Proton and Alpha Monitor (SWEPAM) (*McComas et al.*, 1998) with 64 second resolution. Panel D shows the magnetic field magnitude, panel E shows the longitude of the magnetic field vector, and panel F shows the latitude of the magnetic field vector observed by the Magnetic Field Experiment (MAG) with 16 second resolution (*Smith et al.*, 1998). Panel G, H, I, J, and K show the plasma composition data from SWICS. Panel G shows the O^{7+}/O^{6+} ratio with 1 hour resolution, while panels H, I, J, and K show charge state distribution, with 2 hour resolution, of iron, silicon, oxygen, and carbon respectively. The ICME plasma boundaries, determined by *Richardson and Cane* (2010), are the dashed red vertical lines. The cold ICME plasma boundary, taken from *Lepri and Zurbuchen* (2010), is shown with the vertical solid magenta lines.

As seen in Figure 3.1, the plasma composition during the ICME is much different from that of nominal solar wind observations. It has been previously discussed that hot charge states are closely associated with ICME plasma observations (*Lepri et al.*, 2001; *Henke et al.*, 2001; *Richardson and Cane*, 2004). This behavior can be seen in the plasma composition of the May 20, 2005 ICME observation, as the average iron charge state moves from Fe^{+9} to a hotter distribution with a significant contribution from Fe^{16+}. Additionally, oxygen and silicon charge states show signs of elevated coronal temperatures as each species becomes more ionized. The O^{7+}/O^{6+} ratio is elevated during this time period and Si^{12+} becomes dominant, which is the maximum observable charge state for silicon. During the time period marked by the vertical solid magenta lines the plasma composition exhibits very low charge states indicating cold electron temperatures in the freeze-in region. Here the peak charge states drop from C^{6+}, O^{7+}, and Fe^{16+} to C^{2+}, O^{2+}, and Fe^{7+}, respectively.

We now attempt to reproduce these low charge state observations with differing types of simulations. We first test whether the observed ionic charge state signatures can be reproduced by a single plasma undergoing a complicated expansion history. In a first representative model, initial heating followed by adiabatic cooling for the CME will give rise to lower charge states; however, the plasma is not able to produce a significant contribution of hot plasma. A second model will assume that the observed distributions are the product of two plasmas with distinctly different temperature histories, akin to a prominence and cloud plasma respectively

The resulting charge state distribution after freeze-in of each of these simulations are compared to our ACE/SWICS observations. Our goal is not to quantitatively match all observations, but to obtain qualitative agreements with observed characteristics. To achieve this, we will score each models' ability to reproduce the ACE/SWICS observations based on their abilities to match a number of key and defining features of the ICME observation: For carbon, we will look for peaks around C^{2+} and C^{4+}; for oxygen we look for two peaks, one around O^{2+} and one at the helium like O^{6+}; for silicon, we only look for one peak around Si^{6+} and a broad overall distribution extending towards higher states; for iron, we look for two peaks, one around Fe^{7+} and one for Fe^{16+}. The scores for each model result are cataloged in Table 3.1. A score of 1 indicates that the model was able to recreate the feature

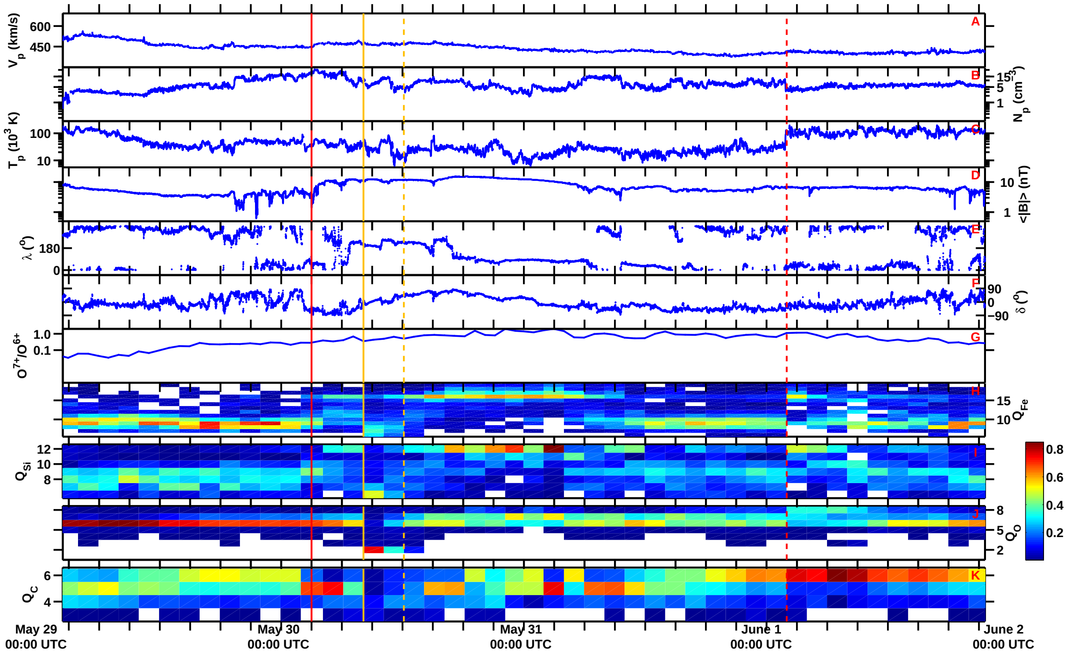

Figure 3.1: ACE observations of the May 20, 2005 ICME. From SWEPAM, panel A shows the proton velocity (V_p), panel B shows the proton density (N_p), and panel C shows the proton temperature (T_p). From MAG, panel D shows the magnetic field magnitude ($|B|$), panel E shows the RTN longitude (λ), and panel F shows the RTN latitude (δ). From SWICS, panel G shows the O^{7+}/O^{6+} ratio. The final four panels, H, I, J, and K, show the charge state distributions of iron, silicon, oxygen, and carbon respectively. The ICME plasma field begins with the solid red line at 0300 UTC on May 20 and ends with the dashed red line at 0200 UTC on May 22, where these boundaries were determined by *Richardson and Cane* (2010). The cold plasma observation begins with the solid yellow line, at 0808 UTC on May 20, and ends with the dashed yellow line, at 1208 UTC on May 20. These boundaries were determined by *Lepri and Zurbuchen* (2010).

while a score of 0 indicates that the model was not.

3.3 Single Plasma Simulations

We first attempt to create the observed charge state distributions using a single plasma, assuming that the unusually cold charge states are a byproduct of the adiabatic cooling of the ICME. The electron temperature and density profiles are shaped similarly to those from the *Gruesbeck et al.* (2011) study; a plasma is initially heated very rapidly and then cools as it expands. The red curves in Figure 3.2 shows the input electron profile which resulted in the closest qualitative match between the model results and the ACE/SWICS observations. Only the first 20 R_{Sun} is shown, since the charge state distribution for all the atomic species is frozen-in entirely within this region and do not change at larger heliocentric radii. The top panel shows the electron density profile, the middle panel shows the electron temperature, and the bottom panel shows the bulk flow velocity of the plasma. The density and temperature are related to each other adiabatically, as was shown in *Gruesbeck et al.* (2011). A hot, dense plasma was simulated first, with a maximum temperature of $2.6 * 10^6 K$ and the maximum density of $2.4 * 10^{10} cm^{-3}$. The velocity profile is determined by the linear acceleration calculated from height-time plots observed by SOHO/LASCO (*St. Cyr et al.*, 2000) and the 1 AU velocity of the ICME, as observed by ACE. Figure 3.3 shows the initial charge state distribution of the modeled plasma using an electron temperature of $1 * 10^4 K$, along row B, compared to ACE/SWICS observations from the May 20, 2005 ICME, along row A. Figure 3.4 shows the evolution of the charge state distribution during the first $10 R_\odot$ of the plasmas propagation. We see that the plasma reacts to the rapid increase of the electron temperature very quickly. Within the first $1 - 5 R_\odot$ the charge states are seen to be frozen-in, with the lightest elements freezing earlier.

In Figure 3.6, we show a comparison of the model results, along row B, to a

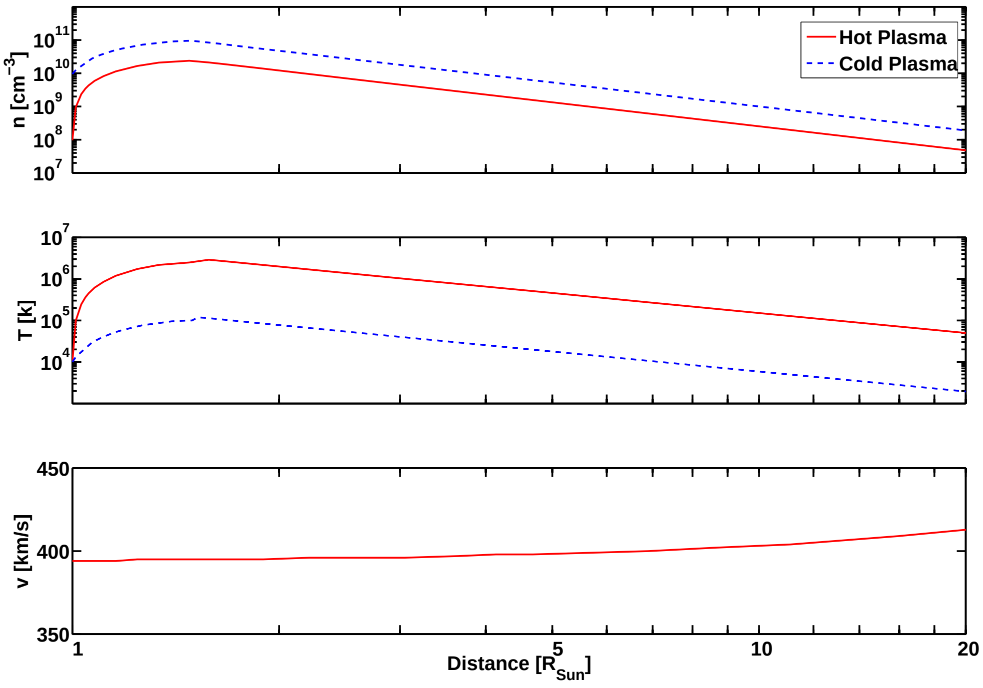

Figure 3.2: Input parameters for the freeze-in code for the multiple plasma simulation over the first 20 $R_{\odot}$. The top panel shows the electron density. The middle panel shows the electron temperature. While the bottom panel shows the bulk velocity, constrained from the linear acceleration plots from SOHO/LASCO observations for the May 20, 2005 ICME (*St. Cyr et al.*, 2000). The cold plasma is denoted by the blue line while the hotter plasma is in red. Only one velocity curve is shown, as both plasmas use the same profile.

Feature	Model 1	Model 2	Model 3	Model 4
C - peak at 2+	0	1	1	1
C - peak at 4+	1	1	1	1
O - peak at 2+	0	1	1	1
O - peak at 6+	1	0	1	1
Si - peak at $\sim$ 7+	1	1	1	1
Broad Si Distribution	1	0	1	1
Fe - peak at $\sim$ 7+	1	0	1*	1
Fe - peak at $\sim$ 16+	1	0	1	1
Total	6	4	8*	8

Table 3.1: Summary of the different models' reproduction of the May 20, 2005 ACE/SWICS ICME observation. A score of 1 is given if the feature is present otherwise, a score of 0 is given. Model 1 uses a single hot plasma. Model 2 uses a single cold-dense plasma. Model 3 uses both the cold and hot plasma combined with a single mixing ratio. Model 4 uses both the cold and hot plasma combined with a mass dependent mixing ratio. The Fe^{7+} peak test for model 3 has an asterisk because there is an equally large peak at Fe^{5+} whereas ACE SWICS shows the coldest peak at Fe^{7+}

low charge state plasma observation of the ICME at ACE, along row A. Each column represents a different atomic species. Going from left to right we show carbon, oxygen, silicon, and iron. The model does replicate some of the features of the observation. Notably, we see the higher carbon and oxygen peaks of C^{4+} and O^{6+} as well as peaks in iron around Fe^{7+} and Fe^{16+}. In silicon we see a broad distribution and a peak near Si^{6+}. What is not reproduced are the cold charge states of carbon and oxygen, which are present in the ACE/SWICS observation. Table 3.1 summarizes the result of the eight qualitative tests for this simulation under the model 1 column. This simulation was able to reproduce 6 of the 8 features we highlighted, primarily lacking at recreating the cold lower mass ions.

Ionic charge states are known to freeze-in closer to the Sun for lower mass species (*Hundhausen*, 1972; *Buergi and Geiss*, 1986; *Geiss et al.*, 1995). For example, *Hundhausen* (1972) states that the oxygen charge state freeze-in around 1.2 $R_\odot$ while the iron charge state freezes-in further from the corona, between 2-3 $R_\odot$, with an ordering that remains even with more rapid expansion (*Geiss et al.*, 1995). In this

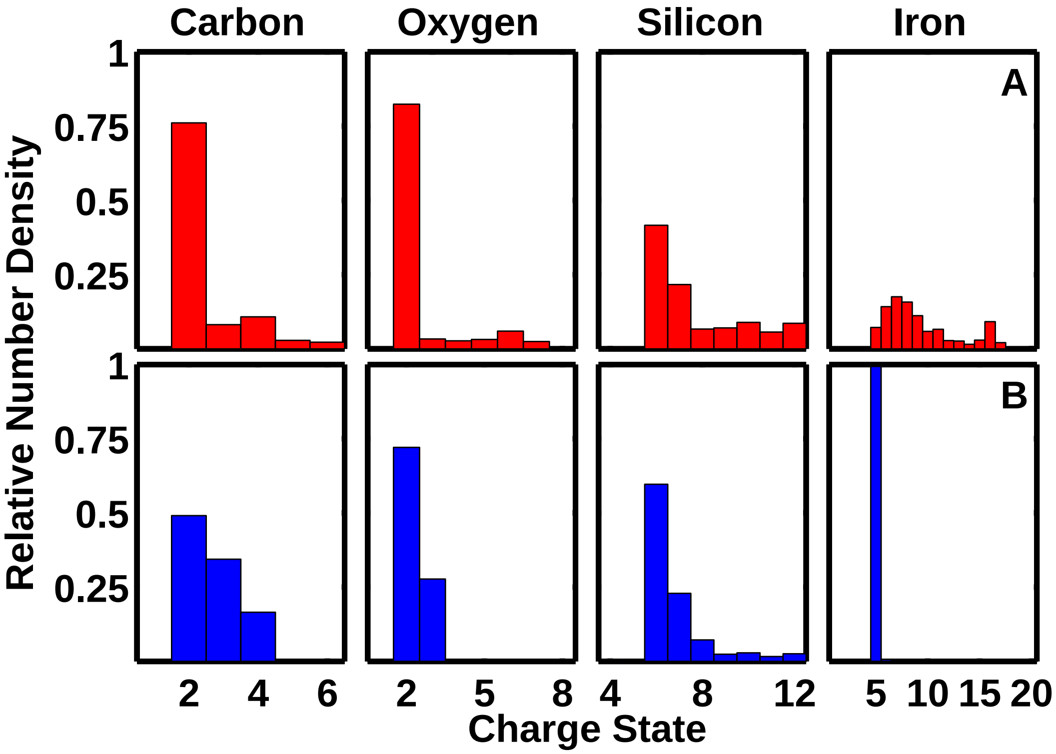

Figure 3.3: Comparison of ACE/SWICS charge state distribution and the initial charge state distribution for the modeled plasma. Row A shows the ACE/SWICS observations from the May 20, 2005 ICME. Row B shows the initial charge state distribution used for each modeled plasma.

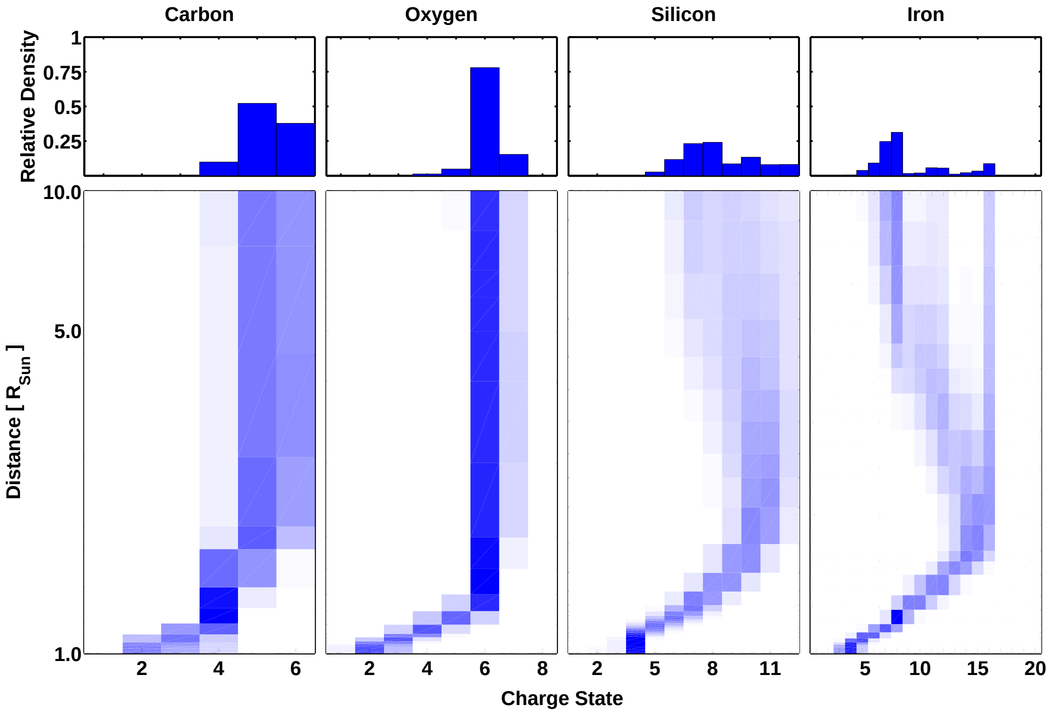

Figure 3.4: Result from the charge state evolution model using a hot, dense plasma for each of the atomic species modeled. Bottom row shows the evolution of the charge state distribution during the first $10R_{\odot}$ after ejection. The top row shows the resulting 1 AU charge state distribution.

simulation, the low mass species froze-in while the plasma was still very hot. The plasma was dense enough to allow ample cooling of the higher mass species resulting in the broader distribution of silicon and iron. Even during the abnormally cool iron charge state observations, there is often still a population of hotter Fe^{16+}, as can be seen in Figure 3.6.

A colder-dense single plasma simulation was also conducted in an attempt to reproduce the anomalously cool low mass charge states. The electron temperature and density profiles are shaped similarly as the previous case, however the temperature maximum is considerably cooler, with a temperature of $1 * 10^5 K$, while the density maximum is greater, with a density of $9.5 * 10^{10} cm^{-3}$. This temperature range is consistent with the analysis of (*Gilbert et al.*, 2012).The dashed blue curve in Fig-

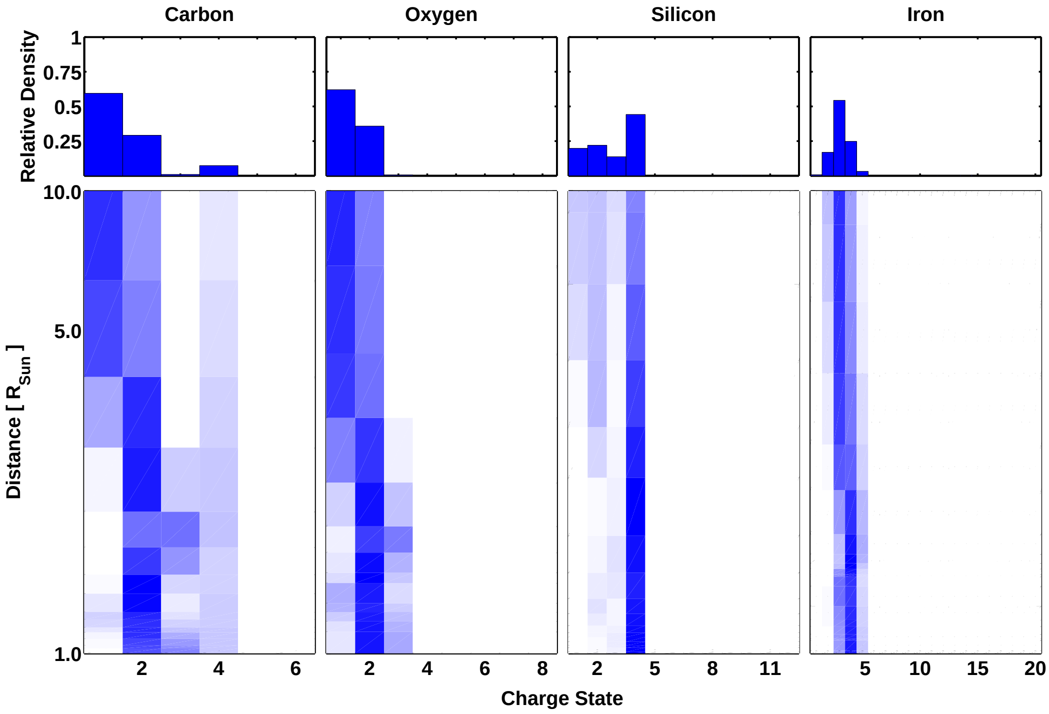

Figure 3.5: Result from the charge state evolution model using a colder-dense plasma for each of the atomic species modeled presented similar to Figure 3.4.

ure 3.2 shows the input electron density and temperature profiles, in panels A and B respectively. The velocity profile is identical to the previous simulation and lies along the red curve in panel C. The cold plasma is initialized with the same temperature and charge state distribution as the hot plasma model. Figure 3.5 shows the evolution of the charge state distribution in the low solar atmosphere. The charge state distribution stays close to the initial state while the plasma approaches the maximum temperature. Afterwards, the ions begin to transition to even colder states than initially present before freezing in.

Row C of Figure 3.6 shows the result of the colder single plasma simulation. In all four species, we see much colder distributions than previously seen in the hotter plasma simulation along row B. Qualitatively, the carbon distribution looks similar to the ACE/SWICS observation. A peak at C^{2+} and a minor peak at C^{4+} are both observed in the resulting model distribution. Additionally, the cold peaks of O^{2+} and Si^{6+} are also recreated in the model. However, the distributions for oxygen, silicon, and iron are much too cold compared to the ACE/SWICS observations. The model fails to recover the observed peak at O^{6+}, and the silicon and iron distribution are much too cold. It is important to remember that the charge state distribution range for the model results, plotted in Figure 3.6, are constrained to the charge states that are resolved in the triple-coincidence measurements from ACE/SWICS. The model results may have densities in colder charge states; however, due to this constraint the plots in row C show only density in charge state bins resolved in the ACE/SWICS dataset. Recently, *Gilbert et al.* (2012) has shown that in these cold charge state ICME events, singly charged ions are present in double-coincidence ACE/SWICS observations, consistent with the colder ions the model produces. Presently, only the triple-coincidence dataset will be considered. Table 3.1 summarizes the result of the eight qualitative tests under the model 2 column. This simulation only recreated 4 of the 8 features, lacking most of the hotter features.

3.4 Multiple Plasma Simulation

Following a notional model of prominence plasma mixed with hot cloud plasma, we now use a combination of two different plasma simulation results to replicate the ACE/SWICS observations. We used a hot plasma, such as one would find from flare heating associated with the eruption (*Reinard*, 2005; *Lynch et al.*, 2011), and a much denser but cooler plasma, such as the prominence material found in the CME core (*Rouillard*, 2011). Figure 3.2 shows the input profiles for both plasma populations. These are identical plasma profiles as described in the previous section. To determine the mixing ratio we perform a linear least square regression. This method calculates the total difference squared of the measured charge state distribution to the modeled distribution for all possible mixing ratios. We then select the mixing ratio that corresponds to the smallest difference between the observation and model. All four species were used in the solution vector to determine a single mixing ratio to reproduce the ACE/SWICS observations. The resulting mixing ratio is given in Equation 3.1.

$$Q_{\text{total}} = 0.930 * Q_{\text{ColdPlasma}} + 0.070 * Q_{\text{HotPlasma}} \tag{3.1}$$

The resulting combined distribution is plotted in Figure 3.6 on row D. Qualitatively, the multiple plasma solution is in agreement with the ACE/SWICS observations. We succeeded in reproducing low charge state carbon, oxygen, and iron concurrently with their high charge state counterparts. In the lower mass species, we are able to recreate a population of doubly charged carbon and oxygen ions while concurrently having a hotter population of carbon around 4+ and oxygen around 6+. Table 3.1 shows the results of the features we aim to replicate. The single mixing ratio simulation's scores are shown under the model 3 column. This model is able to reproduce all 8 features, however there is one major discrepancy in the reproduced charge states and those that are observed. Near the colder peak in the iron distribution we see that there are two noticeable populations. One is near Fe^{7+}, the peak location we are attempting to reproduce, while the other is at Fe^{5+} which is the location of the cutoff for the triple-coincidence dataset. This particular mixing ratio is causing an over-abundance of cold plasma to occur in the iron distribution. We interpret this to be caused by compositional differences between prominence and cloud-type data.

To test this assumption, mixing ratios for each species were determined using a linear least squares regression like before, but solving for mixing ratios for each species. Table 3.2 shows the mixing ratios we determined for each species. Due to the small charge state distribution range observable by ACE/SWICS for silicon, the majority of the modeled cold plasma falls in charge states not delivered in the triple-coincidence data. Therefore, the mixing ratio of iron is used for silicon. Row E in Figure 3.6 shows the resulting charge state distribution using the species dependent mixing ra-

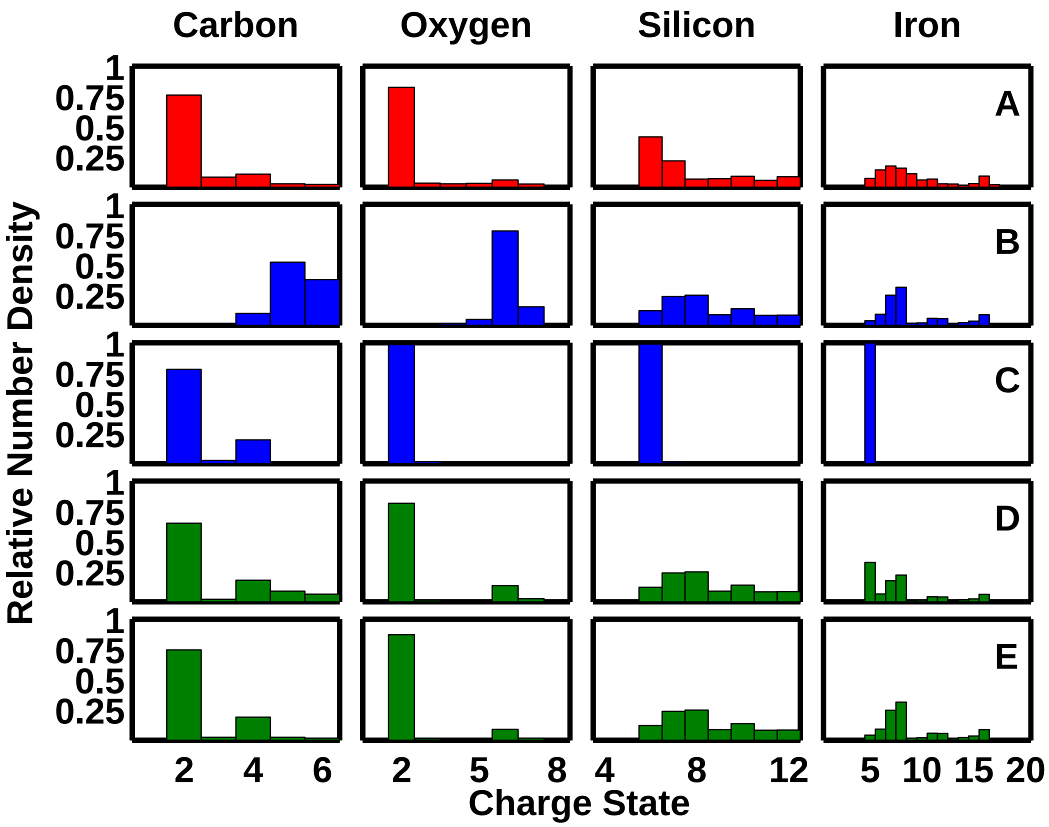

Figure 3.6: Comparison of ACE/SWICS charge state distribution and the charge state evolution model results, at 1 AU, for the four different atomic species, carbon, oxygen, silicon, and iron. Row A shows the ACE/SWICS observations from the May 20, 2005 ICME. Row B shows the model result of a single hot plasma. Row C shows the model result from a single cold dense plasma. Row D shows a combination of the hot and cold plasma model results using a single mixing ratio. Row E shows a combination of the hot and cold plasma model results using a mass dependent mixing ratio.

Species	Cold Plasma Contribution	Hot Plasma Contribution
Carbon	0.983	0.017
Oxygen	0.955	0.045
Silicon	0.104	0.896
Iron	0.104	0.896

Table 3.2: Mixing ratio determined for each species. The majority of the cold plasma modeled for silicon lies outside of the range of silicon charge states resolved for ACE/SWICS, therefore a mixing ratio isn't able to be calculated. The mixing ratio determined for iron is used for silicon as well.

tios. Comparing the resulting charge state distribution to that of the ACE/SWICS observations we see a very good qualitative match. All 8 of the features we are scoring are recreated in this model's resulting distribution like in the previous single mixing ratio text. A summary of the scores from our qualitative test are shown in Table 3.1 under the model 4 column. The cold iron peak no longer shows two populations, like the previous case. Now, only the peak near Fe^{7+} remains, consistent with our data.

3.5 Discussion

In the previous sections, we have shown that we can qualitatively recreate the observations of anomalously low charge state plasma from the May 20, 2005 ICME. Our first attempts involved modeling two different single plasma to test if the cold ion observations were a byproduct of the adiabatic cooling of the ICME as it expands into the heliosphere. We ran a variety of cold and hot models, with a range of expansion profiles, with a result: models based on the temperature history of one single plasma cannot produce concurrent hot and cold signatures, as observed.

This result is not entirely surprising when considering the ionization time scales for different mass ions. During its expansion into space, a given ion freezes in once its ionization time scale becomes greater than its expansion time scale. Lower mass species tend to freeze-in closer to the corona, with the freeze-in distance moving outwards as the mass of the species increases (*Geiss et al.*, 1995; *Buergi and Geiss*, 1986). In our ICME simulation, the presence of hot plasma requires heating very early on in the plasmas expansion history. In this case, carbon and oxygen charge state distributions freeze-in while the ICME plasma is still heating and therefore reflect these high temperatures. Furthermore, the plasma density may be large enough to allow the heavier species to recombine further out, relaxing into lower and cooler charge states, but successively losing high charge state signatures. Thus, we can conclude that low ionic charge state plasma seen in all four species in ICMEs cannot result strictly from expansion effects on a single plasma population. Similarly, in the case of the single cold case, the plasma never experiences a hot enough environment to produce ions in the higher charge states, such as those observed in the ICME observation.

We therefore conclude that our observations are reflective of the multi-temperature nature of CMEs observed at the Sun (*House et al.*, 1981): Cold ionic charge states originate in cool and dense prominence plasma. Hotter charge states come from cloud-plasma that is magnetically dominated. Combining these two solutions, we are able to qualitatively match the ACE/SWICS behavior in all four elements. These two plasma contributions mix during their heliospheric expansion, suggesting that prominence and cloud plasma are on the same field-lines in the corona, providing an important clue for the magnetic structure and relation of prominence plasmas and CME.

Prominences have been described as an important part of the initiation process of CMEs. One model suggests that prominences can act as an anchor, preventing the bent magnetic flux rope from ejecting (*Low*, 1999; *Low et al.*, 1982). As plasma drains from prominences under gravitational pull, the magnetic forces on the flux rope in the corona are no longer balanced forcing the CME to erupt, dragging the magnetically attached prominence with it (*Low et al.*, 2003). Through this process, prominences can lose $\sim 90\%$ of their mass (*Schmahl and Hildner*, 1977) as the material drains from the loops into the corona. Despite this the prominence plasma is still a significant portion of the ICME, accounting for an average of $\sim 20\%$ of the mass of the ejecta (*Gilbert et al.*, 2006). However, this model doesn't predict a mixing of the hot and cold plasma. During the eruption, a helmet streamer loop is ejected as the internal flux rope is propelled outward. The reconnection occurs low in the corona, to close the streamer loop, but does not necessarily connect the streamer fieldlines with the internal flux rope where the prominence is confined.

In prominence models by *Karpen et al.* (2001) and *Aulanier et al.* (2000), prominences form around a neutral line where the surrounding magnetic field is highly sheared. The breakout model of (*Antiochos et al.*, 1999) requires a similar magnetic configuration. They propose a multiflux system with neutral lines at the boundaries of sheared flux arcades. Prominence plasma is then confined in the regions along these neutral lines, called filament channels. As breakout reconnection occurs, the magnetic field of the closed corona can reconnect with the filament channel, placing prominence plasmas on the same fieldlines as the flux-ropes that are being formed as part of the reconnection process (*Lynch et al.*, 2004). This is consistent with our observations, which show that prominence and flux-rope plasmas are on the same fieldlines and can therefore mix.

Finally, we have shown that the best match of our model with our observations occurs when each species experiences a different mixing ratio. Table 3.2 shows the mixing ratios that we used. As can be seen, the lower mass species of carbon and oxygen are composed primarily of the cold prominence material while the heavier species, iron, is primarily composed of the hot leading edge plasma with a very small amount of prominence material. Gravitational forcing will act stronger on these heavier species than the lighter ones. Countering the forcing from gravity, the plasma also experiences collisional drag, from ions traveling along the magnetic field from the corona. However, for heavier species the gravitational force dominates the force from collisional drag. *Gilbert et al.* (2002) calculated the draining time scales for both hydrogen and helium in a prominence assuming both of these forces were acting on the plasma. They found that the heavier helium drains much more quickly than hydrogen. This is consistent with our resulting ICME observation. The charge state distribution of the lighter species is comprised of a larger percentage of prominence material than the heavier species.

CHAPTER IV

Studies Enabled by the Charge State Evolution Model

4.1 Introduction

The low corona is a critical location for the heating and acceleration of the solar wind, however the exact mechanisms governing these processes are still in question (*Edmondson*, 2012). *Parker* (1958) presented a solution for the propagation of a supersonic solar wind emanating from the heated solar corona, which was then confirmed by Mariner 10 observations while traveling to Venus (*Neugebauer and Snyder*, 1962). It was eventually observed that the velocity of the solar wind is bimodal, also showing a latitudinal dependence during solar minimum with fast wind over the poles and slow wind near the ecliptic plane(*McComas et al.*, 1995). These two solar wind types originate from different plasma environments as evidenced by their distinct elemental and ionic composition observed *in situ* (*Geiss et al.*, 1995; *Neugebauer et al.*, 2002; *Gloeckler et al.*, 2003). The supersonic solution of *Parker* (1958) has difficulty in creating the observed faster solar wind velocities, therefore an additional energy source must be present to further accelerate the solar wind (*Parker*, 1965). The exact nature of the coronal heating is not well understood, but is a central question which a number of MHD models are investigating (*Hansteen and Velli*, 2012, and references therein). Whatever the cause, if heating occurs before the plasma becomes frozen-in, the ramifications of the energization should be observed in the charge state distribution observed in the heliosphere.

The Charge State Evolution model (CSEVOL), discussed in chapters II and III, has been used to facilitate a number of investigations of the coronal environment. CSEVOL is a powerful tool capable of making estimates of the low coronal electron plasma environment as a function of height, constrained by *in situ* composition measurements. This technique enables the probing of a region of the Sun where *in situ* measurements are nearly impossible to obtain. Such estimations have been used to diagnose solar wind models (*Jin et al.*, 2012; *Zurbuchen et al.*, 2012), bridge the gap between spectroscopic measurements and *in situ* measurements (*Landi et al.*, 2012b), and as a tool to increase our understanding of the physical processes occurring close to the corona (*Landi et al.*, 2012a,c,d). Studies such as these can help constrain the energization mechanisms the corona.

In this chapter, we will discuss in further detail three of these studies where the use of the charge state model has played a critical role. First, we will discuss the contributions from CSEVOL towards determining the effectiveness of using carbon charge states as a solar wind diagnostic tool, presented in the study of *Landi et al.* (2012a). Then, we will discuss the study published in *Zurbuchen et al.* (2012) where CSEVOL was used, in part, to investigate the source environment of the solar wind. Finally, we will briefly discuss an innovative use of CSEVOL. Published in *Landi et al.* (2012b), we discuss a method to bridge the gap between spectroscopic observations of the solar atmosphere and *in situ* measurements.

4.2 The Effectiveness of Carbon Charge States as a Coronal Electron Measure

Gloeckler et al. (2003) has previously shown that the derived coronal electron temperature, from the O^{7+}/O^{6+} ratio *in situ*, is anti-correlated to the solar wind velocity and the derived solar wind type, separating the fast and slow wind observed by Ulysses *McComas et al.* (1995). Different wind source regions are characterized by different plasma environments which are then reflected in the charge state composition measured *in situ* (*Geiss et al.*, 1995; *Neugebauer et al.*, 2002; *Gloeckler et al.*, 2003). In the study of *Landi et al.* (2012a), we explore the robustness of the O^{7+}/O^{6+} ratio and the effects of the dynamic coronal plasma on the charge state composition.

Landi et al. (2012a) introduced a new analysis technique wherein data is converted into audible noise, through a process called sonification. Applying this technique on composition data measured by ACE/SWICS, we found a strong periodicity in the C^{6+}/C^{4+} ratio. Computing the Fourier analysis of the carbon ratio observed over the mission, we found that its fundamental frequency is 26.9 days which corresponds directly to the typical rotation speed for features on the sun located below 45 deg latitude. Making similar Fourier calculations of typical solar wind type indicators, such as the velocity of helium and the O^{7+}/O^{6+} ratio, yields the same periodicity with a frequency comparable to the solar rotation rate. The Fourier analysis implies that the C^{6+}/C^{4+} ratio is in fact another strong indicator of the type of plasma being observed, either fast or slow solar wind (*Geiss et al.*, 1995; *Neugebauer et al.*, 2002; *Gloeckler et al.*, 2003).

The ratio of oxygen charge states is traditionally used to estimate the coronal electron temperature at the freeze-in height. CSEVOL was used to investigate the robustness of the freeze-in temperature derived from different carbon ionization states. Since CSEVOL requires a prescribed plasma environment to perform the calculations,

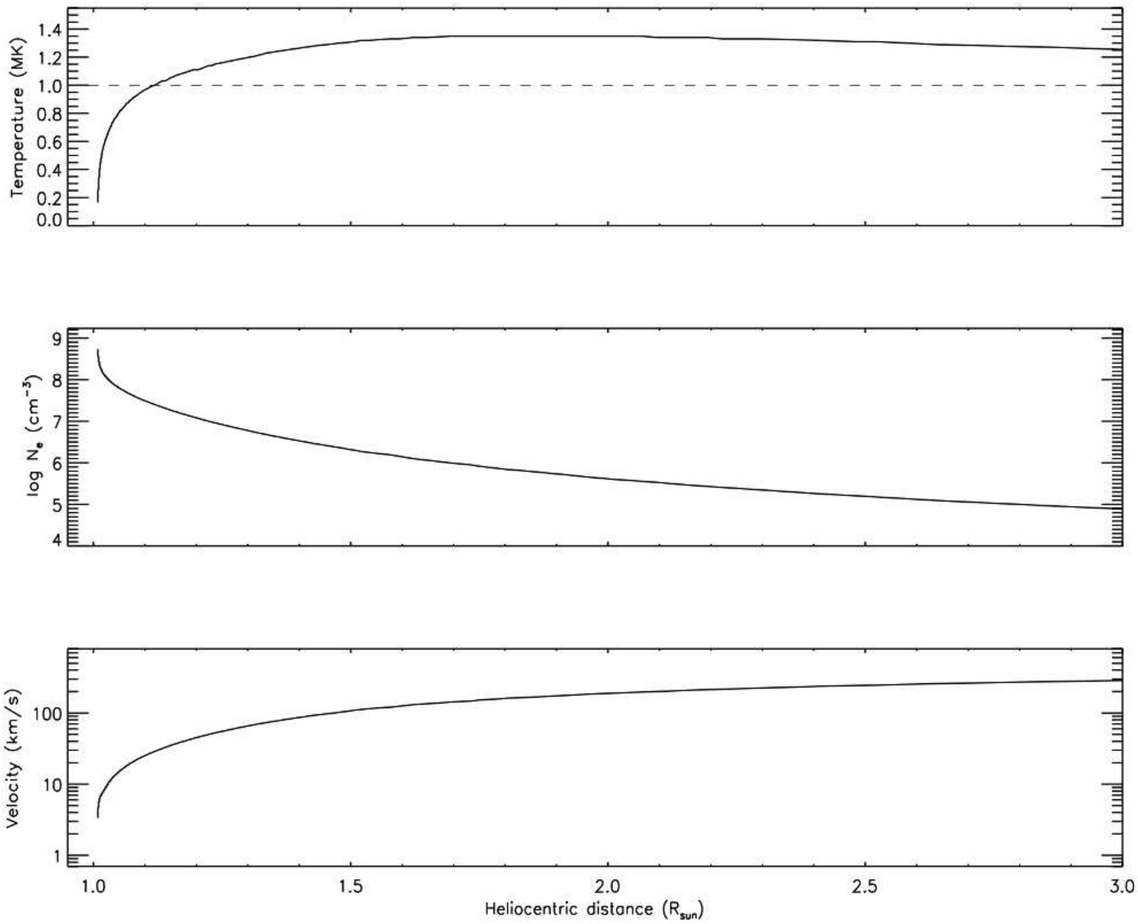

Figure 4.1: CSEVOL input profiles of electron temperature, density and bulk plasma velocity, provided by the *Cranmer et al.* (2007) solar wind model. Figure published in *Landi et al.* (2012a).

the solar wind model of *Cranmer et al.* (2007) was selected to provide the electron temperature, density, and bulk velocity profiles. Figure 4.1, published in (*Landi et al.*, 2012a) shows the input profiles to CSEVOL from the surface of the Sun out to 5 $R_\odot$, further out from the Sun than the freeze-in height for most ionic species. The profile displayed was calculated from a magnetic flux tube which had a footpoint in a coronal hole, yielding fast wind.

The results from the charge state model gives us insight into the behavior of the charge state distribution very close to the sun. First, we determine the freeze-in height of the charge state distribution for each species by finding the distance at which each species relative abundance is within 10% of its final frozen-in value. Each ion species becomes freezes-in at different heights, within first 5 $R_\odot$ (*Hundhausen et al.*, 1968). We found that both the carbon and oxygen compositions were frozen-in within 2 $R_\odot$. Additionally, we observed that the individual ionic species of each element became frozen-in at different heights, as expected. The carbon species freeze-in close to each other in height, varying between 1.24-1.62 $R_\odot$, while the oxygen states freezes-in further apart, varying between 1.02-1.62 $R_\odot$.

These varying freeze-in distances have strong implications on the calculation of the coronal electron temperatures. Traditionally, the temperature is determined by calculating the ratio of two ions and solving the charge state conservation equation, assuming collisional equilibrium (*Geiss et al.*, 1995), which in turn provides an estimate of the coronal temperature at the site where the two ion species froze-in. However, the individual ionic species are shown to freeze-in at different distances, meaning that the traditional coronal electron temperature calculation uses a mix of ions which freeze-in at different heights and different temperatures. To determine the strength of the effect of varying freeze-in heights on the calculated electron temperatures, we compare the input electron temperature from the *Cranmer et al.* (2007) model, to the electron temperatures calculated assuming collision equilibrium from a variety of ratios of species ratios as a function of height above the corona.

Figure 4.2, published in *Landi et al.* (2012a), shows the comparison between the electron temperature from *Cranmer et al.* (2007), also used as the input for the charge state model, and the electron temperatures calculated from various ionic ratios of carbon and oxygen as a function of heliocentric distance. The blue lines represent different oxygen ionic ratios while the red lines represent different carbon ratios. It can be seen that both the carbon and oxygen ionic ratios correspond to temperatures lower than the *Cranmer et al.* (2007) model temperature at most distances. O^{5+}/O^{6+} matches the initial electron temperature very close to the surface, but it diverges

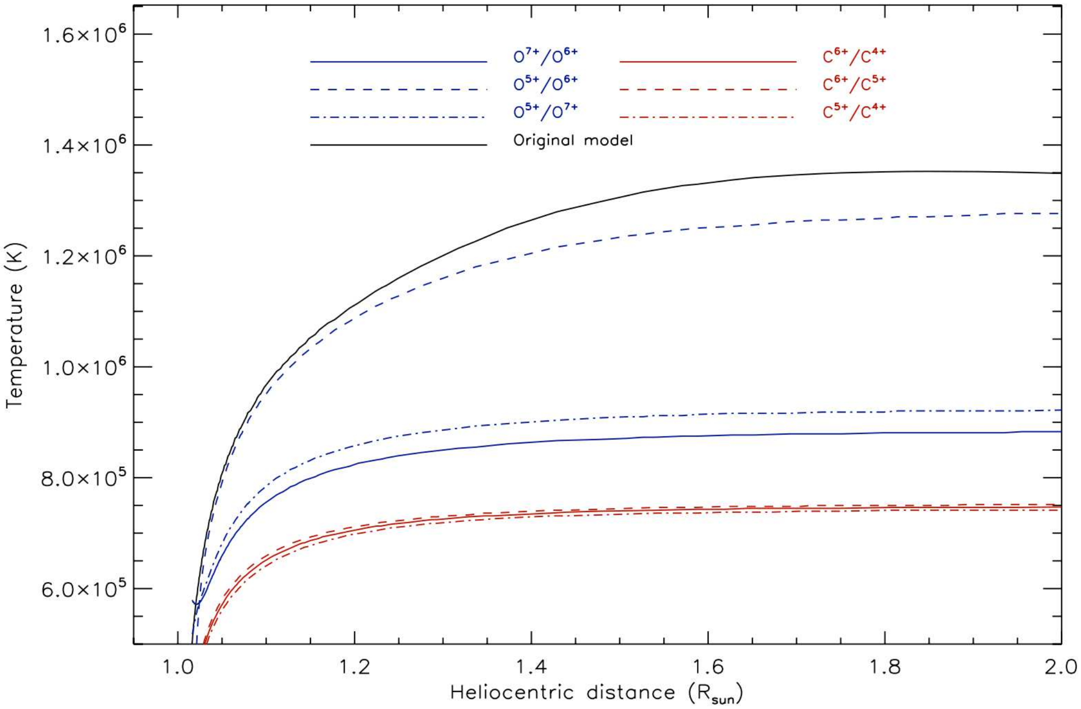

Figure 4.2: Electron temperature calculated from CSEVOL model output using the ionic ratios of different oxygen and carbon species at varying heliocentric distance. Also plotted is the temperature determined from the *Cranmer et al.* (2007) model which was used as the input for CSEVOL. Figure published in *Landi et al.* (2012a).

rapidly higher in the corona and underestimates the electron temperature similar to the behavior of the other ratios. Additionally, we see that the calculated temperatures from the oxygen ratios vary significantly, depending on which ionic species were used. However, the temperatures calculated from carbon ratios are similar to each other, regardless of the ionic species used.

Ionic ratios have been shown to be strong indicators of solar wind type (*Geiss et al.*, 1995; *Neugebauer et al.*, 2002; *Gloeckler et al.*, 2003), as well as a probe of the coronal plasma environment where the species become frozen-in (*Hundhausen et al.*, 1968; *Geiss et al.*, 1995). Motivated by the auditory analysis, which concluded that carbon ionic ratios could be very effective discriminators of solar wind type, similar to the commonly used O^{7+}/O^{6+} ratio, we used CSEVOL to investigate the behavior of the carbon ion species as they evolve from the corona. We found that carbon ions tend to freeze-in at heights much closer together than oxygen species. These have important implications on the accuracy of these ionic ratios to calculate the local freeze-in temperature in the corona. As stated in *Landi et al.* (2012a), we conclude that not only can carbon ion ratios be used as effective indicators of solar wind type, and thereby the source location of the plasma, but they also are a more robust indicator of the freeze-in temperature in the corona.

4.3 Constraints on the Solar Wind

In *Zurbuchen et al.* (2012) we present a study which in part uses the CSEVOL model in order to investigate the source environment of the solar wind by matching compositional observations from the Solar Wind Ion Composition Spectrometer (SWICS) (*Gloeckler et al.*, 1992) on the Uylsses spacecraft (*Wenzel et al.*, 1992). Slow solar wind is observed to have much more variability in time and space (*von Steiger et al.*, 2010). The mechanism which the slow wind escapes from the closed magnetic field region into the heliosphere is still in question, but regardless of the mechanism an amount of heating and acceleration must occur to the plasma in the corona to produce the *in situ* observations.

A number of solar wind models, such as those by *Hansteen and Leer* (1995), *Cranmer et al.* (2007), and *van der Holst et al.* (2010), have attempted to determine the physical process at play in the heating of the solar wind. Comparing *in situ* composition measurements from Ulysses/SWICS to results from CSEVOL we are able to explore the effectiveness on these solar wind models in their ability to match the heating the solar plasma. We used results from a number of current solar wind models (*Hansteen and Leer*, 1995; *Cranmer et al.*, 2007; *van der Holst et al.*, 2010) to provide the electron density and temperature and flow velocity profiles required by CSEVOL. Comparisons of the charge state distribution calculated from solar wind models to *in situ* data illustrates the accuracy in a solar wind models ability to estimate the near sun environment, where any energization process would be occurring to the plasma. The estimated plasma environment will set the observed *in situ* charge state distributions at 1 AU, providing a new constraint on solar wind models. Figure 4.3, published in *Zurbuchen et al.* (2012), shows a set of input electron temperature, density and bulk flow velocity profiles, which were used as input for CSEVOL. This particular profile was calculated from the *Hansteen and Leer* (1995) model. The red curves denote a fast solar wind stream, from a coronal hole, while the blue curves denote slow solar wind, originating from a streamer.

Charge state distributions were calculated for carbon, oxygen, silicon and iron, for both fast and slow wind solutions from these solar wind models. The charge state distribution evolution was calculated from the corona through the heliosphere to 1 AU. Figure 4.4, published in *Zurbuchen et al.* (2012), shows the resulting evolution of the fast coronal hole wind using the input profile from the *Hansteen and Leer* (1995) model. The bottom row shows the evolution for each atomic species through the first 5 $R_\odot$. During this period, each element becomes frozen-in and thus remains constant

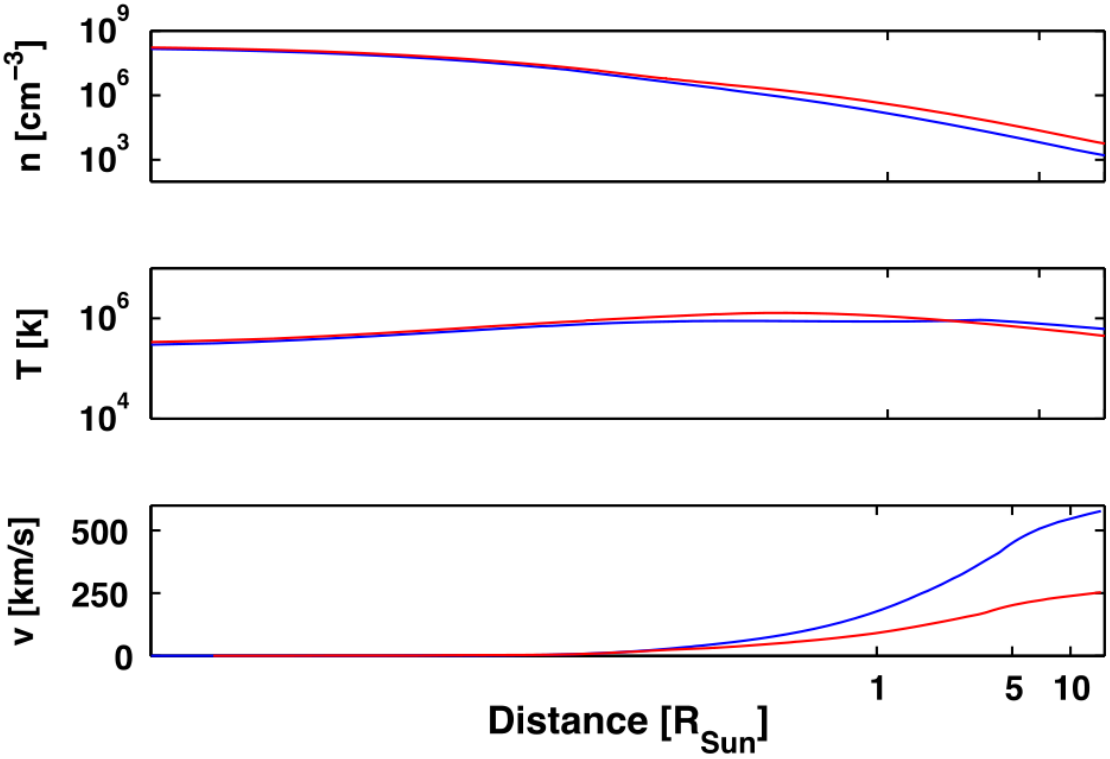

Figure 4.3: CSEVOL input parameters of electron temperature, density, and bulk plasma velocity. The red curves denote fast solar wind and the blue curves denotes slow solar wind. These curves are calculated from the model of *Hansteen and Leer* (1995). Figure published in *Zurbuchen et al.* (2012).

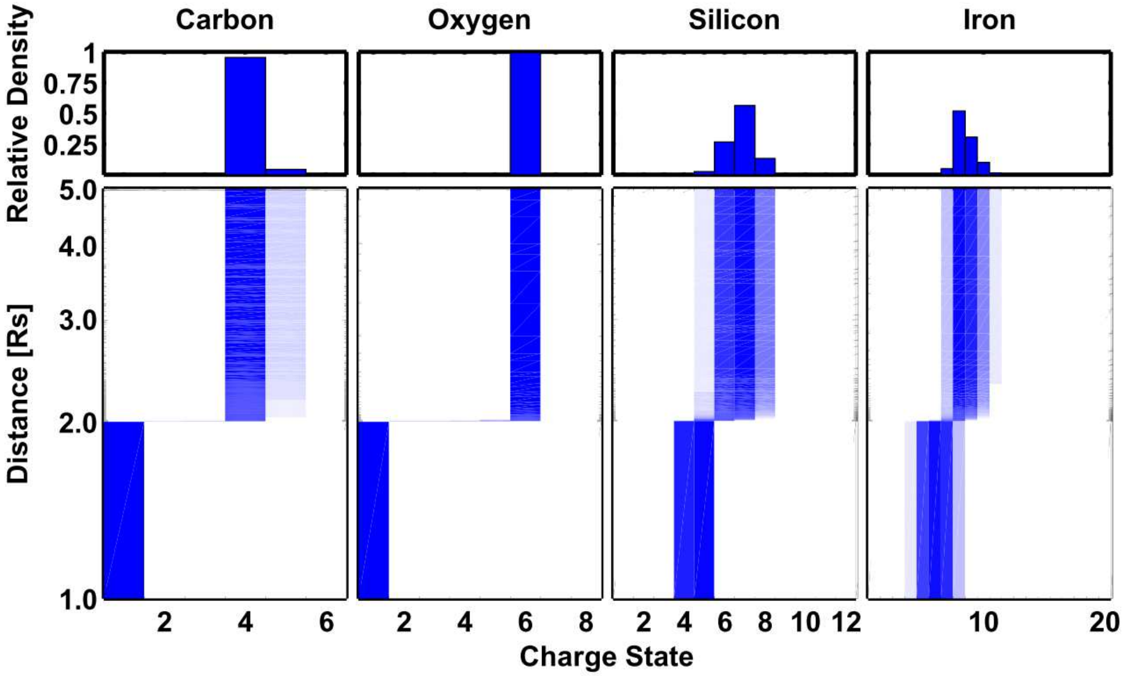

Figure 4.4: The computed charge state evolution for carbon, oxygen, silicon, and iron of the fast solar wind profile presented in Figure 4.3. The top row shows the frozen-in charge state distributions at 1 AU. The bottom row shows the evolution of the distributions throughout the first 5 solar radii. Within this range the elements become frozen-in. Figure published in *Zurbuchen et al.* (2012).

for the rest of the evolution. The top row shows the charge distribution for each species as it would be measured at 1 AU. Figure 4.5 , published in *Zurbuchen et al.* (2012), shows the evolution from a slow wind profile, also computed by the *Hansteen and Leer* (1995) model. Figure 4.5 is presented in a similar format as Figure 4.4.

In both Figures 4.4 and 4.5, we see that the charge state distribution for each species is indeed frozen-in close to the corona, as is expected (*Hundhausen et al.*, 1968). Comparing the top row from both igures, we see the expected compositional difference between the two solar wind types. In Figure 4.4 we see that the composition has a larger distribution of cooler charge state ions, which would be expected from the fast wind which originates from the relatively cooler coronal holes (*Geiss et al.*, 1995). Figure 4.5 shows an ionic composition that is representative of hotter plasma

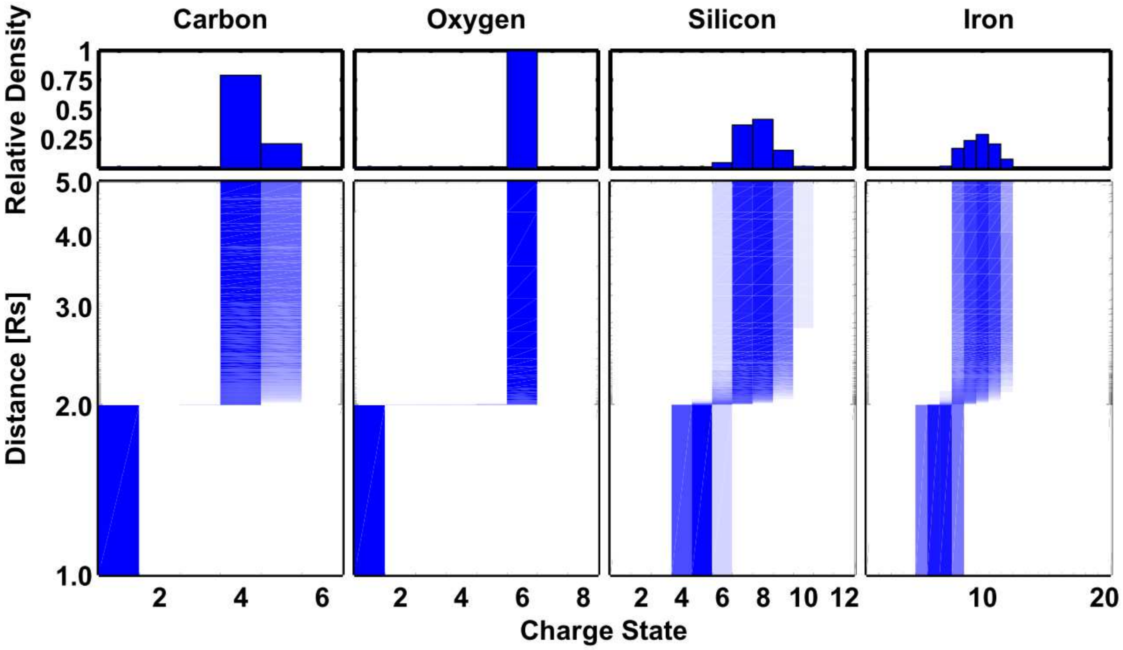

Figure 4.5: The computed charge state evolution for carbon, oxygen, silicon, and iron of the slow solar wind plasma presented in Figure 4.3. This data is presented similar to that of Figure 4.4. Figure published in *Zurbuchen et al.* (2012).

temperatures compared to the resulting composition modeled from inputs from the fast wind model. Hotter plasma such as this is expected, as slow streamer-type wind is strongly correlated to hotter charge states (*von Steiger et al.*, 2000). Next, we compare the model results to Ulysses/SWICS observations. Two hour accumulations of the Ulysses/SWICS data are used, separating the measurements into coronal-hole type and streamer type based on the carbon and oxygen composition (*von Steiger et al.*, 2010).

Figure 4.6, published in *Zurbuchen et al.* (2012), shows the Ulysses/SWICS composition observations from coronal-hole wind along with the results from the charge state evolution using fast wind profile from the *Hansteen and Leer* (1995) solar wind model. Panel A shows the comparison of the helium velocity (V_{He}) to $log(O^{7+}/O^{6+})$. Panels B, C, and D show the average charge state of carbon, silicon, and iron, respectively, versus $log(O^{7+}/O^{6+})$. In these three panels, the blue triangle on the left of the plot represents the average charge state calculated from the charge state model. It can be seen that the average charge state from the model solution underestimated the composition when compared to the observations. In other words, the solar wind model's freeze-in temperatures are much cooler than those observed from the Ulysses/SWICS measurements. Using the oxygen ratio as an example, the freeze-in temperature from the model is estimated to be $T_{\mathrm{f}} = 0.65MK$ while the temperature calculated from the data is around $T_{\mathrm{f}} = 1.1MK$ (*Zurbuchen et al.*, 2012). Comparing the model's freeze-in temperature to the input electron temperature profile, shown in Figure 4.3 along the blue curve, we see that the estimated temperature from the oxygen ratio is much cooler than the profile used as input to CSEVOL. This discrepancy is caused by high speeds in the *Hansteen and Leer* (1995) model close to the corona. The plasma is moving too fast for the evolving charge states to adapt to the electron environment (*Zurbuchen et al.*, 2012). A similar comparison was conducted using the solar wind models of *Cranmer et al.* (2007); *van der Holst et al.* (2010) and the same result was

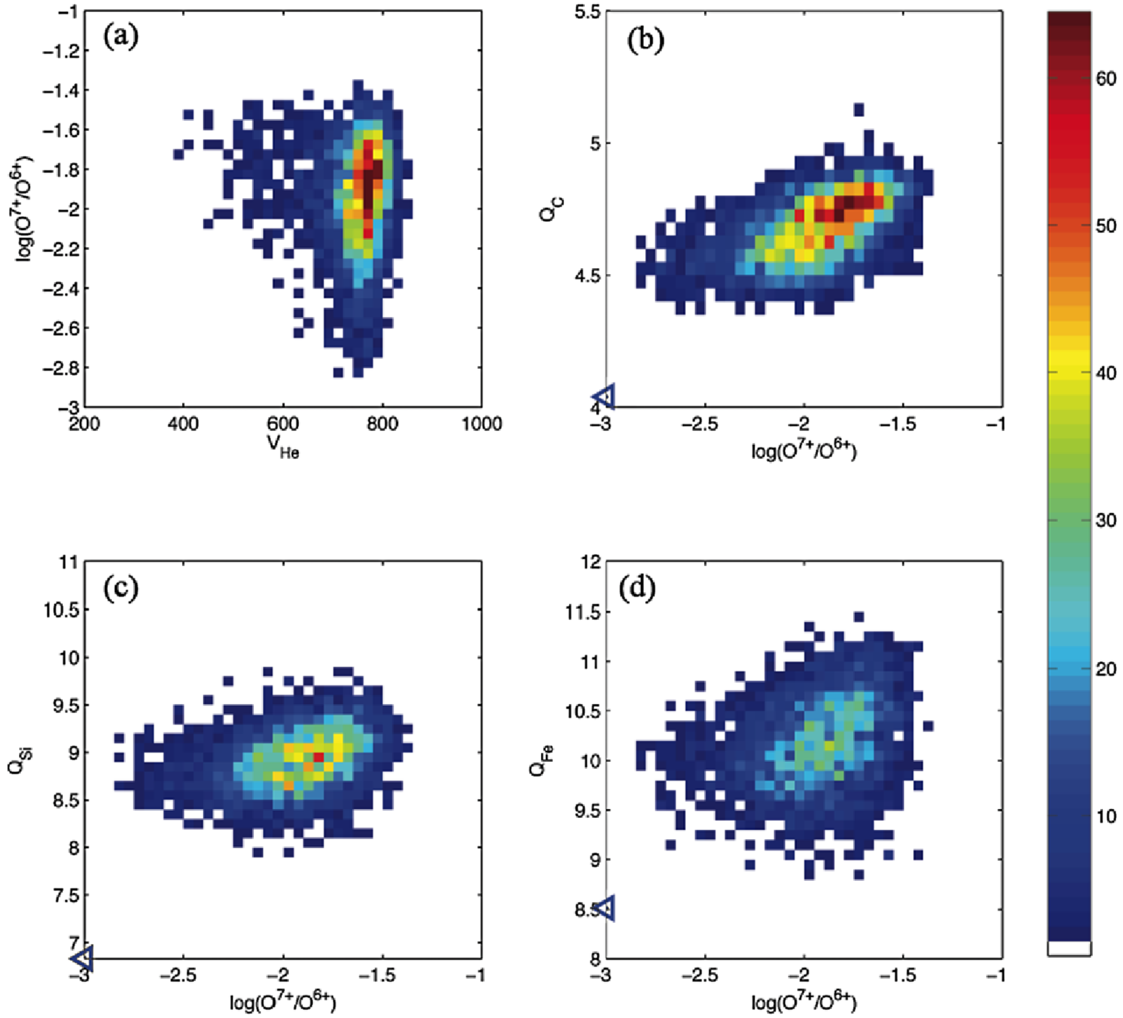

Figure 4.6: Ulysses/SWICS observations of the ionic composition of *in situ* fast solar wind compared with the charge state composition computed from the *Hansteen and Leer* (1995) model. Panel A shows the $log(O^{7+}/O^{6+}$ observations versus the velocity of helium (V_{He}). Panels B-D show the average charge state for carbon (Q_{C}), oxygen (Q_{O}), and iron (Q_{Fe}), respectively, each versus $log(O^{7+}/O^{6+}$. The average charge state determined from the charge state model is denoted by the blue triangles. Figure published in *Zurbuchen et al.* (2012).

observed. The model's charge state composition was cooler than that of the Ulysses observations.

Figure 4.7, published in *Zurbuchen et al.* (2012), shows a comparison of composition measurements from Ulysses/SWICS to the charge state model results for slow streamer wind, in a similar format to Figure 4.6. In panels B-D, the average charge states from the evolution model are denoted by red triangles on the left side of the plots. Once again, in panels B and C, we see that the charge states calculated from the *Hansteen and Leer* (1995) model are cooler than those observed by Ulysses/SWICS. Panel D however shows that the modeled iron charge state is actually in good agreement with the observations. Once again, the calculated freeze-in temperatures from the model charge states, of carbon and oxygen, is less than the freeze-in temperature calculated from the data. For oxygen, the model estimates a temperature of $T_{\mathrm{f}} = 0.85$ MK while the data estimates temperatures ranging $T_{\mathrm{f}} = 1.3 - 1.7$ MK (*von Steiger*, 2008). The iron temperature determined from the model is comparable to the data, both around $T_{\mathrm{f}} = 1.1$ MK. Carbon and oxygen charge states freeze-in much closer to the sun and, in the model, are moving too fast to adapt to the surrounding environment before freezing-in (*Zurbuchen et al.*, 2012). The iron state, which freezes-in further from the Sun (*Geiss et al.*, 1995), coupled with the slower velocity of the streamer wind model, has time to adapt to the environment and reflect the Ulysses/SWICS observations. This same result was observed using a number of different solar wind models as the input to CSEVOL.

Comparing the CSEVOL results from a number of solar wind models to the Ulysses/SWICS observations we find that the resulting charge state distributions from the solar wind models tend to underestimate the composition of the plasma, consisting of cooler ions than those observed *in situ*, for both coronal-hole and streamer wind. These cooler ionic compositions are not due to the temperature of the corona calculated from the solar wind models, as these tend to be within the values that are

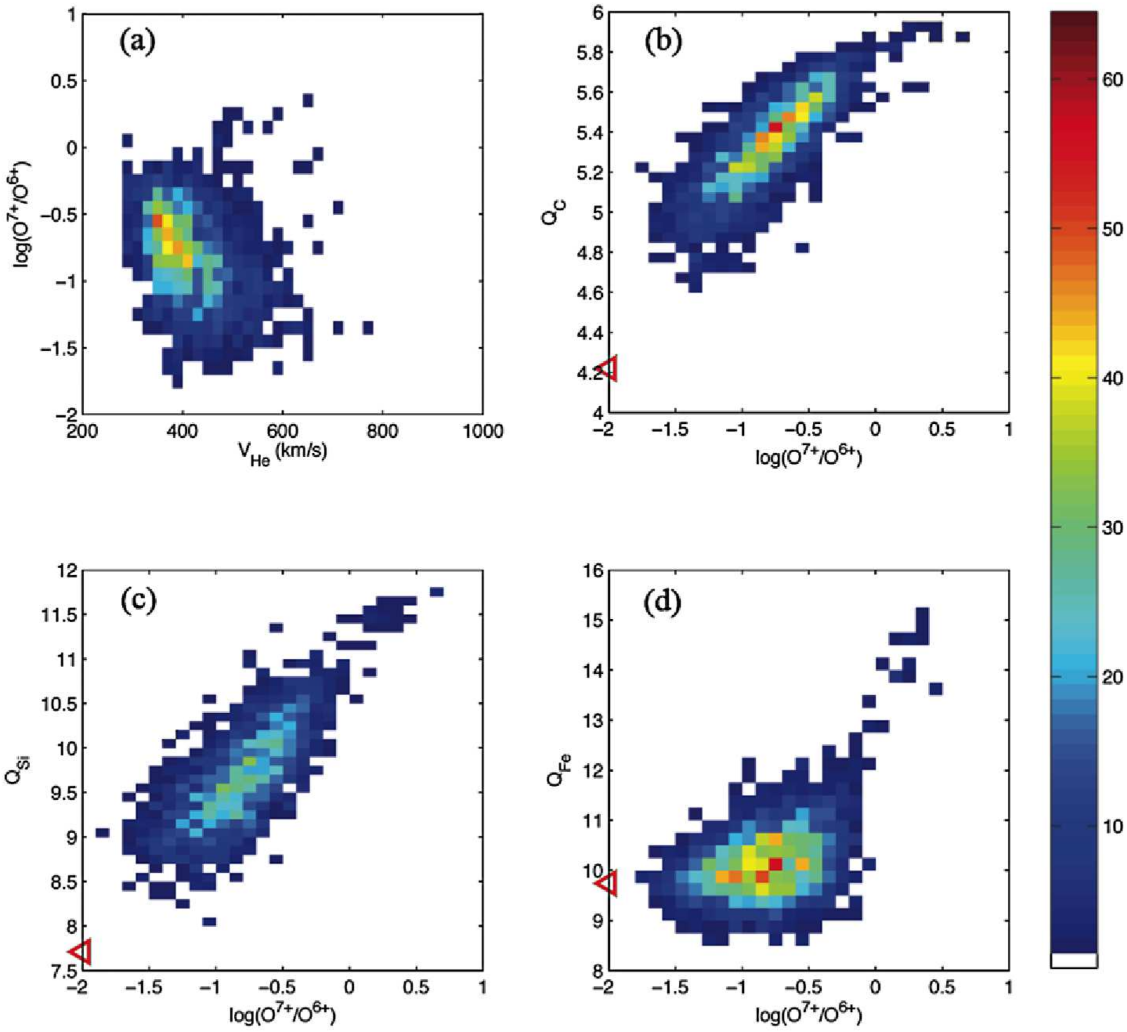

Figure 4.7: Ulysses/SWICS observations of the ionic composition of *in situ* slow solar wind compared with the charge state composition computed from the *Hansteen and Leer* (1995) model. We present this data similar to Figure 4.5. The average charge state determined from the charge state model is denoted by the red triangles. Figure published in *Zurbuchen et al.* (2012).

calculated from composition observations, namely $T \sim 1$ MK. More likely, the early coronal flow velocities predicted by the solar wind models we considered (*Hansteen and Leer*, 1995; *Cranmer et al.*, 2007; *van der Holst et al.*, 2010) are too high. This causes the plasma to flow quickly out of the corona leaving little time for the charge states to adapt to the environment. In turn, the charge states distributions predicted would reflect a distribution frozen-in deeper in the corona than what is observed to occur (*Zurbuchen et al.*, 2012).

4.4 Bridging the Gap Between Spectroscopic and *in situ* Measurments

CSEVOL, up to this point, has been used with prescribed electron temperature, density, and flow velocities, determined either through trial-and-error or from a solar wind model, to predict the *in situ* charge state distribution for comparison with observations. Comparing these results to ionic measurements has enabled new constraints on the early coronal environment. *Landi et al.* (2012b) discusses two innovative methods to incorporate spectroscopic measurements into this process. Spectroscopic measurements can determine the composition of the plasma close to the corona based on the strength of various emission lines of radiation. One method will be used to robustly validate solar wind models, from the corona throughout the heliosphere. The other method will use a trial-and-error method to determine the best profile to bridge the composition measurements remotely obtained in the corona to *in situ* measurements in the heliosphere when the two observations can be obtained in quadrature.

Landi et al. (2012b) demonstrates a proof of concept of one of these methods by investigating the coronal wind and equatorial wind models of *Cranmer et al.* (2007). At 1 AU, the predicted charge states from CSEVOL are compared to characteristic *in situ* observations obtained from SWICS on the ACE spacecraft. Similar to the *Zur-*

buchen et al. (2012) results, we observed discrepancies between the predicted charge states and the observations, due to the flow velocity in the corona from the model. In the corona, synthetic emission lines were computed based on the charge state evolution. These emission lines were compared to coronal hole and equatorial observations from the EUV Imaging Spectrometer (EIS) (*Culhane et al.*, 2007) onboard Hinode and the Solar Ultraviolet Measurements of Emitted Radiation (SUMER) (*Wilhelm et al.*, 1995) instrument onboard SOHO. The charge state model was shown to estimate line intensities closer to those observed in the corona than intensities calculated from a LTE calculation. The deviation from the spectroscopic observations is also caused by the MHD model's overestimation of the coronal flow velocities. *Landi et al.* (2012b) was only an initial demonstration, but has shown that CSEVOL, and similar charge state models, can be used to fill in the gaps between spectroscopic and *in situ* composition measurements producing stronger constraints and estimates on the plasma environment from the corona throughout the heliosphere.

CHAPTER V

The Wind/STICS Data Processor

In this chapter, we will discuss the method we use to process data from the Suprathermal Ion Composition Spectrometer (STICS) onboard the Wind spacecraft. We first provide an overview of the satellite's mission, followed by details of the instrument itself. Then, we discuss the process we employ to calculate distribution functions for various ionic species from the particle counts observed by the instrument. Finally, we discuss a novel method we have begun to use to contend with the intermittent nature of the data.

5.1 The Wind Mission

The Wind spacecraft began operating nearly 20 years ago. It was launched on November 1, 1994 and started its data collection shortly thereafter. Wind is one of two missions that make up the Global Geospace Science (GGS) initiative, the United States contribution to the International Solar Terrestrial Physics (ISTP) program. Prior to this, many spacecraft missions worked independently to make observations with different individual focuses. Wind, combined with its sister spacecraft POLAR, were designed to investigate the solar-terrestrial system together, with a main emphasis on the flow of energy, mass, and momentum in the geospace environment (*Acuña et al.*, 1995). Geospace refers to both Earth's magnetosphere and the nearby heliospheric environment. To accomplish a thorough investigation of this environment, Wind observes the upstream region of the magnetosphere and bow shock while POLAR observes the Earth's magnetosphere via a polar orbit. In addition to these two spacecraft, the ISTP program includes contributions from a number of international space agencies. The European Space Agency (ESA) provided SOHO and CLUSTER, the Japanese Institute of Space and Astronautical Science (ISAS), now combined with the Japanese Aerospace Exploration Agency (JAXA), provided GEOTAIL, and the Russian Space Agency provided INTERBALL (*Acuña et al.*, 1995; *Chotoo*, 1998). These missions combined to provide a global view of the entire solar-terrestrial system, ranging from remote observations of the Sun, to *in situ* measurements in the deep tail of the Earth's magnetosphere.

Wind, as seen in Figure 5.1, is equipped with a series of instruments to investigate the magnetic field, waves and the plasma environment, including solar wind and energetic particles. Wind is a cylindrical spin-stabilized spacecraft, with its spin axis oriented perpendicular to the ecliptic plane. The spacecraft spins at an angular speed of twenty rotations per minute (*Harten and Clark*, 1995). Initially, Wind launched with a three year mission plan, composed of a series of orbits enabling observations both upstream and downstream of the Earth's bowshock. This was accomplished through a number of petal orbits, utilizing lunar swingbys (*Acuña et al.*, 1995). The initial mission orbits are shown in Figure 5.2.

In 1997, the spacecraft was originally planned to enter into a halo orbit about the 1st Langragian Point (L1), approximately 240 Earth radii upstream from the Earth, along the Sun-Earth line. Here it would begin to monitor the solar wind environment continuously. This plan was changed however, and Wind continued sampling the magnetosphere and upstream conditions with another series of petal orbits, taking the spacecraft through the magnetosheath and bow shock and eventually further downstream the magnetotail. Beginning in 2001 and lasting until late 2003, Wind x

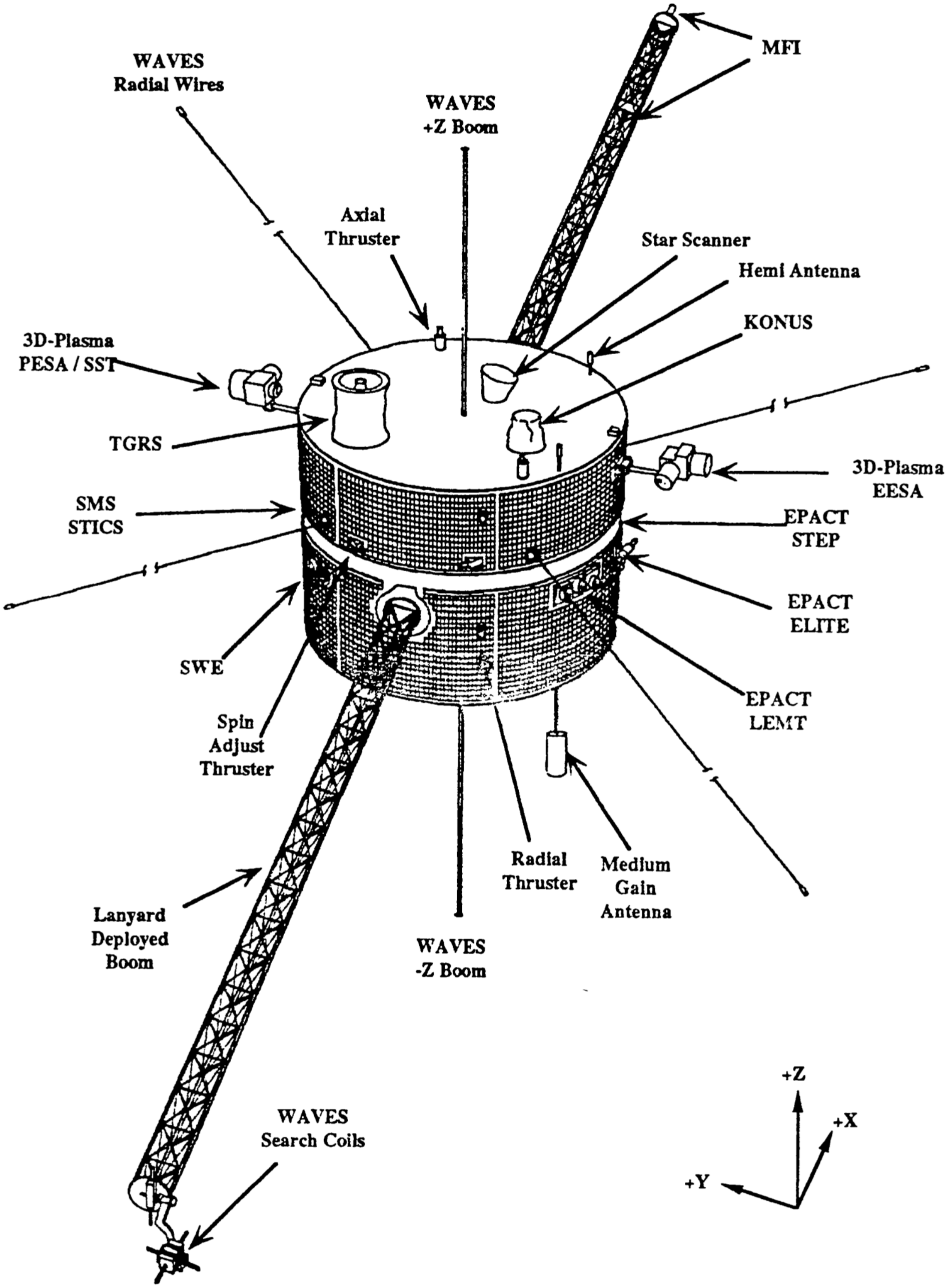

Figure 5.1: Illustration of the Wind spacecraft. The location of its instruments are indicated. Published in *Harten and Clark* (1995)

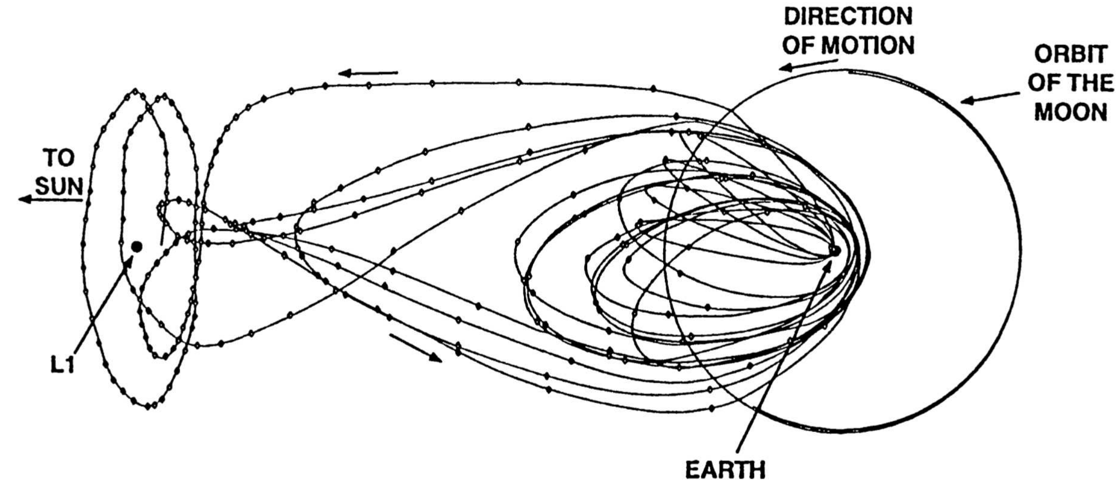

Figure 5.2: Illustration of the initially planned orbit for Wind. Shown, is the orbit projected on the GSE X-Y plane. Published in *Acuña et al.* (1995)

began prograde orbits, taking it far from the Earth along a direction perpendicular to the Sun-Earth axis. A diagram of this orbital phase is shown in Figure 5.3. In late 2003, the Wind spacecraft performed a deep magnetotail transit, traveling further than 200 Earth radii downstream in the magnetotail, before finally moving out to orbit L1 in mid 2004. Since then, Wind has continually monitored the solar wind upstream of the Earth.

As previously mentioned, for nearly 20 years the Wind spacecraft has been providing a number of different observations from a variety of plasma environments and solar conditions using eight different instruments, composed of twenty-four different sensors (*Acuña et al.*, 1995; *Chotoo*, 1998). The magnetic field is observed using the Magnetic Field Investigation (MFI) instrument (*Lepping et al.*, 1995). Radio and plasma waves, that occur throughout the geospace environment, are observed with the Radio and Plasma Waves Investigation (WAVES) (*Bougeret et al.*, 1995). Particles are measured over a large range of energies from the six other instruments. Low energy bulk plasma, from 7 ev to 22 keV, is observed by the Solar Wind Experiment (SWE) (*Ogilvie et al.*, 1995) while the 3-D Plasma (3DP) instrument (*Lin*

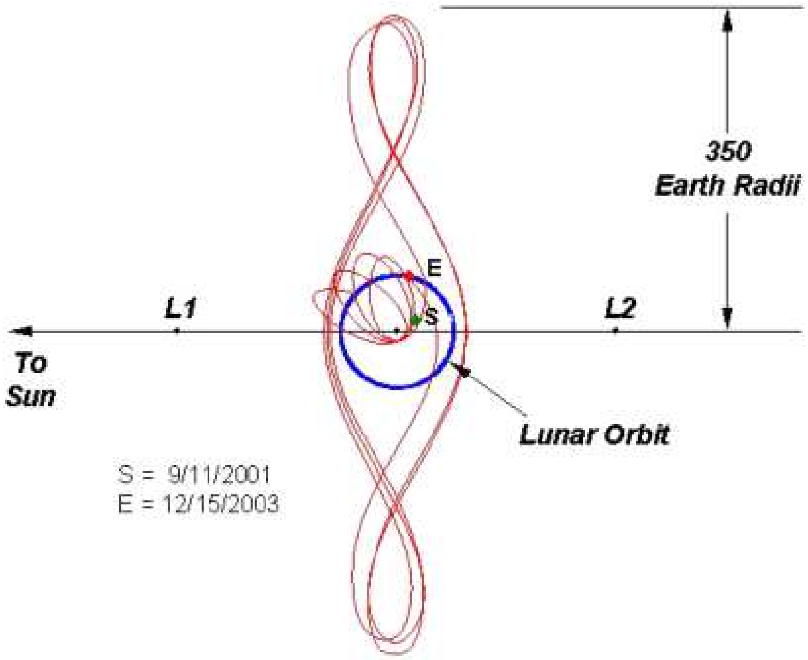

Figure 5.3: Illustration of the Wind prograde orbit from mid-2001 to late 2003. Shown, is the orbit projected on the GSE X-Y plane. Plot obtained from the wind.nasa.gov/orbit.php site.

et al., 1995), provides three-dimensional distribution information for plasma in this energy range. Energetic particle distributions are observed between the energies of 0.2 – 500 MeV with the Energetic Particles: Acceleration, Composition Transport (EPACT) instrument (*von Rosenvinge et al.*, 1995). Gamma-rays are observed on-board Wind from two separate instruments: the Transient Gamma-Ray Spectrometer (TGRS) (*Palmer et al.*, 1995) and the Konus experiment (*Aptekar et al.*, 1995). Finally, the composition of the heliospheric plasma from the bulk solar wind through the suprathermal tail is observed with the Solar wind/Mass Suprathermal ion composition studies (SMS) instrument suite (*Gloeckler et al.*, 1995). For the remainder of this chapter, we focus on the data from the suprathermal ion population observed from the Suprathermal Ion Composition Spectrometer (STICS), which is part of SMS (*Gloeckler et al.*, 1995).

5.2 The Suprathermal Ion Composition Spectrometer (STICS)

STICS is a time-of-flight (TOF) mass spectrometer, capable of measuring independently an incoming particle's mass, charge state, and energy. A diagram of the instrument is shown in Figure 5.4. Particles enter through the instrument aperture and immediately pass through an electrostatic deflection system. Here, an electric potential is imposed on two curved plates which the particle passes between. This potential causes the particle's path to be deflected, allowing only ions with a specific energy-per-charge (E/Q) through. The deflection plates step through thirty logarithmically spaced voltages, allowing ions to pass through with energies ranging between $6.2 - 223.1$ keV/e. This curved deflection system not only selects the E/Q of incoming particles but also helps to prevent any stray light from making it into the instrument.

Once through the deflection system, the particle impacts a very thin carbon foil ($\sim 2\,\mu g/cm^2$), at the beginning of the TOF telescope. The carbon foil is thin enough for an energetic ion to pass through, but it will knock off one or more secondary electrons as it does. This secondary electron is then detected by the front secondary electron detector assembly (SEDA), which causes a start signal for the TOF calculation. The front SEDA consists of a microchannel plate (MCP), which generates the start signal, and two discrete anodes, which help to provide the elevation angle information of the ion. The ion does lose some energy as it passes through the carbon foil which can be estimated, as described later. Once inside the TOF telescope, the ion travels a distance of 10.0 cm until it strikes a solid state detector (SSD). Here, two things happen. First, if the incident ion has an energy that is greater than the measurement threshold of the SSD, ~ 30 keV, then the energy of the ion can be measured. And second, on impact with the SSD, the ion knocks another secondary electron off of the detector. This electron is then detected by the rear SEDA, causing a stop signal for the TOF analysis. With both the start and stop signals, the duration the ion spent in the TOF telescope can be determined. Since the length of the telescope is known,

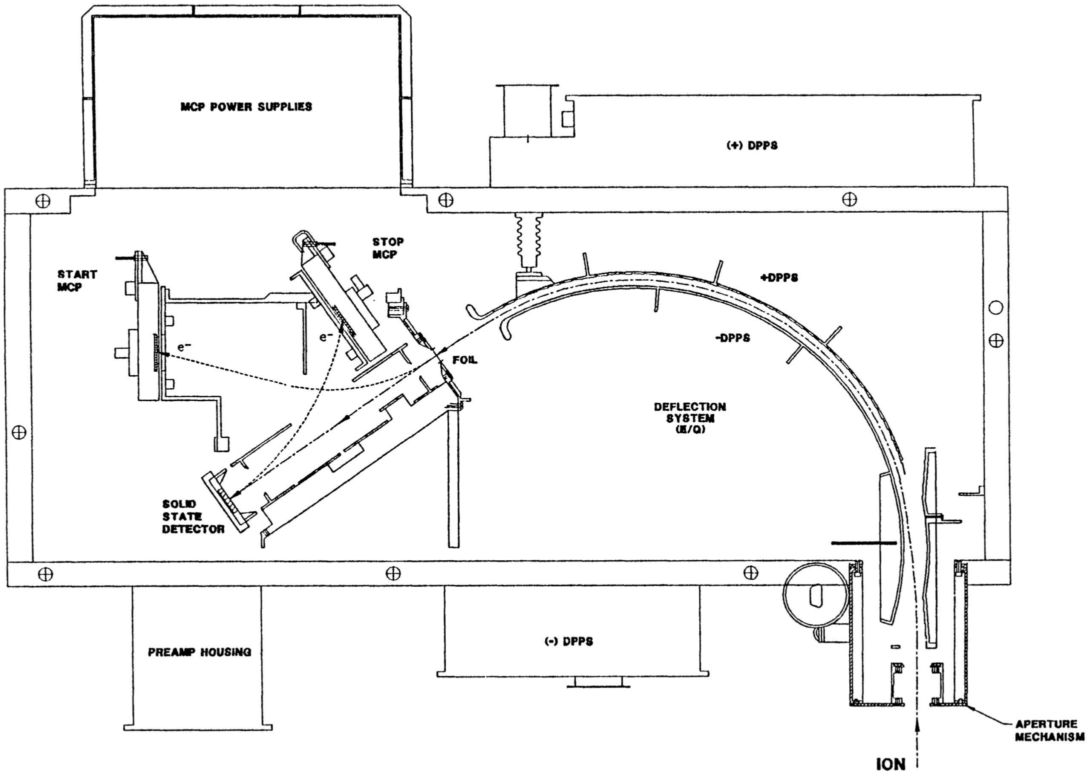

Figure 5.4: Simplified cross-section of the STICS instrument. It shows the path of a particle as it enters the detector and travels through the system. Published in (*Gloeckler et al.*, 1995).

the velocity of the particle can also then be obtained (*Gloeckler et al.*, 1995; *Chotoo*, 1998). Figure 5.4 shows these components of the STICS instrument which an ion encounters during its path through the system.

The entrance aperture of STICS is oriented such that it is perpendicular to the spin axis of Wind. This allows observations over all azimuthal angles. The instrument itself consists of three TOF telescopes. Oriented such that observations spanning from 79.5° above the ecliptic plane to $-79.5°$ below the ecliptic plane can be made, split into three sectors, one for each telescope 53° in span. These three sectors are shown in the top portion of figure 5.5. Two 53° telescopes look above and below the ecliptic plane, while one 53° telescope looks directly along the plane. Since the instrument look direction is perpendicular to the spin axis, STICS can observe all azimuthal directions

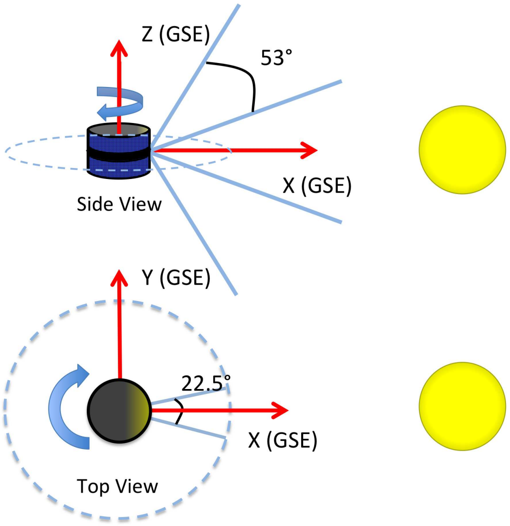

Figure 5.5: Field-of-View (FOV) of STICS. The top picture shows the off-ecliptic FOV, in the GSE X-Z plane. The bottom picture shows the azimuthal acceptance angle for STICS for 1 observational sector, in the GSE X-Y plane. Sectors not to scale.

as the spacecraft spins. The angular acceptance angle of the instrument is 4.8° and continually observes particles as the spacecraft spins, observing all azimuthal angles. The azimuthal observations are divided into sixteen equally sized bins, each having a span of 22.5°. These are numbered from 0-15, with sector 0 denoting when the deflection system's voltage changes. The bottom portion of figure 5.5 demonstrates the azimuthal span of the STICS instrument. These individual observation bins combine to give nearly three-dimensional compositional analysis of the suprathermal plasma (*Chotoo*, 1998).

STICS is optimized to make high cadence observations of the suprathermal plasma population. As previously mentioned, the Wind spacecraft rotates at speed of 20 rpm, equivalent to 3 seconds per spin. Each deflection voltage step is held for 2 spins in order to make observations in all sixteen azimuthal sectors at each voltage. To step through all of the voltage steps it takes 60 spins, or 3 minutes. Therefore, STICS is able to make a single E/Q and direction observation with a time resolution of 3 seconds, and can sample the full distribution of energies, in all directions, every 3 minutes.

Properties of each observed particle, such as mass, mass-per-charge (M/Q), and energy are calculated onboard the spacecraft. The particle data is then finally transmitted to Earth in two forms. In the first form, the data is binned onboard into previously set bins based on ion mass and M/Q. The particles are accumulated in each bin over the amount of time it takes for the instrument to cycle through all voltage steps, creating matrix rates for each ionic species. For the He^{2+} matrix rate, the full directional information is retained. While for the H^+ rate, only half of the directional information is preserved, as each returned rate is the combination of two observational sectors. Finally, for twenty other ionic species, which represent a number of heavy ions (such as C^{4+}, O^{6+}, and Fe^{10+}), the returned matrix rate is accumulated over all observation directions, retaining no directional information. In addition to the matrix rates, STICS also creates a number of Pulse Height Analyzed (PHA) words for a subset of the particles observed by the instrument. Each PHA word contains the measured time-of-flight, energy, and observation direction information. This allows the element, ionic state, and velocity of the particle to be determined. With this information, the phase space distribution for each ionic species can be calculated.

5.3 From PHAs to the Phase Space Distribution Function

In order to maximize the scientific uses of the suprathermal plasma observations from STICS, we often need more information than the counting rate of particles alone. PHA words make it possible to produce the phase space distributions for each ionic species. A phase space distribution describes the density of particles, from a given parcel of plasma, as a function of velocity of the particles. In other words, we can see how the particles in a plasma are distributed over a range of energy and space. As with any distribution, we can then take moments of this distribution in order to determine the bulk parameters of the plasma. For instance, the zeroth moment determines the density of the plasma, the first moment determines the bulk velocity, and the second moment determines the thermal velocity. The process to convert an instrument's counting rates to a phase space distribution is well understood (*von Steiger et al.*, 2000). For the STICS instrument, we follow a process similar to that presented in *Chotoo* (1998).

5.3.1 Calculating Physical Properties from the PHA Word

To begin, we first need to identify the ionic species that created each PHA word. As previously mentioned, each PHA consists of the time-of-flight, energy, and directional information. This information can be used to determine the identity of the ion. However, since this information is encoded into digital channel numbers to preserve memory space, we first need to convert these to physical units. *Chotoo* (1998) describes this process, using the following equations.

To calculate the time-of-flight, in ns, of the the particle, τ, from the digital channel number, T_{CH}, we use the following equation.

$$\tau = (T_{\mathrm{ch}} - 44)/2.372530695 \tag{5.1}$$

To determine the measured energy, in keV, from the SSD, E_{meas}, from the compressed energy channel, E_{c}, we use the process described in *Chotoo* (1998). Due to the memory constraints on the size of each PHA word, only 1024 different energy channels are able to be used. However, in order to represent the full span of energies for the many different ionic species of the solar plasma, the telemetered channel number is compressed from the actual energy channel number E_{d}. This allows a greater span of energy bins. Therefore, we need to first decompress the channel.

$$E_{\mathrm{d}} = E_{\mathrm{c}} \text{ for } E_{\mathrm{c}} < 256 \tag{5.2}$$

$$E_{\mathrm{d}} = 2E_{\mathrm{c}} - 256 \text{ for } 256 \leq E_{\mathrm{c}} \leq 384 \tag{5.3}$$

$$E_{\mathrm{d}} = 4E_{\mathrm{c}} - 1024 \text{ for } 384 \leq E_{\mathrm{c}} < 1024 \tag{5.4}$$

Then the measured energy can be obtained from the following relation.

$$E_{\mathrm{meas}} = (E_{\mathrm{d}} + 6)/0.37654782 \tag{5.5}$$

We can determine the E/Q, in keV/e, of the ion based on the the deflection voltage step number, DVS, that the instrument is set to when the particle passes through the deflection system. This step number is contained within the PHA word. To determine the E/Q, from the step number, DVS we can use the following equation.

$$E/Q = 6.190722 * (1.1225857)^{DVS} \tag{5.6}$$

As previously discussed, the STICS instruments steps through a total of thirty separate voltages which are applied across the deflection plates, allowing ions with energies ranging from $6.2 - 223.1$ keV/e. In order to fully sample all sixteen azimuthal directions at each voltage step, the deflection voltage is currently held constant for two spins. This allows for an ample observation time while in the heliosphere. Therefore, it takes a total of sixty spins to step through all the defined voltage steps once. One full sequence of all the voltage steps is defined as a cycle. The order in which the voltage is applied can be defined at any time. Currently, STICS uses a triangular stepping sequence. In other words, the deflection plates begin at the lowest possible voltage and steadily increase to the maximum voltage over the next thirty spins, holding each step constant for two spins. After the plates reach the maximum voltage of the

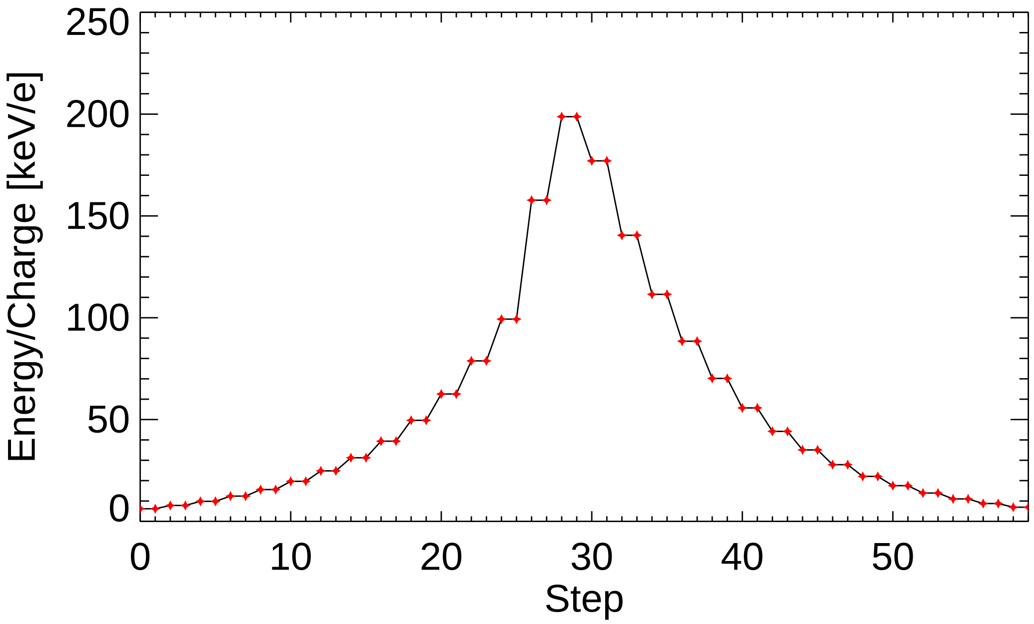

Figure 5.6: Typical E/Q stepping sequence for the STICS deflection system.

stepping table, STICS steadily steps back down to its minimum voltage over the next thirty spins. The voltages applied during the first thirty steps are different from those applied during the last thirty steps, allowing different ion E/Q through on either side of the voltage maximum. An illustration of the triangular stepping sequence is shown in figure 5.6.

5.3.2 Ion Identification

Once the TOF, E/Q, and energy of a PHA are determined, identification of the ionic species is possible. This can be accomplished in a few different ways. First, we will discuss using the time-of-flight and the energy-per-charge of the particles. Figure 5.7 shows the distribution of PHAs, accumulated over the entire year of 2004, versus the time-of-flight and the E/Q of the measured ion. It can be seen that there are a number of distinct tracks that are enhanced over the background. These tracks correspond to individual ion species. The three bright tracks on the left side of the

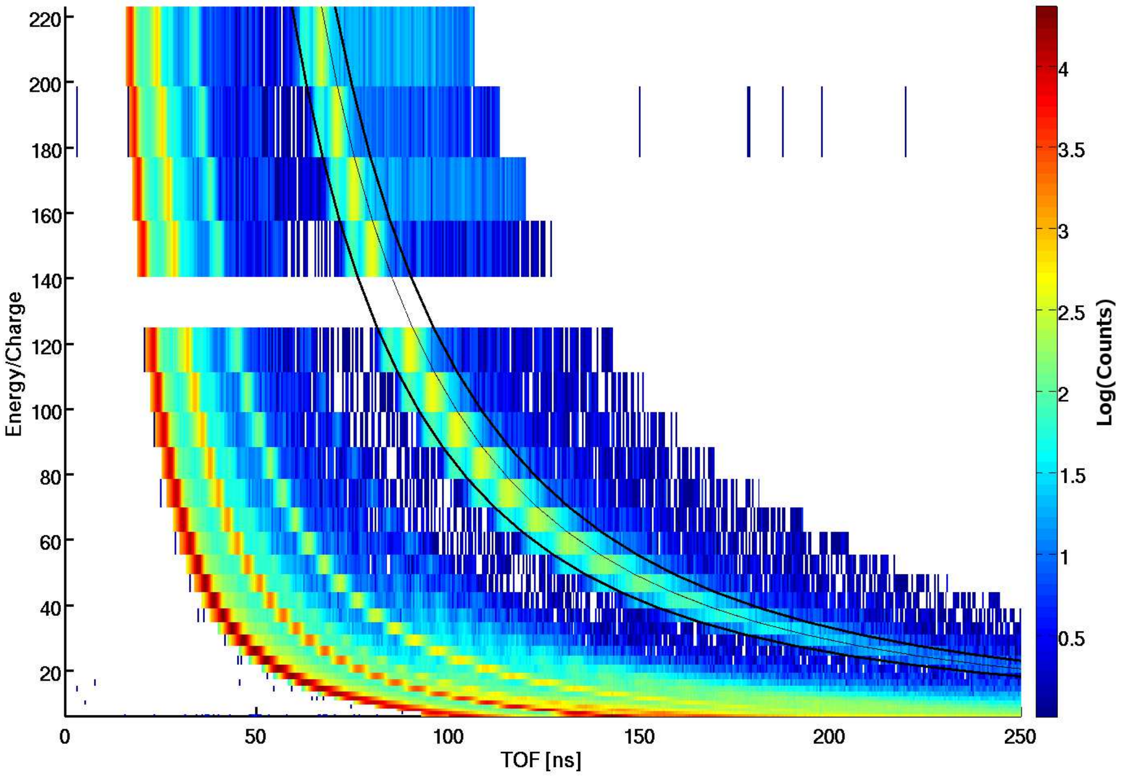

Figure 5.7: Distribution of the particles over the time-of-flight and energy-per-charge measured by STICS. The data shown is an accumulation of PHAs over the entire year of 2004. The thin black line is the predicted location of O^+, while the two thick black lines indicates the bin used for O^+ identification.

data correspond to H^+, He^{2+} and He^+. In early 2004, Wind was finishing its deep magnetotail orbit, spending a portion of time sampling the Earth's magnetosphere, resulting in a large O^+ track appearing in the data, to the right of the previously mentioned three tracks. We will use this track as an example of identification using the TOF and E/Q distribution.

To ensure that the TOF track is composed of $O+$ ions, we first predict the time-of-flight for an $O+$ ion at all the energy-per-charge steps of STICS. We do this by calculating the velocity an ion would have after it passes through the carbon foil, V_{ion} in km/s, entering the STICS TOF telescope during energy-per-charge step, E/Q in keV/e, using the following relation.

$$V_{\text{ion}} = 439.36 * \sqrt{((E/Q) * (Q/M) - (E_{\text{loss}}/M))} \qquad (5.7)$$

In the above equation, Q/M represents the ratio of the charge to mass of a specific ion. To improve the accuracy of the ion's predicting velocity in the TOF telescope, we must account for the energy lost by the ion when it passes through the carbon foil, E_{loss}. This can be estimated by using the Transport of Ions in Matter (TRIM) software (part of the Stopping and Range of Ions in Matter (SRIM) software package, *www.srim.org*). TRIM calculates the kinetic energy a particle loses when passing through some material from collisions with the atoms of the material. By performing a monte carlo simulation of atoms of a specific energy impacting a defined material one can estimate the average loss of energy for a particle passing through that material. Figure 5.8 shows one such calculation we performed for an oxygen atom with an energy of 78.81 keV impacting a layer of carbon 89 angstroms thick, similar to the carbon foil in STICS. The energy loss has a gaussian distribution, due to the randomness of the scattering of the particle in the material. Therefore, we can determine the energy loss for a particular energy-per-charge step by calculating the mean of the distribution. This calculation is carried out for all E/Q steps of the instrument to characterize the energy loss for all possible ion observations.

Once the velocity of the ion has been determined, it is trivial to determine the ion's time-of-flight, τ in ns, through the TOF system. Since the distance the ion travels in the TOF telescope, $d = 10.0$ cm, is known, τ is simply the ratio of distance to velocity. The following equation shows this relation, where the leading factor of 10000 performs the necessary unit conversion.

$$\tau_{\text{ion}} = 10000 * \frac{d}{v_{\text{ion}}} \qquad (5.8)$$

Combining Equation 5.7 and Equation 5.8 results in the relation for the predicted

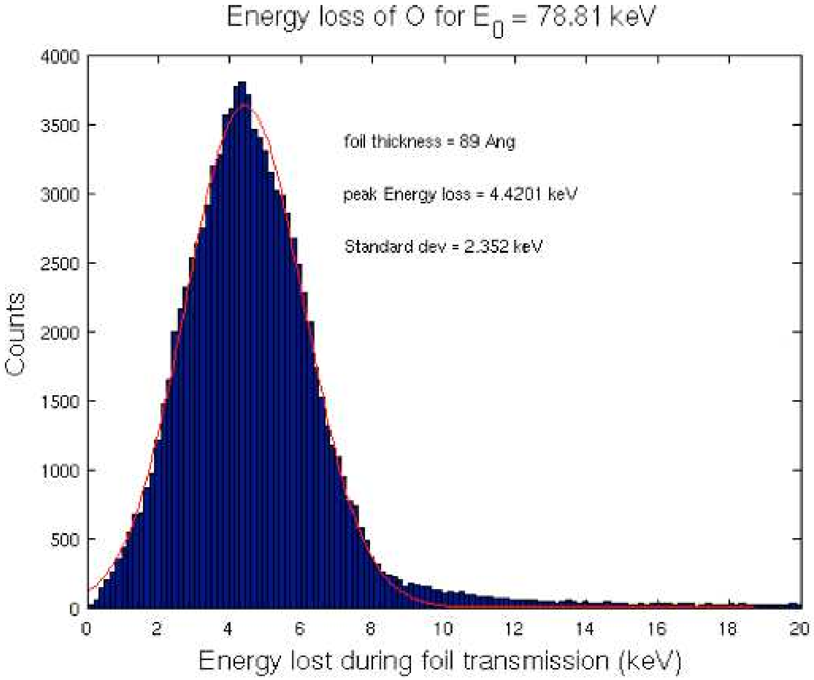

Figure 5.8: Results of the TRIM calculation for a number of oxygen atoms, with an energy of 78.81 keV, impacting a carbon foil of thickness of 89 angstroms, the same thickness as the carbon foil on STICS. The red curve is a gaussian curve fit to the histogram, with the mean energy loss and standard deviation displayed.

time-of-flight of an ion determined by its E/Q, as measured by STICS.

$$\tau = \left[\frac{439.36}{10,000 * d} * \sqrt{((E/Q) * (Q/M) - (E_{\text{loss}}/M))}\right]^{-1} \tag{5.9}$$

In Figure 5.7, the predicted time-of-flight, using Equation 5.9, of an O^+ ion is plotted as the thin black line. It can be seen that this predicted track lines up with the bright track in the data. For each voltage step, a range of potential E/Q of the incident ions are capable of passing through the deflection system. This is referred to as the energy passband, $\Delta E/Q$. Calibration data has shown that the average passband is $\frac{\Delta E/Q}{E/Q} = 1.9\%$ (*Chotoo*, 1998). Considering this spread in E/Q we can create a TOF band, centered on the predicted track, for a given ion. This band is shown in Figure 5.7, by the two thick black lines. Any PHA landing in this band we then classify as an O^+ ion. As can be seen, the entire bright track in the data lies within these bounds. For any ion which we can create a track for, we can then classify using the time-of-flight and energy-per-charge information of the PHA.

The TOF-E/Q method works well for ions that have distinct mass-per-charge ratios, but for many of the heavy ions, these tracks would overlap each other, making it harder to classify the ions. Instead we can use the mass and mass-per-charge calculated from each PHA word. From the E/Q, energy, and time-of-flight of the PHA, we can calculate the mass and M/Q. This method is similar to the one used onboard the spacecraft to create the matrix rates previously discussed. *Chotoo* (1998) provides the equations used for these conversions.

$$\begin{aligned} M &= 2 * (\tau/d)^2 * (E_{\text{meas}}/\gamma) \qquad (5.10) \\ M/Q &= 2 * (\tau/d)^2 * (E/Q) \qquad (5.11) \end{aligned}$$

We then create a distribution of PHAs, accumulated over a length of time, in

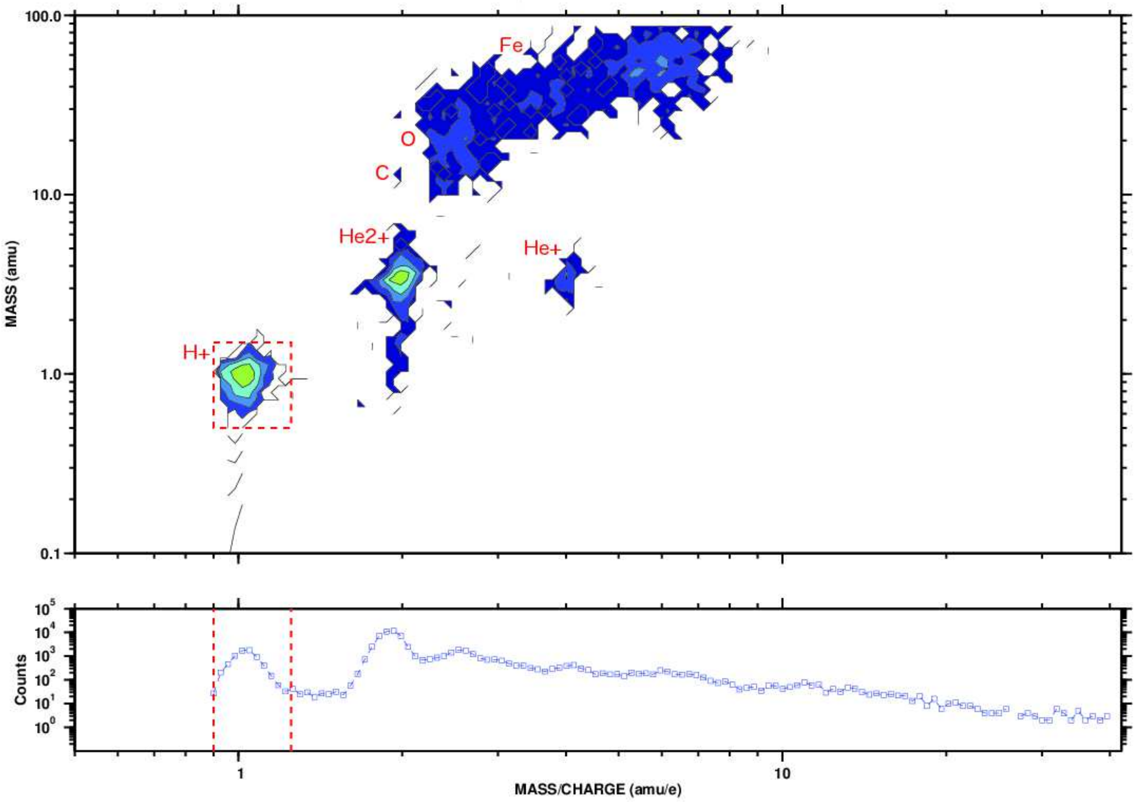

Figure 5.9: The top panel shows a distribution of PHA words from May 30, 1995 versus M/Q and mass. The bottom panel shows the distribution of counts integrated over all masses as a function of M/Q. The Mass-M/Q box boundaries for $H+$ ions is shown, as well as the general location of the $He2+$ ions, $He+$ ions, C group, O group, and Fe group.

Mass-M/Q space. Figure 5.9 shows one such distribution, accumulated on May 30, 1995, similar to the Figure in *Chotoo* (1998). Compared to Figure 5.7, individual ions appears as distributions spread around a single point, determined by the ion's mass and M/Q, instead of tracks. The top panel of Figure 5.9 displays the distribution of particles that created PHA words, while the bottom panel shows the number of particles per M/Q. The bottom panel is created by integrating over all masses for each M/Q bin in the distribution.

Based on the mass and M/Q of each species, the identification of the ionic species is possible for each particle. To do this, we create boxes in Mass-M/Q space, centered

Ionic Species	**Mass Low (amu)**	**Mass High (amu)**	**M/Q Low (amu/e)**	**M/Q High (amu/e)**
H^+	0.0	2.13	0.90	1.26
He^+	2.79	6.30	3.55	4.67
He^{2+}	2.79	6.30	1.61	2.32
C^{4+}	9.04	12.99	2.87	3.24
C^{5+}	9.04	12.99	2.25	2.54
C^{6+}	9.04	12.99	1.87	2.18
O^+	4.80	79.30	14.89	20.20
O^{6+}	10.83	20.41	2.54	2.87
O^{7+}	14.21	20.41	2.11	2.46
Fe^{8+}	38.45	79.28	6.53	7.38
Fe^{9+}	38.45	79.28	5.78	6.53
Fe^{10+}	38.45	79.28	5.28	5.78
Fe^{11+}	38.45	79.28	4.82	5.28
Fe^{12+}	38.45	79.28	4.40	4.82
Fe^{14+}	38.45	79.28	3.77	4.14
Fe^{16+}	38.45	79.28	3.34	3.55

Table 5.1: Mass and M/Q boundaries for ionic species measured by Wind/STICS. Published in *Chotoo* (1998).

on the mass and M/Q for each species. These boxes account for any spread of the ions in the space due to energy loss of the ion in the system and the energy passband of the instrument allowing ions with energies ranging about the E/Q step to enter the system. In Figure 5.9 we show one such box, in the top panel, for selecting protons. Any particle that falls within this box is classified as a proton. Using the same mass and M/Q box definitions which STICS uses onboard to create the matrix rates for heavy ions, as described earlier, we can then classify a number of the ions. In Figure 5.9 we have indicated the distribution of both the $He+$ and $He2+$ ion as well as the general location of the C, O, and Fe groups of ions.

Table 5.1 shows the boundaries of these boxes in both dimensions for the heavy ions which we can currently identify, provided by *Chotoo* (1998). If an incoming particle does not have enough energy to overcome the SSD energy threshold, then its mass can not be determined. These events are called double coincidence events, as only a start and stop signal can be made, as opposed to a triple coincidence event, when both timing signals and an energy measurement can be made. The mass of a double coincidence particle can not be determined, and will then have a mass of zero amu. These events can still be included in analysis for some ions, by only considering the M/Q ranges from Table 5.1. The bottom panel of Figure 5.9 illustrates the M/Q range for H^+. Inside these bounds we can see a clear peak, corresponding the large contribution of proton measurements. Additionally, we can see a significant peak near $M/Q \sim 2$, corresponding to the He^{2+} observations. Further identification in this manner can be difficult however, as many heavy ions have a very similar M/Q. For example, the M/Q of O^{7+} is $\sim$ 2.4 while the M/Q of C^{5+} is $\sim$ 2.3. The distribution for an ion is spread out in mass-M/Q space, making it difficult to discriminate between two ions in the region where they may overlap.

5.3.3 Calculating Differential Flux

In order to minimize the observational error of a specific ion, we accumulate the observations over a duration of time. With the number of ions observed over this time period known, we can then calculate the phase space distribution of the sampled plasma, following the methodology of *Chotoo* (1998). The first step, is to convert the counts into differential flux. The differential flux describes the flux of particles, per unit of energy, incident on the instrument's detectors. The conversion from the number of counts of a particular ion identified by STICS to flux, is straightforward. *Chotoo* (1998) gives the relation as

$$\frac{dJ}{dE} = \frac{counts}{g\,\Delta E/Q\,\eta_1\,\eta_2\,\Delta t}\frac{DC\,BR_{\mathrm{norm}}}{Box_{\mathrm{eff}}} \tag{5.12}$$

The differential flux has units of $[cm^2\,s\,sr\,keV/amu]^{-1}$ and is denoted as $\frac{dJ}{dE}$ in the above equation, while *counts* is the number of ions that we have identified by one of the identification previously discussed for a particular E/Q step. The accumulation time of the observation is denoted by Δt. The remaining terms in the above equation

Telescope	**Parallel Beam**	**Isotropic**
	Geometric Factor (cm^2)	**Geometric Factor** ($cm^2\, sr$)
1	0.72 ± 0.18	0.031 ± 0.002
2	0.68 ± 0.18	0.029 ± 0.002
3	0.74 ± 0.18	0.029 ± 0.002

Table 5.2: Geometric factors for STICS determined from calibration. As published in *Chotoo* (1998).

describe the efficiency of the STICS instrument's ability to observe an ion from the incident flux and will be described in further detail.

The geometric factor of the instrument is represented by g in Equation 5.12. As not every particle is able to make it into the instrument due to scattering in the electrostatic analyzer and the particle's angle of entry, the geometric factor represents the relationship between the counting rate of particles in the instrument and the actual incident flux from the heliosphere on the aperture.. This factor represents the effective aperture size that particles can enter the system through. The values for the geometric factors of STICS are published in *Chotoo* (1998) and shown in Table 5.2. These values were determined from pre-flight calibration and in-flight cross calibration (*Chotoo*, 1998). If the radiation is from a beam of particles entering the instrument perpendicular to the aperture, then the geometric factor is only dependent on the area of the aperture. If, however, the particles are isotropically distributed and impacting the aperture at a number of different angles, then the geometric factor is dependent on the full solid angle acceptance range of the aperture (*Chotoo*, 1998). This results in smaller geometric factors, seen in Table 5.2, for isotropic particle distributions compared to that from the parallel beam case. The parallel beam approximation is appropriate for particle populations originating from a single source, such as the solar wind, while the isotropic factor is used for particle populations which are evenly distributed in velocity space, such as the suprathermal particles or pick-up ion distribution.

As previously discussed, the deflection system of STICS is designed to allow only particles with a particular E/Q to enter the instrument. However, the E/Q of particles that do make it through the deflection system spread over a small range about this value. This is called the energy passband, $\Delta E/Q$, as described in the previous section. From calibration data, this has been found to have a value of $\frac{\Delta E/Q}{E/Q} \sim 1.9\%$ (*Chotoo*, 1998).

Not all the particles that make it through the deflection system become measured by the TOF telescope. The likelihood of a particle of a particle in the TOF telescope to pass through the carbon foil and then trigger a measurement at the SSD detector is referred to as the efficiency and is denoted by the η_{X} terms in Equation 5.12. The efficiency of a particle passing through the carbon foil and triggering a start signal is referred to as the start efficiency, η_1. The efficiency denoted by η_2 can refer to two different situations. If we are considering triple coincidence particles, then η_2 refers to the triple efficiency. The triple efficiency describes the ability for a particle to produce both the stop signal and the SSD energy measurement. If however, we also choose to consider double coincidence events in the analysis, then η_2 refers to the stop efficiency. The stop efficiency illustrates the ability of a particle, that has triggered a start signal, to trigger a stop signal. These efficiencies have been determined during the calibration of the instrument, and are provided by *Chotoo* (1998). Figure 5.10 shows a sample efficiency curve for protons. The top panel shows the start efficiency, η_1, and the middle panel shows the triple efficiency, η_2. Since, the calculation for differential flux uses the product of these efficiencies, we show this in the bottom panel. This represents the overall efficiency of a particle that passes through the deflection system to be measured by the TOF system.

The value DC, in Equation 5.12, is the deadtime correction for the instrument. Each spin of the Wind spacecraft takes 3 seconds, however the instrument does not make observations for this entire time. This is due to a number of reasons as the instrument requires time for flight software to classify ions which it has previously

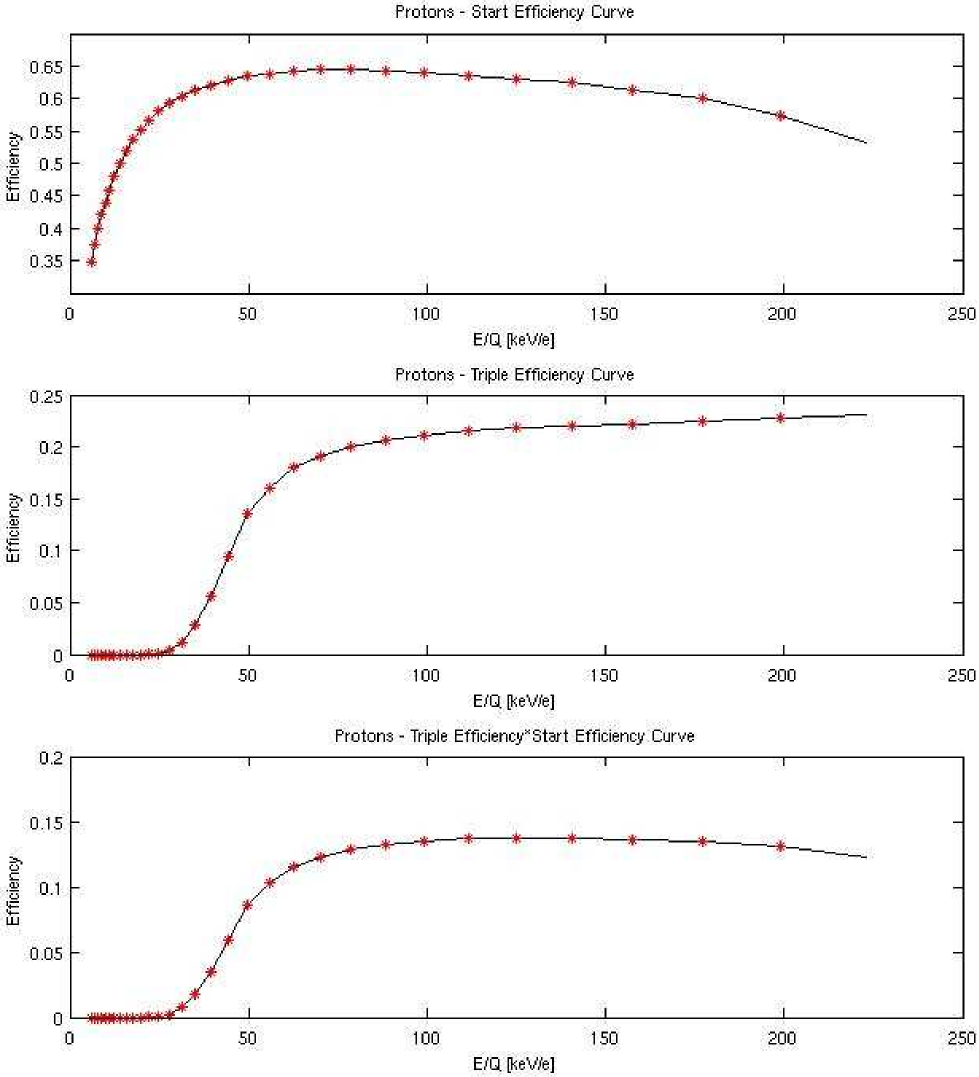

Figure 5.10: Efficiency curves for protons. The top panel shows the efficiency of an incoming particle to trigger a start signal. The middle curve shows the efficiency of a particle that has triggered a start signal also triggering a stop signal and a measured energy from the SSD. The bottom curve shows the combination of these first two curves. Curves are determined from calibration data, and published in *Chotoo* (1998). The red asterisks represent the E/Q steps from the deflection system.

Sector	**Deadtime Correction Factor**
0	2.143
1-15	1.068
Full Spin	1.103

Table 5.3: The deadtime correction factors for STICS. As published in *Chotoo* (1998).

observed, read counters, and perform other housekeeping chores. These things happen between every observation sector. There is a longer deadtime period for the first observation sector of each spin. The voltage in the deflection system is changed at the beginning of the spin and more time is required for the stepping voltages to settle. As there are sixteen observation sectors, each one lasting 187.5 ms. The instrument has a deadtime of 12 ms between each sector, and an additional 100 ms of deadtime for sector 0 (*Chotoo*, 1998). Sector 0 will always have a deadtime of 100 ms, as a convince for the data processing unit, regardless of whether the voltage has been changed. The deadtime correction is simply a factor to account for this lost observation time, and is determined by the ratio of total available time to actual observation time. Table 5.3 shows the deadtime correction factors for sector 0, the first observation sector, and the other sectors. Additionally, the deadtime correction factor for an entire spin is shown. This is used when we use considering one of the counting rates that does not have directional information. These factors were published in *Chotoo* (1998).

The BR_{norm} term represents the basic rate normalization applied to the observed counts. Since STICS cannot return a PHA word for every measured particle, three basic rates (BR), for eight azimuthal directions, are returned accounting for particles falling within 3 separate mass-M/Q regions. The PHAs are then created for a portion of particles in each of these bins, distributed based on the priority assigned to each mass-M/Q region. One bin encompasses H^+, He^+, and He^{2+}, which composes a majority of the observed heliospheric plasma.

To ensure that all the telemetered PHA words are not created from protons, this region is given the lowest priority. In other words, the smallest number of PHAs are

Ion	**Box Efficiency**
H^+	0.90 for $DVS < 15$
	0.99 for $DVS \geq 15$
He^+	0.98
He^{2+}	0.98

Table 5.4: The box efficiency for the M-M/Q boxes of H^+, He^+, and He^{2+}. The efficiencies for H^+ are dependent on the deflection voltage step number, DVS. This were published in *Chotoo* (1998).

created per number of measured particles.

Multiply charged heavy ions constitute the next highest priority, and singly charged pick-up heavy ions have the highest priority. The basic rate then describes the total amount of particles that were observed by STICS. Thus, the basic rate normalization is simply the ratio $BR_{\mathrm{norm_i}} = BR_{\mathrm{i}}/PHA_{\mathrm{i}}$ for each azimuthal sector, where i represents the basic rate region and PHA_{i} refers to the number of PHA words created from particles falling in that region (*Chotoo*, 1998).

The final term in Equation 5.12 represents the efficiency of the mass-M/Q box to include all observed ions of the particular box, Box_{eff}. The ion distribution can spread beyond the bounds of the mass-M/Q box that is defined. The box efficiency is meant to correct for the number ions that are observed by STICS but are not properly identified due to the limitations of the mass-M/Q box used. *Chotoo* (1998) has characterized this value for the H^+, He^+, and He^{2+} boxes, while further ion box efficiencies have yet to be characterized. As seen in *Chotoo* (1998) and table 5.4, this correction is very small and should not alter the resulting differential flux much. For the ions not yet characterized, we use an efficiency of 1.0. Table 5.4 shows that there are two separate efficiencies for $H+$. As *Chotoo* (1998) describes, this is due to a larger amount of energy being lost in the carbon foil for the less energetic protons. Protons, due to their lighter mass and momentum, suffer from a greater energy loss in the carbon foil when the protons are slower. This causes the distribution to spread more, resulting in more protons falling outside of the classification box.

5.3.4 From Differential Flux to a Phase Space Distribution

Finally, we can obtain a phase distribution for a given ionic species, by calculating the phase space density from the differential flux. The phase space density, f in units of s^3/km^6, is the density of particles occurring in a volume of velocity space. This can be written in the same manner as *Chotoo* (1998).

$$f = \frac{dN}{d^3r\,d^3v} \tag{5.13}$$

The density of the particles is defined as the number of particles, dN, present in a volume of space, d^3r. The d^3v represents the volume of velocity space that the particles inhabit. Velocity space is another way of describing the energy range of a particular population of particles. To obtain the density of particles passing through the instrument, we relate it to the differential flux observed by STICS, using the following relation from *Chotoo* (1998).

$$dN = \frac{dJ}{dE}\,dA\,dE\,d\Omega\,dt \tag{5.14}$$

In the above equation, dJ/dE is the differential flux measured by STICS. The other terms describe how the observation was obtained. The dA term represents the unit area which particles are flowing through, dE represents the range of energies of the incident particles, $d\Omega$ is the solid angle acceptance cone of the aperture, and dt is the accumulation time of the measurement. Combining these two equations, we can get to a relation between differential flux and phase space distribution, as derived in *Chotoo* (1998).

$$\begin{aligned} dN &= f\,d^3r\,d^3v & (5.15) \\ \frac{dJ}{dE}\,dA\,dE\,d\Omega &= f\,d^3r\,d^3v & (5.16) \end{aligned}$$

We can simplify this relation further. First, we transform the differential velocity space into spherical coordinates, by $d^3v = v^2\, dv\, d\Omega$. Next, since $dr = v\, dt$, we can re-write the differential space term as, $d^3r = v\, dt\, dA$. Substituting these two relations into the above equation gives the following equation.

$$\frac{dJ}{dE}\, dA\, dE\, d\Omega = f\, v^3\, dv\, d\Omega\, dA\, dt \tag{5.17}$$

Canceling like terms from this equations, yields

$$\frac{dJ}{dE}\, dE = f\, v^3\, dv \tag{5.18}$$

Since, the energy appearing in the above equation is simply the kinetic energy of the particle, we can then write the energy as $E = 0.5\, m\, v^2$ which makes the differential energy, $dE = m\, v\, dv$. Substituting these relations into the above equations, yields our final equation which we can use to obtain the phase space density for a given ionic species from the observed differential flux.

$$\begin{aligned}
\frac{dJ}{dE}\, m\, v\, dv &= f\, v^3\, dv && (5.19)\\
\frac{dJ}{dE} &= \frac{v^2}{m}\, f && (5.20)\\
\text{Since, } v^2 &= \frac{2\,E}{m} && (5.21)\\
\frac{dJ}{dE} &= \frac{2E}{m^2}\, f && (5.22)\\
\Longrightarrow\ f &= \frac{m^2}{2E}\, \frac{dJ}{dE} && (5.23)
\end{aligned}$$

However, as previously stated, the units of differential flux are $[cm^2\, s\, sr\, keV/amu]^{-1}$ while the phase space distribution is commonly given in units of s^3/km^6. To perform the unit conversion, we multiply the right hand side of the above equation by 1.076 (*Chotoo*, 1998). This yields our final relation for the phase space density of an ionic species, as a function of particle energy.

$$f = 1.076 \, \frac{m^2}{2E} \, \frac{dJ}{dE} \tag{5.24}$$

We can then create the phase space distribution of a ion from this relation. The measurement error for the phase space density can be estimated from the Poisson counting error from the instrument, or $\sigma_{\mathrm{counts}} = \sqrt{counts}$. We can then propagate the error through the above equations to determine the error of the phase space density, σ_{f}. This is shown in the following equations.

$$\begin{aligned} \sigma_{\mathrm{counts}} &= \sqrt{counts} && (5.25) \\ \sigma_{\frac{\mathrm{dJ}}{\mathrm{dE}}} &= \frac{\sigma_{\mathrm{counts}}}{g \, \Delta E/Q \, \eta_1 \, \eta_2 \, \Delta t} \frac{DC \, BR_{\mathrm{norm}}}{Box_{\mathrm{eff}}} && (5.26) \\ \sigma_{\mathrm{f}} &= 1.076 \, \frac{m^2}{2E} \, \sigma_{\frac{\mathrm{dJ}}{\mathrm{dE}}} && (5.27) \end{aligned}$$

To calculate full phase space distribution function, the data needs to be accumulated over a set period of time. Because of Wind's spin configuration, STICS observes particles coming from all azimuthal directions. In order to calculate the 3-dimensional phase space density, the distribution function is then accumulated and calculated individually for each observation sector. If the distribution function is accumulated over all of the sectors, only a 1-dimensional distribution is able to be calculated. The 1-dimensional function can be determined with smaller measurement error when accumulated over shorter cadences than the 3-dimensional observation, but lacking any directional information. Figure 5.11 shows an example of a calculated phase space distribution function for alpha particles over a 14 hour observation period during DOY 150 of 2003 accumulated over all observation sector. The poisson counting errors are shown as the red vertical bars.

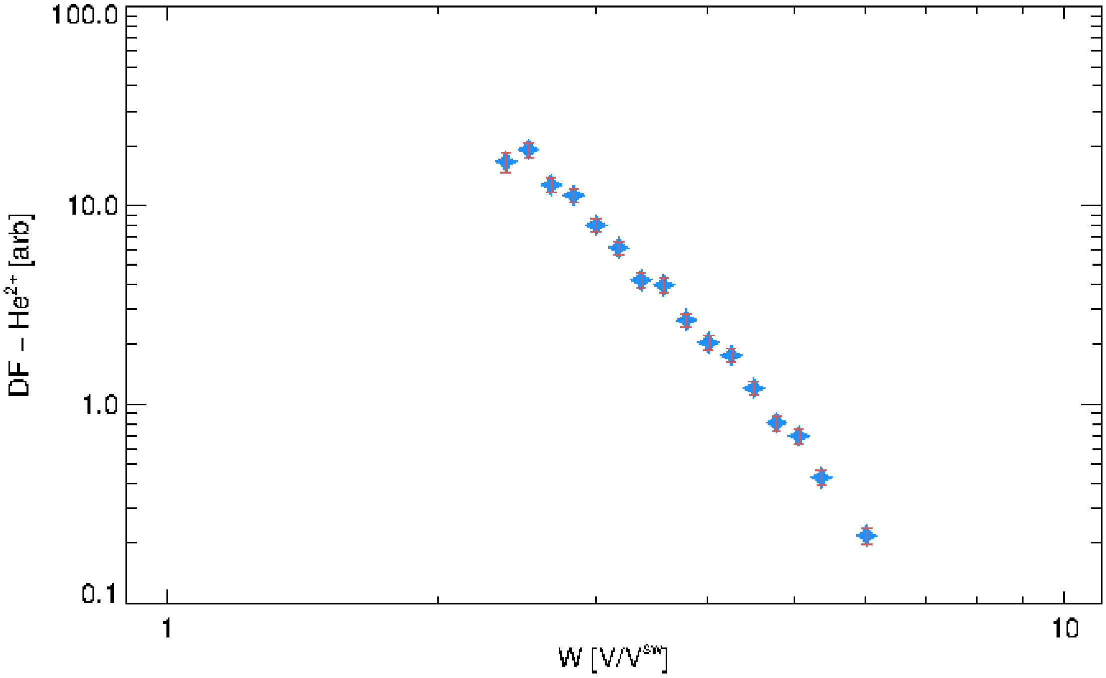

Figure 5.11: Phase space density, DF versus particle speed W, normalized by solar wind bulk speed, for alpha particles. Distribution was accumulated over DOY $150.083 - 150.67$ of 2003, and all sixteen view directions. The red error bars signifies the Poisson counting error.

5.4 Adaptive Cadence - Solution to Intermittent Periods of Observations

Normally, to create phase space distribution functions of solar wind plasma, as described in the previous sections, we accumulate the PHAs for a set amount of time, usually on the order of hours. This accumulation takes places in order to obtain enough counts to minimize the errors of the measurement. For the STICS data, even with two hour accumulations, the error bars can at times be very large because of the very small amount of incident particles. To accommodate these intermittent periods of measurements we have developed a method of an adaptive cadence.

The adaptive cadence method allows the accumulation time of the phase space distribution to vary, while processing long periods of data. To do this, we first set a desired counting error threshold and the number of energy bins of the distribution function to exceed this threshold. Typically we run the adaptive cadence method requiring 10 energy bins in order to ensure that at least $\sim 30\%$ of the total energy bins contain an observation satisfying the set error threshold. Initially, we choose an error threshold of $\sim 50\%$. This value was settled on as it requires that the distribution function is computed from more than only 1 or 2 counts.

After the number of energy bins and error threshold are determined, we begin to step through each measurement cycle and accumulate the number of STICS counts for a particular ion in each energy bin. At the end of each cycle, we compute the distribution function from the current accumulated counts and compute the measurement errors. Then we test each measurement error versus the desired error threshold which had been set. If the total number of energy bins achieving the desired error is greater than or equal to the number of bins we set, then the distribution function is outputted and accumulation for the next observation begins. However, if the number of energy bins satisfying the our desired measurement error is not large enough, the next measurement cycle is accumulated into the current distribution function measurement and the error threshold is tested once again. This procedure continues over the time period which we wish to process, allowing each calculated distribution function to be accumulated over a different amount of time, but all satisfying a set measurement error.

Figure 5.12 shows one such example of the adaptive cadence method. The top panel shows the accumulation time required to ensure that 10 energy bins had an error less than 50% for the three ions C^{4+}, C^{5+}, and C^{6+}. The next three panels shows the distribution function as it evolves in time for the three ions. The magenta dashed line shows the start time of an ICME as determined by *Richardson and Cane* (2010). As can be seen over the course of the three days, the accumulation time required to produce a distribution function varies from 1 day to 0.5 hours, for both C^{5+} and C^{6+}.

Using the adaptive cadence method we have been able to pinpoint a wide array of periods when the measured phase space distribution from STICS is able to be computed at very high-cadences. These often occur near transitions in the heliospheric environments, such as at co-rotation interaction region (CIRs), interplanetary (IP) shocks, and interplanetary coronal mass ejections (ICMEs). During these transition events the cadence time required to calculate phase space distributions can be on the order of ten's of minutes, compared to quieter periods when it can take up to ten's of days. High-cadence measurements during these time periods enable the investigation of their impact on the suprathermal particles. It is not well understood whether transition events like these have a significant impact on the suprathermal population, such as further heating of the particles. We also find that high-cadence measurements can be produced upstream of the Earth's bow shock and inside the magnetosphere. Observations such as these, allow the exploration of the leakage mechanism of plasma into and out of the magnetosphere, and any possible energization of the plasma occur-

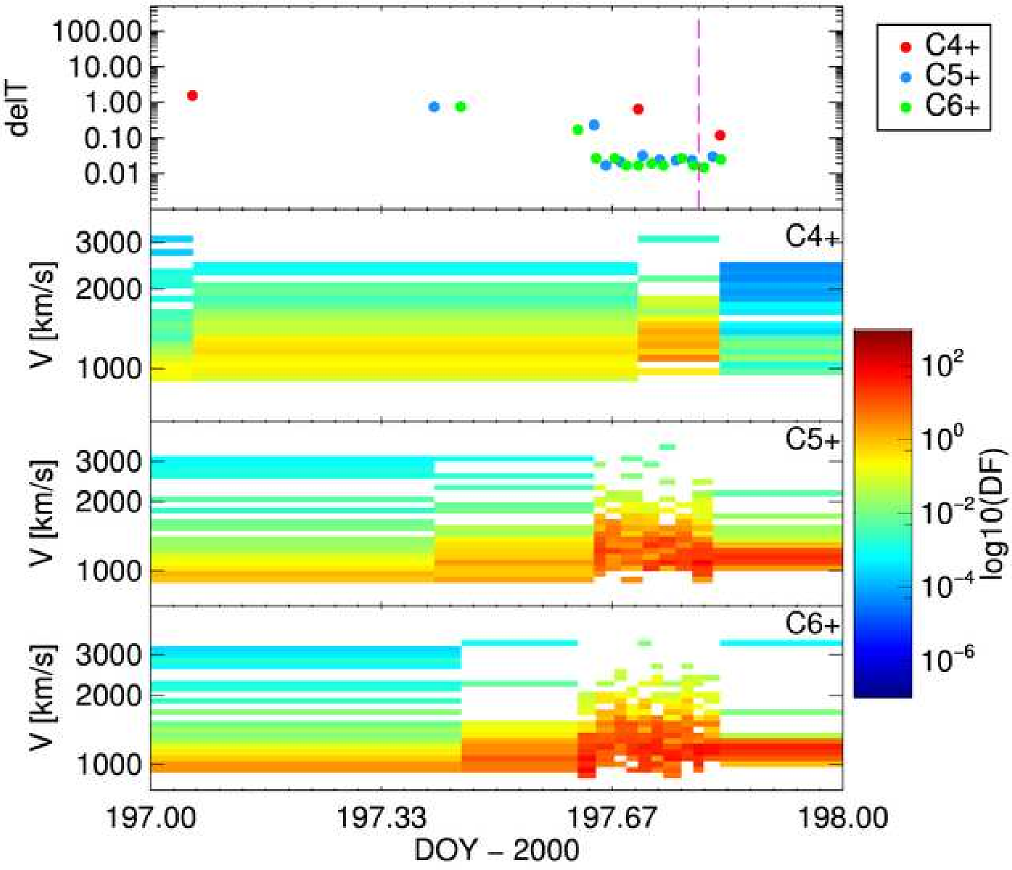

Figure 5.12: Spectrogram plot showing an example of the adaptive cadence ratio, for the carbon ions C^{4+}, C^{5+}, and C^{6+}. Top panel shows the accumulation time for each returned distribution function. The next three panels show the phase space distribution versus time. Particle velocity is along the y-axis. The magenta dotted line represents the beginning of an ICME, as determined from (*Richardson and Cane*, 2010).

ring at the bow shock. Using the ICME time periods determined from this method, we can explore the relationship between the suprathermal ionic composition and the bulk plasma, utilizing the unique compositional characteristics of ICMEs.

CHAPTER VI

Suprathermal Heavy Ion Observations during Interplanetary Coronal Mass Ejections

The text of this chapter is presented as a draft which will be submitted to the Astrophysics Journal.

Abstract

Suprathermal particles are an important seed population for a variety of energetic particles found throughout the heliosphere, but their origin is in debate. We present, for the first time, high-cadence observations of suprathermal heavy ions during interplanetary coronal mass ejections (ICME), from the Suprathermal Ion Composition Spectrometer (STICS) onboard the Wind spacecraft, and investigate their ionic composition and compare it to the bulk plasma composition, observed from the Solar Wind Ion Composition Spectrometer (SWICS) onboard the Advanced Composition Explorer (ACE). We find that the composition of the suprathermal plasma is related to the local bulk plasma and not to the bulk solar wind plasma upstream of the ICME. This implies that the suprathermal plasma is accelerated from the local bulk plasma and not the upstream solar wind plasma from the CME-driven shock.

6.1 Introduction

The suprathermal plasma population consists of ions that are more energetic than the ions of the thermal solar wind, ranging in energies from ~ 10 keV/nucleon - ~ 100 keV/nucleon. Figure 6.1, from*Mewaldt et al.* (2001), shows a three year accumulation of the oxygen fluence observed by the Advanced Composition Explorer (ACE) (*Stone et al.*, 1998). The suprathermal plasma is the population of ions lying between the solar wind thermal plasma and solar energetic particles in the higher energy regime. This regime may also contain another population, missing from figure 6.1, the contributions from pick-up ions, which will show up for singly charged ions but not for multiply charged heavy ions. These ions are evident in a distribution function for protons and singly ionized helium as an extended distribution of particles with a shoulder at $\sim 2\ v_{\text{sw}}$ (*Gloeckler et al.*, 1993). These ions will not contribute to the heavy ion population

The suprathermal plasma has been suggested to be an important seed population for energetic particles accelerated by co-rotating interaction regions (CIRs) (*Mason et al.*, 2012), and solar energetic particles (SEPs) (*Tylka et al.*, 2005). The origin of the suprathermal particles is still in question. Several mechanisms have shown promise for generating suprathermal particles in the heliosphere. Possible acceleration mechanisms such as thermal solar wind accelerated locally, or particles accelerated remotely, in the corona or at interplanetary shocks (*Laming et al.*, 2013).

One possible local source is the pump mechanism, introduced by *Fisk and Gloeckler* (2012a), acting on the bulk plasma. The pump mechanism is a fundamental acceleration process which is used to explain the ubiquitous observations of the common spectral shape observed in suprathermal population throughout the heliosphere (*Fisk and Gloeckler*, 2006; *Gloeckler et al.*, 2000). By employing a series of expansions and contractions in the local magnetic field, the local bulk plasma can become energized into suprathermal energies. Particles accelerated in such a manner would retain the compositional characteristics of the local plasma. Additionally, the pump mechanism has been invoked to attempt to explain the similar spectral observations of ACRs (*Fisk and Gloeckler*, 2009), and galactic cosmic rays (GCRs) (*Fisk and Gloeckler*, 2012b).

However another mechanism, diffusive shock acceleration, has long been thought of as a source of energetic particles (*Lee et al.*, 2012). Diffusive shock acceleration can occur when a propagating shock interacts with the plasma upstream of the shocks flow direction. As the shock passes through the plasma, particles can become energized as they pass through the shock. Some of the particles can become trapped, bouncing back and forth across the shock, achieving higher energies. These resulting high energy particles retain the compositional characteristics of the un-shocked plasma upstream which the shock passed through. Interplanetary (IP) shocks are caused by many different events in the heliosphere, such as co-rotational interaction regions (CIRs) (*Gosling et al.*, 1976; *Hundhausen and Gosling*, 1976) and coronal mass ejections (CMES) (*Sime and Hundhausen*, 1987; *Vourlidas et al.*, 2003; *Ontiveros and Vourlidas*, 2009). Gradual SEP events associated with CMEs are thought to be accelerated by the CME-driven shock directly from the suprathermal population (*Desai et al.*, 2006).

CMEs are large and powerful eruptions from the Sun which transport plasma and magnetic flux throughout the heliosphere. When observed *in situ* they are referred to as interplanetary coronal mass ejections (ICMEs). ICMEs often travel through the heliosphere at velocities greater than the ambient solar wind, which in turn can drive IP shocks ahead of the ICME (*Sime and Hundhausen*, 1987; *Vourlidas et al.*, 2003; *Ontiveros and Vourlidas*, 2009). A reverse shock can also form in the rear of ICMEs which originate from high latitudes, from either the over-expansion of the ICME flow (*Gosling et al.*, 1988, 1994) or the collision of deflected fast and slow solar wind streams behind the ICME (*Manchester and Zurbuchen*, 2006). The region of heated

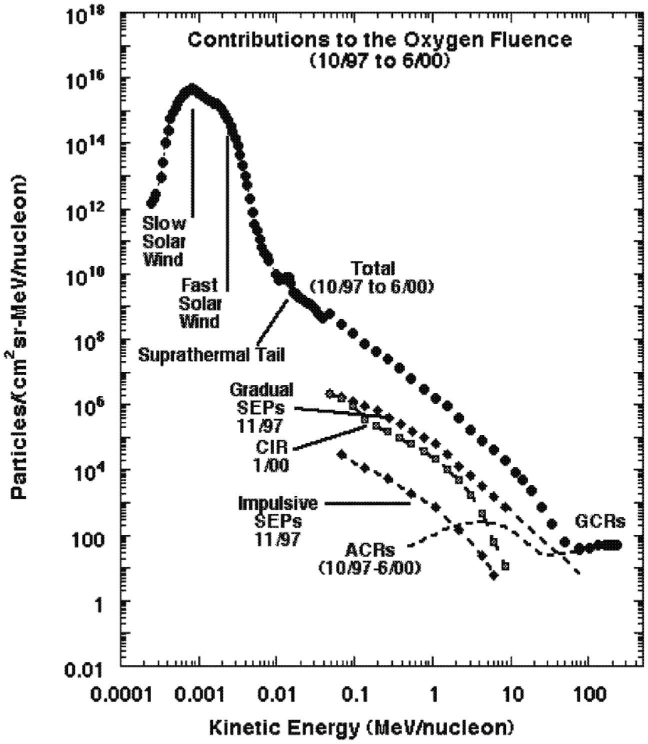

Figure 6.1: The oxygen fluence as observed by the various particle instruments on ACE. The contributions of the solar wind, suprathermals, and higher energy particles are shown. Figure published in (*Mewaldt et al.*, 2001).

plasma between the ICME and the shock is called the sheath. This sheath plasma generally consists of plasma which has piled in front of the ICME as it propagates through the heliosphere. This plasma can become compressed, as the ICME sweeps up more and more plasma, thereby heating the sheath plasma. Downstream of the sheath, we observe the ICME plasma.

ICME plasma has very unique compositional characteristic compared to that of the nominal solar wind composition occurring upstream of the transient (*Lepri and Zurbuchen*, 2004; *Zurbuchen and Richardson*, 2006). It is important to remember, that even though any acceleration mechanism acting on the bulk plasma may require adiabatic heating, the only ramification of this heating is a diffusion of the particles in energy space. The plasmas ionic charge state information has been set close to the sun (*Gruesbeck et al.*, 2011, 2012, and references therein). Further out in the heliosphere, mean free path is too large, due to the expansion of the solar wind and ICME, to allow further ionization or recombination of the charge states. The ionic distribution will therefore remain constant even though the particles are being accelerated by some form of heating. Assuming no mass-per-charge or charge dependent acceleration mechanisms.

Lepri and Zurbuchen (2004) and *Lepri et al.* (2001) have shown that the presence of hot iron charge states in the solar wind are in fact a very strong indicator of ICME plasma. *Gruesbeck et al.* (2011) showed that the bi-modal presence of hot iron charge states, Fe^{16+}, observed simultaneously with cooler, more nominal states, such as Fe^{10+} occur in a majority of ICMEs. Additionally, *Henke et al.* (1998), has shown that the O^{7+}/O^{6+} ratio, observed during ICMEs, can also be elevated, indicating hotter temperatures or greater initial velocities during ejection from the sun. The oxygen charge state enhancements are often correlated with ICMEs exhibiting magnetic cloud topology (*Henke et al.*, 1998).

The charge state distribution of a plasma becomes frozen-in once the volume expands faster than it can adapt to the surrounding environment (*Hundhausen et al.*, 1968). Once frozen-in, the charge state composition of the plasma remains constant as the plasma travels throughout the heliosphere. Freezing-in of the charge state information occurs very close to the sun, usually within the first 5 solar radii (*Hundhausen et al.*, 1968; *Hundhausen*, 1972; *Bame et al.*, 1974; *Buergi and Geiss*, 1986; *Geiss et al.*, 1995). *Gruesbeck et al.* (2011, 2012) has shown that even for the anomalous charge states often observed in ICMEs, the charge state composition is still frozen-in very close to the Sun. Combining this with the unique composition of ICME plasma (*Lepri et al.*, 2001; *Zurbuchen et al.*, 2003; *Lepri and Zurbuchen*, 2004), we are able to constrain the origin of the suprathermal ions present in ICME observations by comparing the composition of the suprathermal plasma to that of he thermal plasma during ICMEs.

This paper presents an analysis of the composition of both the bulk solar wind plasma and the suprathermal plasma, observed during ICMEs time periods, to investigate the source population of the suprathermal plasma found locally inside ICMEs. For this study we present first measurements of the charge state distribution of suprathermal heavy ion plasma occurring during ICMEs. We compare the compositional characteristics of the local suprathermal plasma to that of the local bulk plasma and to the bulk plasma upstream of the shock associated with the ICME. We show that the suprathermal plasma, observed in the ICME, is compositionally similar to the local bulk plasma and not to the bulk plasma found upstream of the CME in the solar wind. This is indicative of an acceleration mechanism acting on the local bulk plasma which energizes the particles up to suprathermal energies and not acceleration of ambient solar wind bulk plasma by the CME-driven shock.

6.2 ICME Observations

ICMEs are large events which have been observed by widely separated spacecraft. Spatially separated observations of a single ICME has led to a greater understanding of their structure and the extent of their influence in the heliosphere (*Kilpua et al.*, 2009, 2011; *Reinard et al.*, 2012; *Lepri et al.*, 2012). We use observations from both the Advanced Composition Explorer (*Stone et al.*, 1998) and the Wind (*Acuña et al.*, 1995; *Harten and Clark*, 1995) spacecraft to compare the plasma properties during a number of ICME observations. These two spacecraft were chosen for a number of reasons. First, in order to fully observe the suprathermal particles we can use observations from the Suprathermal Ion Composition Spectrometer (STICS)(*Gloeckler et al.*, 1995) onboard the Wind spacecraft. STICS is a time-of-flight instrument designed very similarly to the Solar Wind Ion Composition Spectrometer (SWICS) (*Gloeckler et al.*, 1998) onboard the ACE spacecraft. These two instruments are very similar offering comparative data products spanning both the thermal and suprathermal energy regime. Second, after Wind moved out to orbit the L1 point, ACE and Wind were orbiting in close proximity allowing for the co-observation of similar parcels of ICME plasma. We will compare the common plasma parameters used for ICME identification (*Zurbuchen and Richardson*, 2006) from both spacecraft to give us confidence that we are observing the same ICME event simultaneously with both spacecraft.

We use the Suprathermal Ion Composition Spectrometer (*Gloeckler et al.*, 1995) onboard the Wind spacecraft to make the first high-cadence charge state distribution measurements of the suprathermal heavy ions during ICMEs. STICS is a time-of-flight mass spectrometer which measures the mass, energy and charge of ions. STICS observes particles in an energy per charge range of $6.2 - 223.1$ keV/e, allowing high cadence observations of the minor heavy ion phase space distribution for suprathermal energies, observations unique to the instrument. For the composition of the bulk plasma, we use the Solar Wind Ion Composition Spectrometer (SWICS) (*Gloeckler* *et al.*, 1998) onboard the ACE spacecraft. SWICS observes particles in an energy range spanning $0.49 - 100.0$ keV/e, using logarithmically spaced energy bins. Unlike STICS, SWICS is optimized to observe the phase space velocity distributions of the bulk solar wind plasma, but still can observe the very low energy suprathermal contribution. These two energy per charge ranges overlap enabling for validation between the two separate instrument observations. Detector efficiencies limit the time periods where STICS is capable of observing a statistically significant portion of the suprathermal plasma, based on the relative density of the *in situ* plasma, at high cadences, on the order of hours compared to the long accumulations generally used to compute distribution functions for minor ionic species. This makes it hard to calculate the charge state distribution for the plasma in the suprathermal energies.

For this study, we focus on O^{6+}, O^{7+}, Fe^{8+}, Fe^{9+}, Fe^{10+}, Fe^{11+}, Fe^{12+}, Fe^{14+}, and Fe^{16+}, species which have been characterized for the Wind/STICS data. As previously discussed, both oxygen and iron are good discriminators between typical solar wind plasma and ICME plasma. The ions chosen span a range of ionic charge states sufficient to differentiate between the solar wind and ICME plasma.

We used the *Richardson and Cane* (2010) ICME list to determine the time period and boundaries for the ICME observations. We searched this list for events with a significant suprathermal particle population and found a subset of events where two-hour cadence charge state distribution could be made using these nine species. This candidate list consists of fourteen events, separated based on whether the accumulation period occurred during the sheath or the ICME, shown in Table 6.1.

Figure 6.2, shows the ACE observations of one such candidate ICME. The ICME shock was observed on day of year (DOY) 149 of 2003 and the ICME plasma was observed on DOY 150, as reported by *Richardson and Cane* (2010). Panel A shows the solar wind velocity (V_{p}) from the Solar Wind Electron, Proton and Alpha Monitor (SWEPAM) (*McComas et al.*, 1998) and SWICS merged dataset (`http://www.`

Event #	Year	DOY Start	DOY End	ICME	Sheath
1	2000	160.500	162.708	X	
2	2000	195.404	195.708		X
3	2000	195.708	196.583	X	
4	2000	261.706	261.875		X
5	2000	261.875	265.000	X	
6	2001	94.622	94.750		X
7	2001	94.750	95.500	X	
8	2001	328.288	328.583		X
9	2003	149.767	150.083		X
10	2003	150.083	150.667	X	
11	2004	312.769	312.917		X
12	2004	314.833	316.958	X	
13	2005	236.259	236.583		X
14	2005	236.583	236.958	X	

Table 6.1: List of candidate time periods determined where charge state distributions can be calculated for the nine ionic species from the Wind/STICS observations. The type of event, either ICME plasma or sheath plasma, is also indicated.

`srl.caltech.edu/ACE/ASC/level2/lvl3DATA_SWEPAM-SWICS.html`). Also from the SWICS-SWEPAM merged data, panel B shows the proton density (n_p) and panel C shows the proton temperature (T_p). From the Magnetic Field Experiment (MAG) (*Smith et al.*, 1998), panel D shows the magnitude of the magnetic field ($|B|$) and panel E shows the angle of the magnetic field, with the latitudinal angle (λ) in black and the longitudinal angle (δ) in red. The average oxygen charge state ($\langle Q_\mathrm{O} \rangle$) and average iron charge state ($\langle Q_\mathrm{Fe} \rangle$) are shown in panel F and G respectively, calculated from SWICS. Finally, panel H shows the charge state distribution of iron, calculated from SWICS as well. The three vertical lines indicate when the shock is observed (dashed cyan line), the ICME plasma begins (dashed magenta line), and the ICME plasma ends (solid magenta line), all of the time periods obtained from the *Richardson and Cane* (2010) list. Many of the common *in situ* indicators of an ICME are seen in the plasma and magnetic field observations. First, a linearly decreasing bulk velocity throughout the ICME, due to the expansion of the transient, is observed beginning at DOY $\sim$ 150.05, corresponding to the beginning of the ICME period and ending at DOY $\sim$ 150.65, immediately prior to the end of the period (*Russell and Shinde*, 2003). In the magnetic field, we see both a strong increase in the magnitude of the magnetic field, beginning at DOY $\sim$ 150.05, (*Klein and Burlaga*, 1982) as well as smooth rotation of the field during the ICME, from DOY $\sim$ 150.05 to DOY $\sim$ 150.65 (*Klein and Burlaga*, 1982), which could be evidence of an embedded magnetic cloud (*Hirshberg and Colburn*, 1969; *Klein and Burlaga*, 1982; *Zurbuchen and Richardson*, 2006). Finally, we see a drastic increase in the prevalence of hotter iron charge states, beginning as early as DOY $\sim$ 149.55 (*Lepri and Zurbuchen*, 2004).

Figure 6.3 shows *in situ* observations from the Wind spacecraft, during the same time period as Figure 6.2. In panel A, we show the bulk velocity (V_{p}) from the Solar Wind Experiment (SWE) (*Ogilvie et al.*, 1995). Also from SWE, panel B shows the proton density (n_{p}) and panel C shows the proton temperature (T_{p}). Panel D shows the magnitude of the magnetic field ($|B|$) from the Magnetic Field Investigation (MFI) (*Lepping et al.*, 1995). Panel E shows the angle of the magnetic field vector, with the latitudinal direction (λ) in black and the longitudinal direction (δ) in red, also from MFI. The following three panels show compositional measurements from the suprathermal population from STICS. To ensure they are not contaminated with the bulk population, only particles with velocities greater than twice the current bulk speed, as observed by SWE, are considered. As we are only considering multiply charged heavy ions, we do not need to worry about contamination from any pick-up ions as they do not contribute. In a similar fashion to Figure 6.2, we show the average oxygen charge state ($\langle Q_{\mathrm{O}} \rangle$) in panel F, the average iron charge state ($\langle Q_{\mathrm{Fe}} \rangle$) in panel G, and the charge state distribution for iron (Q_{Fe}) in panel H. Once again the same ICME boundaries are denoted by vertical lines. Comparing Figure 6.3 to Figure 6.2 we see considerable similarities in the properties of the plasma. We see a decreasing bulk velocity, beginning at DOY $\sim$ 150.05, an enhanced and smoothly rotating magnetic field, beginning at $\sim$ 150.05, and elevated charge states within

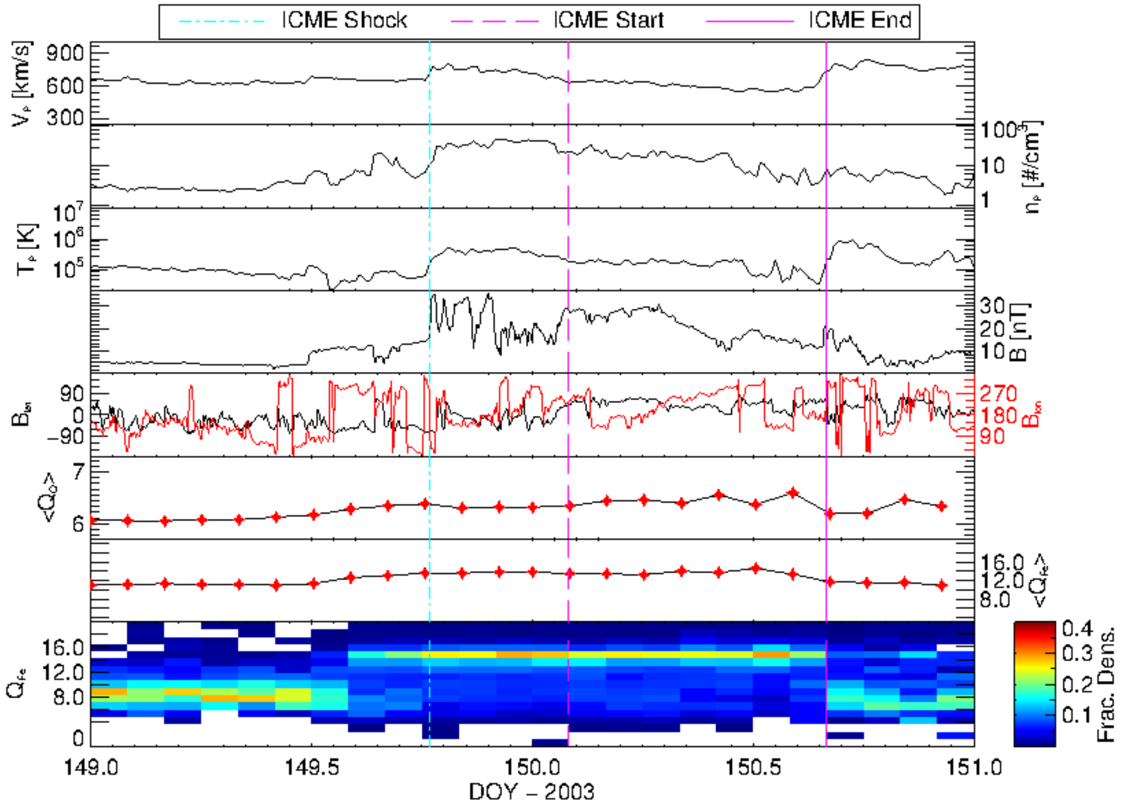

Figure 6.2: Plasma observations of an ICME observed by the ACE spacecraft on DOY 150 of 2003. Panel A-C shows the bulk solar wind velocity (V_{p}), proton density (n_{p}), and proton temperature (T_{p}) respectively, all from SWEPAM. Panel D shows the magnitude of the magnetic field ($|B|$), from MAG. Panel E shows the latitude (λ) and longitude (δ) of the magnetic field vector from MAG. Panel F-H shows the average oxygen charge state ($\langle Q_{\mathrm{O}} \rangle$), average iron charge state ($\langle Q_{\mathrm{Fe}} \rangle$), and the charge state distribution of iron (Q_{Fe}) respectively, all from SWICS. The ICME time periods were determined from *Richardson and Cane* (2010). The dashed cyan line indicates the shock preceding the ICME, the dashed magenta line indicates the beginning of the ICME plasma, and the solid magenta line indicates the end of the ICME plasma.

the ICME of the suprathermal particles, beginning . Additionally, just upstream of the shock, near DOY $\sim$ 149.75, we see nominal iron charge states, much like what is seen in the ACE/SWICS charge state distribution, characteristic of fast solar wind. In general, the plasma observations are very similar on both spacecraft for this ICME observation. These similarities in the plasma parameters implies that the two spacecraft are observing the same plasma, therefore allowing for a valid comparison between the two satellites.

For events 9 and 10, we are able to make suprathermal observations during both the sheath region and inside the ICME itself. Figure 6.4 shows events 13 and 14. The preceding shock was observed on DOY 236 of 2005 with the ICME observed entirely on the same DOY. This figure is presented in an identical format to that of Figure 6.2. Once again, we observe many of the characteristic indicators of ICMEs, such as an enhanced magnetic field with a smooth rotation beginning at DOY $\sim$ 236.57. Figure 6.5 shows the Wind observations for this time period, presented identically to Figure 6.4. Comparing the plasma observations, we once again see a strong resemblance, lending confidence that both spacecraft are observing the same ICME. As can be seen in panels F-H of Figure 6.5 we observe suprathermal plasma for a short duration in this ICME, mostly in the sheath.

To calculate the average charge states and charge state distribution during an ICME time period, we first determine the integrated density of the plasma from the accumulated distribution function. The accumulated distribution function is simply the phase space velocity distribution function that has been accumulated for a specified period of time. For each ICME, we accumulate the observed distribution for a length of time coinciding with the duration of STICS suprathermal observations. Figure 6.6 shows the O^{6+} distribution function observed by Wind/STICS integrated over the entire ICME event 14. The vertical magenta line denotes the two-solar-wind cutoff point, above which we integrate the distribution to obtain the density. From the

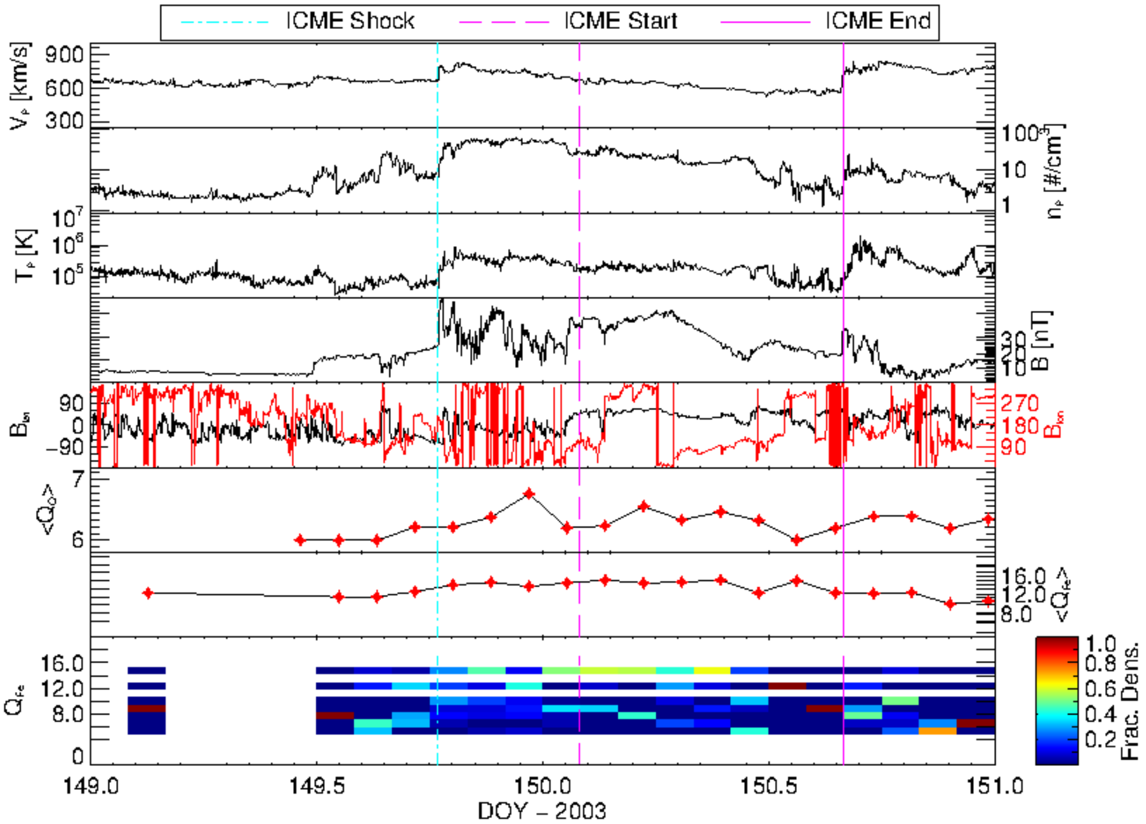

Figure 6.3: Plasma observations of an ICME observed by the Wind spacecraft on DOY 150 of 2003. Panel A-C shows the bulk solar wind velocity (V_{p}), proton density (n_{p}), and proton temperature (T_{p}) respectively, all from SWE. Panel D shows magnitude of the magnetic field ($|B|$) from MFI. Panel E shows the latitude (λ) and longitude (δ) of the magnetic field vector from MFI. Panel F-H shows the average oxygen charge state ($\langle Q_{\mathrm{O}} \rangle$), average iron charge state ($\langle Q_{\mathrm{Fe}} \rangle$), and the charge state distribution of iron (Q_{Fe}) respectively, all calculated from STICS for particle velocities greater than 2 V_{sw}. The ICME time periods were determined from *Richardson and Cane* (2010). The dashed cyan line indicates the shock preceding the ICME, the dashed magenta line indicates the beginning of the ICME plasma, and the solid magenta line indicates the end of the ICME plasma.

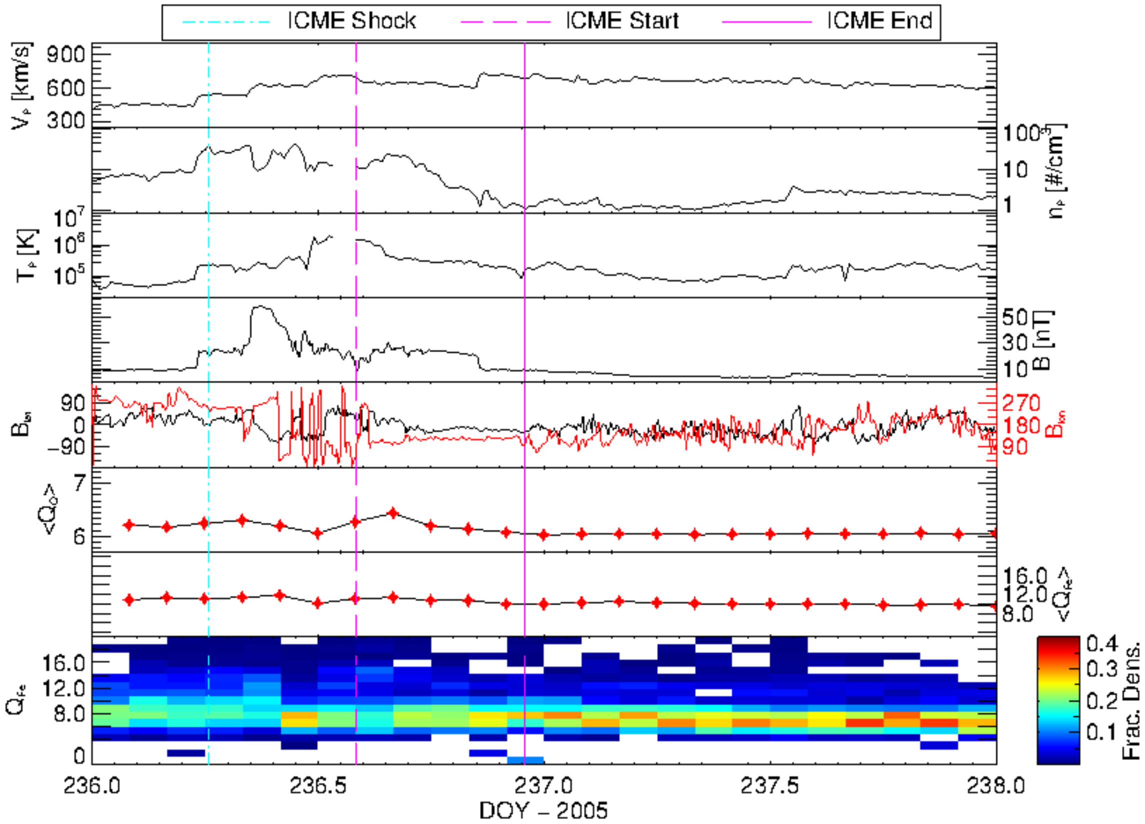

Figure 6.4: Plasma observations of an ICME observed by the ACE spacecraft on DOY 236 of 2005, presented in the same fashion as Figure 6.2

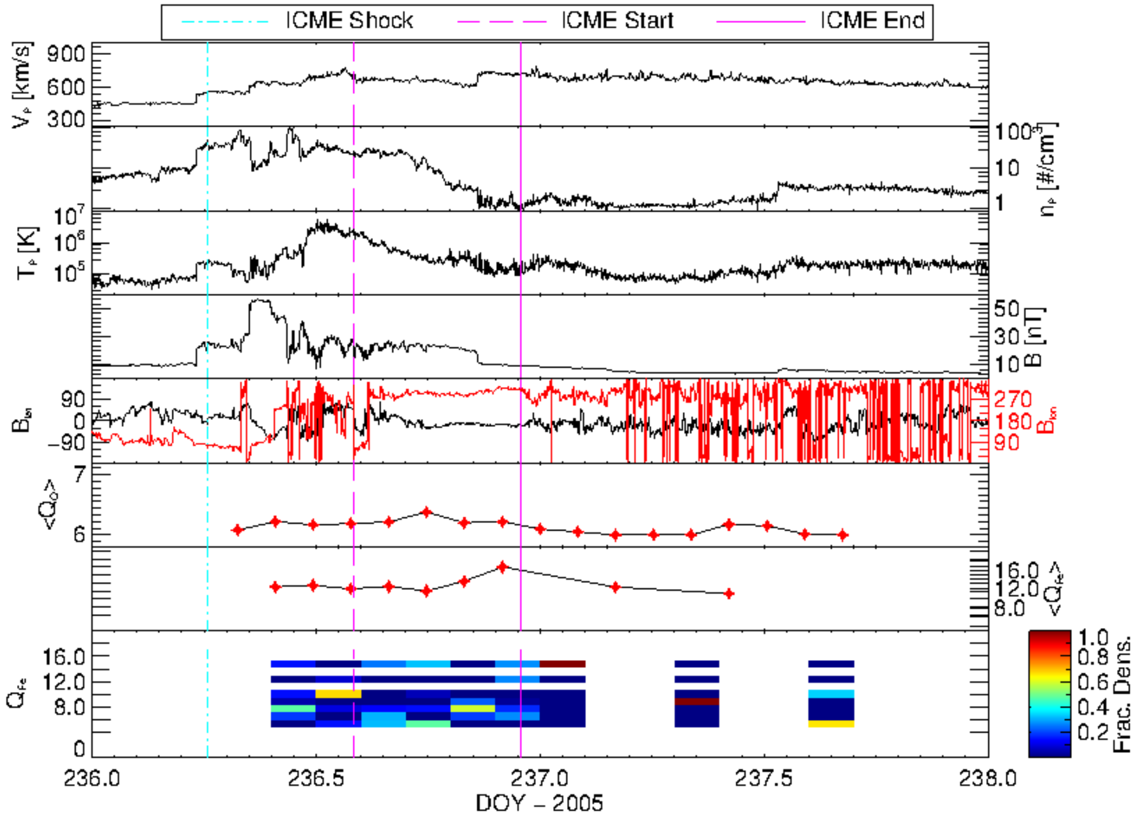

Figure 6.5: Plasma observations of an ICME observed by the Wind spacecraft on DOY 236 of 2005, presented in the same fashion as Figure 6.3

Wind/STICS instrument, we see that a significant portion of the distribution function lies above this cutoff. From each ions' distribution function, we can calculate the relative abundance of each ionic species, $S_{\mathrm{X+}}$. To do this we, we first calculate the total density for all the charge states of the particular atomic species. Next, we then determine the summation of all the densities for each species. Finally, the relative abundance for a particular ionic species is determined from the ratio of the density of the individual ionic species to the total density from all the charge states. This process is shown in Equation 6.1. In Equation 6.1, we show the calculations for the relative abundance of both an oxygen species, $S_{\mathrm{O}^{\mathrm{X}+}}$, and and iron species, $S_{\mathrm{Fe}^{\mathrm{X}+}}$.

$$\begin{aligned} S_{\mathrm{O}^{\mathrm{X}+}} &= \frac{n_{\mathrm{O}^{\mathrm{X}+}}}{n_{\mathrm{O}^{6+}}+n_{\mathrm{O}^{7+}}} \\ S_{\mathrm{Fe}^{\mathrm{X}+}} &= \frac{n_{\mathrm{Fe}^{\mathrm{X}+}}}{n_{\mathrm{Fe}^{8+}}+n_{\mathrm{Fe}^{9+}}+n_{\mathrm{Fe}^{10+}}+n_{\mathrm{Fe}^{11+}}+n_{\mathrm{Fe}^{12+}}+n_{\mathrm{Fe}^{14+}}+n_{\mathrm{Fe}^{16+}}} \end{aligned} \tag{6.1}$$

In Equation 6.1, $n_{\mathrm{O}^{\mathrm{X}+}}$ represents the total density for an ionic species of oxygen and $n_{\mathrm{Fe}^{\mathrm{X}+}}$ is the density for an ionic species of iron.

The average charge state, $\langle Q \rangle$, is then computed by calculating the weighted summation of the relative abundance distribution, where the weight is simply the ionic charge state, as shown in Equation 6.2. We only consider species which both Wind/STICS and ACE/SWICS resolve. For each event we calculate the average charge state, $\langle Q \rangle$, for both the bulk thermal population and the suprathermal population. We divide the events between sheath and ICME components.

$$\begin{aligned} \langle Q_{\mathrm{O}} \rangle &= 6 * S_{\mathrm{O}^{6+}} + 7 * S_{\mathrm{O}^{7+}} \\ \langle Q_{\mathrm{Fe}} \rangle &= 8 * S_{\mathrm{Fe}^{8+}} + 9 * S_{\mathrm{Fe}^{9+}} + 10 * S_{\mathrm{Fe}^{10+}} + \\ & \quad 11 * S_{\mathrm{Fe}^{11+}} + 12 * S_{\mathrm{Fe}^{12+}} + 14 * S_{\mathrm{Fe}^{14+}} + 16 * S_{\mathrm{Fe}^{16+}} \end{aligned} \tag{6.2}$$

In Equation 6.2, $\langle Q_{\mathrm{O}} \rangle$ is the average charge state for oxygen and $\langle Q_{\mathrm{Fe}} \rangle$ is the average charge state of iron. Additionally, $S_{\mathrm{O}^{\mathrm{X}+}}$ is the relative abundance of a ionic species of oxygen and $S_{\mathrm{Fe}^{\mathrm{X}+}}$ is the relative abundance for iron.

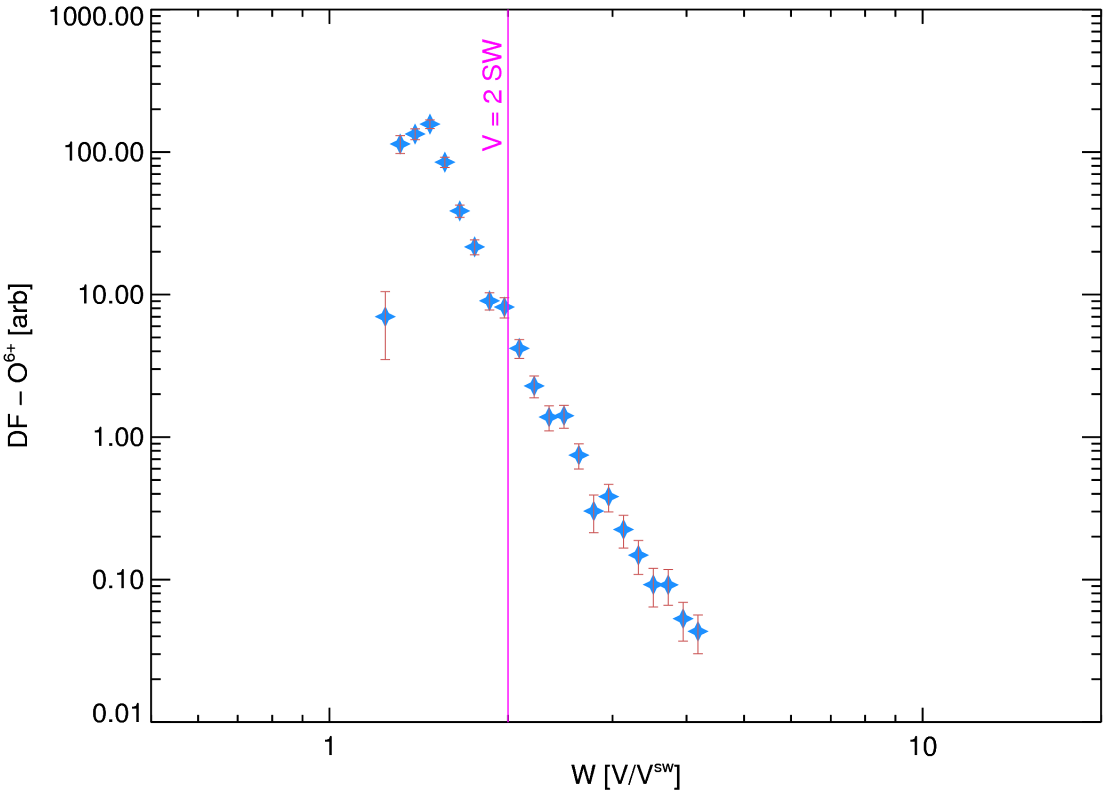

Figure 6.6: The accumulated distribution function of O^{6+} during the ICME on DOY 236 of 2005, observed by the Wind/STICS instrument. The error bars are the propagated statistical counting error. The vertical magenta line shows our separation between the thermal and suprathermal regimes.

6.3 Comparison of Suprathermal and Bulk Plasmas

In order to determine the source of the suprathermal plasma, we analyze the ionic composition of the suprathermal plasma. This plasma will retain the unique characteristics of the seed plasma, if accelerated after it has left the Sun. By determining the thermal plasma that the suprathermal particles originate from, we can further limit the acceleration processes acting on it. We compare the composition of the suprathermal plasma in the ICME to the local bulk plasma, observed during the same time period, and the bulk plasma that is upstream of the CME-driven shock. First, we will consider the average oxygen charge state, for the suprathermal composition, and the bulk composition, data over a portion of the ICME period. The length of the accumulation is determined by the duration of valid STICS observations of suprathermal particles. We calculate and compare the charge states in three regions, upstream of the CME-driven shock, the sheath (when present) and inside the ICME. The upstream bulk state is calculated from a six-hour accumulation period occurring upstream of the CME-driven shock. Again, we constrain the average calculation of the oxygen charge state to only those that we currently report from Wind/STICS.

In Figure 6.7, we show the comparison of the composition of oxygen. The horizontal axis denotes the value of the average charge state of the bulk plasma, calculated from ACE/SWICS. The vertical axis denotes the average charge state of the suprathermal plasma, calculated from Wind/STICS. The blue dots are time periods which occur in the ICME sheath while the green dots are periods occurring within the ICME itself. The error bars represent the standard error of the average. The large size of the vertical error bars is due the consideration of only two species of oxygen. Since O^{6+} and O^{7+} are the primary charge states observed in the solar wind (*Landi et al.*, 2012a), the value of the average state should not vary widely. Panel A shows the local comparison while panel B shows the comparison between suprathermal plasma and the upstream bulk plasma.

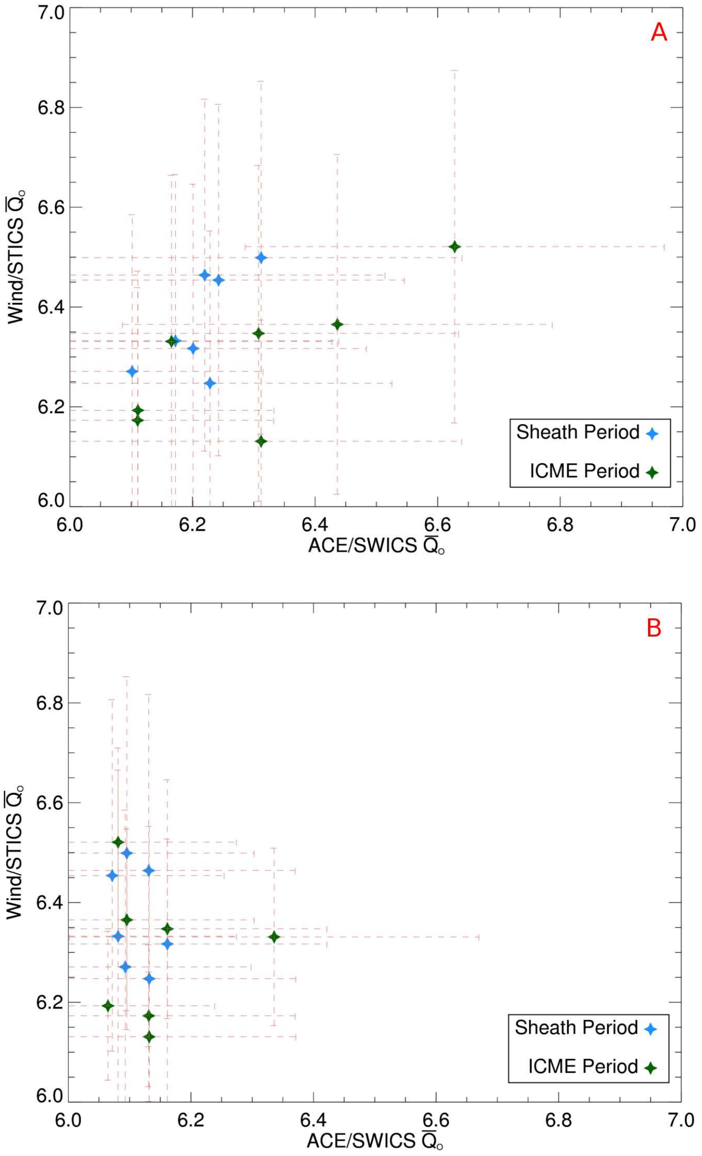

Figure 6.7: The average charge state of oxygen ($\langle Q_{\mathrm{O}} \rangle$) calculated for the bulk population, from ACE/SWICS along the abscissa, and the suprathermal population, from Wind/STICS along the ordinate. Panel A shows a comparison of the local charge states. The green dots are periods where the average charge state was calculated inside of the ICME while the blue dots are for periods in the sheath. In panel A, the average charge state was calculated during the same period for the suprathermal plasma and the bulk plasma, while panel B shows the comparison with the upstream comparison, where the suprathermal plasma charge state is still calculated in either the sheath or ICME, but the bulk plasma charge state is now determined from a 6 hour accumulation upstream of the shock.

In both panels, we can see that the suprathermal plasma spans a charge state range from ~ 6.1 to ~ 6.5. The local bulk plasma shows a similar span of charge states, in panel A, but panel B shows that the upstream bulk plasma is centered towards lower oxygen states, ~ 6.05 to ~ 6.3. In panel A, a more linear relationship between the bulk and suprathermal plasma is apparent, where higher bulk charge states correspond to higher suprathermal charge states. We do not see this same relationship in panel B. Higher suprathermal $\langle Q_{\mathrm{O}} \rangle$ does not correspond to any particular upstream bulk oxygen charge state. Most of the upstream composition is clustered near lower oxygen states. This relationship tells us that the suprathermal oxygen plasma is compositionally similar to local bulk plasma, but does not share a similar correlation to the upstream plasma. Calculating the Pearson's correlation coefficient, r confirms this relationship we observed by eye. The Pearson's correlation coefficient is simply a relation describing the strength of a linear correlation between two variables (*Rodgers and Nicewander*, 1988, and references therein). This score varies between -1 and 1 equating to a strong negative correlation to a strong positive correlation. The comparison of local $\langle Q_{\mathrm{O}} \rangle$ has a score of $r \sim 0.55$, indicating a weak linear correlation, while the upstream comparison has a correlation score of $r \sim -0.12$, which indicates that the two are not correlated at all.

To further validate the results from the oxygen composition we also investigated the composition of iron. Wind/STICS currently resolves a much wider range of iron charge states than oxygen, namely Fe^{8+}, Fe^{9+}, Fe^{10+}, Fe^{11+}, Fe^{12+}, Fe^{14+}, and Fe^{16+}. Additionally, iron has a large range of available charge state present in the solar wind, showing a wider range of charge states when comparing solar wind observations to ICME observations. Figure 6.8 shows the comparisons of the average charge state of suprathermal Fe to the local bulk plasma Fe in panel A, and the upstream bulk solar wind plasma in panel B. These scatterplots are presented in an identical format to Figure 6.7. The difference between the local comparison and the upstream comparison is far more obvious. In the local comparison of panel A, we see the average suprathermal charge state of iron vary from ~ 10 to ~ 15 and the local bulk plasma varying over the same range. The suprathermal plasma is once again linearly related to the local bulk plasma. In panel B, we can see that upstream iron charge state varies from ~ 9 to ~ 11.5, which is more representative of solar wind composition (*Gruesbeck et al.*, 2011, and references therein), while the suprathermal plasma varies over a much wider range. We once again computed the Pearson's correlation coefficient to confirm the relationship we observed visually. The local comparison of suprathermal plasma to the bulk plasma is very strongly correlated, with a value of $r \sim 0.96$, while the upstream correlation is much weaker, with a value of $r \sim 0.42$. While the $\langle Q_{\mathrm{O}} \rangle$ shows a weak correlation, $\langle Q_{\mathrm{Fe}} \rangle$ shows a strong correlation. The oxygen and iron charge state comparisons both show that the suprathermal plasma is compositionally related to the local bulk plasma and not related to the composition of the upstream solar wind plasma.

Figures 6.7 and 6.8 both show that the suprathermal plasma composition observed during the ICME and sheath strongly resembles the local bulk plasma composition. However, the suprathermal plasma does not have a strong relationship with the bulk plasma upstream of the CME-driven shock. This has strong implications on the origin of the suprathermal plasma being accelerated. The suprathermal plasma inside of the ICME is most likely being accelerated out of the local bulk plasma population and not from plasma originating away from the ICME, for instance shock accelerated heliospheric plasma.

6.4 Discussion

Energization at the CME-driven shock is thought to accelerate SEP so they tend to precede ICMEs. They show evidence of energization by means of diffusive shock acceleration (*Reames*, 2013; *Desai et al.*, 2006). When a particle crosses a shock front

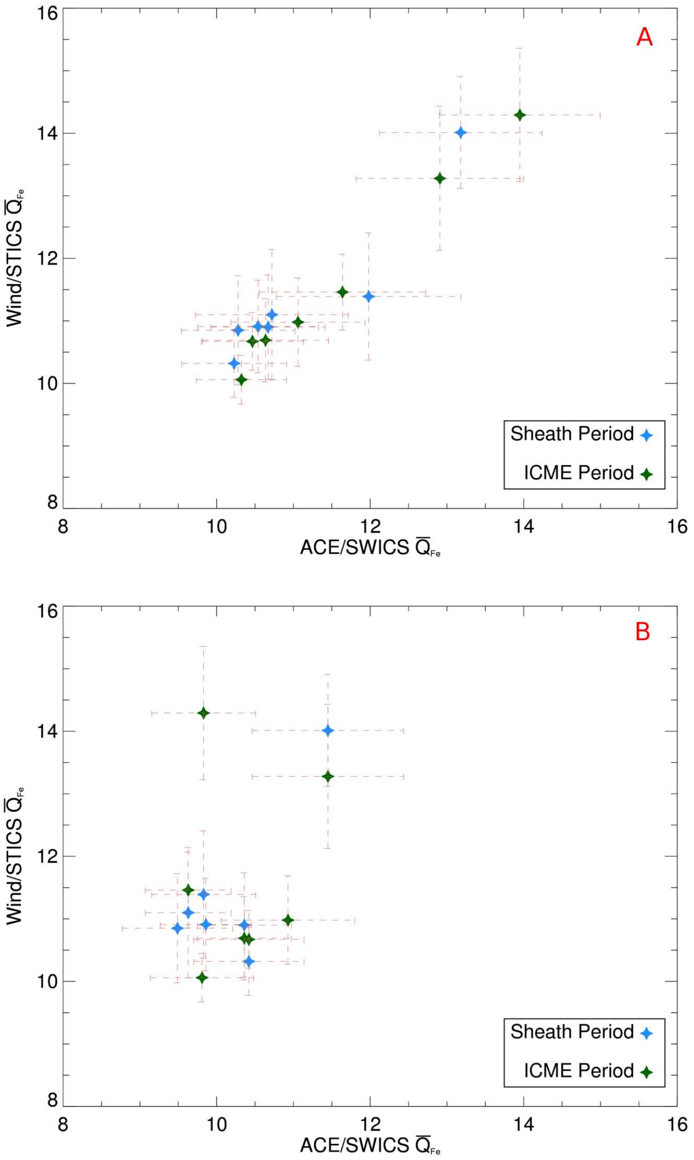

Figure 6.8: The average charge state of iron ($\overline{Q}_{\mathrm{Fe}}$) calculated for the bulk population, from ACE/SWICS along the abscissa, and the suprathermal population, from Wind/STICS along the ordinate. Presented in an identical format to that of Figure 6.7

it can become energized once it enters the region of compressed plasma downstream. This compressed region adiabatically heats the plasma, accelerating the particles within (*Drury*, 1983). Diffusive shock acceleration occurs when a particle becomes trapped near the shock front (*Krymskii*, 1977; *Blandford and Ostriker*, 1978). Once trapped, the particle can bounce back and forth across the shock, experiencing the compression many times thereby accelerating the particle to higher energies with each consecutive interaction (*Lee*, 1983). This process has been used to explain the acceleration of suprathermal plasma from the bulk (*Giacalone*, 2012; *Jokipii and Lee*, 2010), but it has also been argued that the bulk plasma can not be efficiently injected into the shock acceleration process (*Fisk and Gloeckler*, 2012a). Diffusive shock acceleration can only occur if the injected particle is energetic enough allowing its motion to take it back and forth across the shock. Generally, this requires particle energies greater than the thermal energy of the bulk plasma (*Drury*, 1983; *Fisk and Gloeckler*, 2012a). The bulk plasma has a very small portion of particles which would be energetic enough to enter into this mechanism, thus a different mechanism would be needed to account for the propensity of suprathermal plasma observed.

One such alternative could be the pump mechanism introduced by *Fisk and Gloeckler* (2012a). Particles are energized by this mechanism through adiabatic heating due to expansions and contractions in the local plasma. When the plasma is compressed the particles gain energy adiabatically; while the inverse occurs during expansions of the plasma. The more energetic particles of the bulk plasma, once energized further by the compressions, may become mobile enough to escape the turbulent region, retaining their new higher energies. Suprathermal particles may also experience these expansions and in turn become further energized (*Fisk and Gloeckler*, 2012a). This mechanism will act to diffuse the bulk plasma throughout the energy spectrum. A process such as this would accelerate the local bulk plasma up to suprathermal energies.

Compressions and expansions in the local plasma are necessary for the pump mechanism to work. In the solar wind, these compressions can be formed from turbulence of the magnetic field (*Fisk and Gloeckler*, 2008). Such a requirement, makes this process very applicable to a wide variety of plasma regimes, as turbulence occurs in most dynamic systems, and ICMEs are no exception. Turbulence has been observed within ICMEs through remote observations, such as the Ultraviolet Coronagraph Spectrometer (UVCS) on the Solar Heliospheric Observatory (SOHO) (*Telloni et al.*, 2010), as well as *in situ* from magnetic field measurements, such as those from the International Sun/Earth Explorer 3 (ISEE-3) (*Ruzmaikin et al.*, 1997).

We have shown that the suprathermal composition observed in the sheath and ICME is similar to the composition of the local bulk plasma and not the bulk plasma upstream of the shock. If the acceleration of the suprathermal plasma found in the ICME were happening at the shock we would expect two differing scenarios, neither of which are observed. 1) We would expect to see compositions comparable to the upstream plasma if the shock was accelerating the environment it was being driven through, or 2) if the shock was energizing the ICME plasma, we would expect to see a precursor of ICME suprathermal plasma upstream of the shock, but instead we see very few suprathermal counts upstream and when we do it is similar to the thermal plasma. The CME-shock can only accelerate particles at its location upstream of the ICME, as particles have to interact with it to become accelerated. The pump mechanism, however, utilizes turbulence found throughout the plasma to accelerate the particles, allowing for local acceleration throughout the duration of the ICME.

6.5 Conclusion

We have presented some of the first high-cadence observations of suprathermal heavy ion charge state distributions during ICMEs. Using these measurements we have investigated the source population for the suprathermal minor ions present in

ICMEs. Suprathermal plasma is known to be an important seed population for more energetic particles, but the origin of these ions is not well understood. Shock acceleration, a common mechanism to produce energetic particles, may not be an efficient mechanism of elevating bulk solar wind plasma up to suprathermal energies. This leaves the door open for a process which can accelerate the plasma locally, such as the pump acceleration mechanism.

Since, the charge state composition of heliospheric plasma is set very close to the corona, it can be used to differentiate between different plasma populations, assuming no mass-per-charge or charge dependent acceleration mechanisms. Any acceleration occurring further out in the heliosphere will only act to energize the particles and not alter their ionic state. Using ICMEs observed simultaneously by both ACE and the Wind spacecraft, we compared the composition of the bulk plasma to that of the suprathermal plasma. We found that the the composition of the suprathermal plasma is strongly related to that of the co-located bulk plasma and not to the bulk plasma upstream of the shock. The suprathermal plasma seems to be accelerated out of the local bulk plasma and not shock accelerated from upstream plasma.

This alone does not discriminate between a local acceleration mechanism or production during the ejection of the CME. The slowest of suprathermal ions have a velocity that is at least twice that of the flow speed of the bulk plasma. If the suprathermal particles are being produced at the Sun, during the CME eruption, a strong precursor of suprathermal ions should be seen prior to the observation of the ICME, much like is seen with energetic ions (*Smith et al.*, 2004). This however is not observed in our ICME candidates. Instead suprathermal particles are observed inside of the ICME time, co-located with similar bulk plasma. Further, implying that the suprathermal plasma is being accelerated from the local bulk plasma by an acceleration mechanism also occurring locally.

CHAPTER VII

Conclusion

Composition measurements are powerful tools which can be used to discriminate between different types of solar wind plasma, such as slow streamer wind, fast coronal hole wind, and even ICME plasma. Classification of the plasma is possible because the charge state distribution is frozen-in very close to the surface of the Sun. Charge states maintain a fingerprint of the coronal environment from which the measured plasma originated. Over the course of this work, we have presented a series of studies expanding on the usages of *in situ* composition measurements to address key questions which we posed in the Introduction pertaining to the origin of ICME plasma.

7.1 What are the Characteristics of the Early Coronal Environment During CME Eruptions?

The eruption of a CME can be a violent event resulting in hotter than normal plasma temperatures in the corona. Due to this, *in situ* composition measurements of ICME plasma are often indicative of very hot plasma temperatures. During many observations of ICME plasma, charge states similar to the nominal solar wind is often concurrently observed with unusually hot charge states. The nearly ubiquitous observations of bi-modal iron charge state distributions during ICMEs implies that these features are produced by an innate feature of the CME evolution and not from an observational effect or from the mixing of plasma confined to magnetic field lines.

By employing a new charge state evolution model, we investigated the early coronal environment, which determines the *in situ* composition measuremed at 1 AU. The concurrent *in situ* observation of nominal solar plasma and very hot plasma inside of ICMEs is modeled to occur due to a rapid heating of the CME plasma during ejection followed by a subsequent cooling due to adiabatic expansion. Very early in the lifetime of a CME, strong heating is believed to occur from sources such as compressional heating of the plasma during reconnection or heating from an associated flare. A significant heating of the plasma will act to increase the overall charge state of all the atomic species. Further out from the corona, the plasma no longer undergoes heating while the volume continually expands, thereby lowering the temperature and density. The ions undergo recombination and move towards lower charge states, but with the decreasing density the plasma quickly becomes frozen-in. This process enables the production of the bi-modal iron charge state distributions, with the rapid initial heating producing very high charge states. As the plasma cools, a portion of the iron ions approach nominal solar wind values while another significant portion can become stuck at a hotter Ne-like charge state. The plasma quickly becomes frozen-in producing the two peaked charge state distribution.

In addition to the bi-modal iron charge state distributions observed during ICMEs, recent observations have also shown the presence of very cold charge states observed concurrently with these hot ionic charge states inside ICMEs. A single plasma undergoing adiabatic cooling following an initial rapid heating is not able to produce hot ionic states simultaneously with very cold ion states. To produce the cold ionic charge states, the plasma must begin with a very low temperature along with an enhanced electron density allowing for a prolonged period of recombination. In this case, the recombination is so efficient that no hot ionic states remain in the plasma. Another method to produce cold ionic charge states would be for a much weaker initial heating coupled with very cool initial temperatures. In this case, the plasma would never become hot enough to produce the commonly observed high charge states seen in ICME plasma.

Remote observations show that prominence eruptions are often associated with the eruption of a CME. Prominence plasma is generally very dense and cold, ingredients perfect for the production of cold ionic states. The concurrent observations of hot charge states and anomalous cold charge states are likely produced by a mixture of hot ICME plasma and remnant prominence material associated with the ejection of the CME. Prominences are seen to be suspended in the coronal atmosphere along neutral lines occurring in complex magnetic arcades. During the eruption process, the CME's magnetic field may reconnect with those from an associated prominence, thereby allowing the mixing of the two distinct plasmas.

Compositional measurements provide very robust measures of the low coronal environment. They are able to constrain many fundamental plasma properties very close to the Sun. Constraints on this environment can then help to validate current solar wind models by comparing model predictions to the estimates from the ionic composition. In addition, comparisons between different solar wind models and constraints from the composition can be used to investigate various competing heating mechanisms which accelerate the solar wind. Already, it has been shown that many of these models overestimate the early flow velocity. The resulting charge states from solar wind models model have cooler distributions than observed charge states. The plasma is swept through the corona much quicker than expected. This leaves little time for the ions to fully adapt to the surrounding environment, which results in the reduced charge states from the model.

7.2 What is the Origin of the Seed Population for the Suprathermal Plasma?

The source of suprathermal ions is still not fully understood. Utilizing the unique compositional difference between the typical solar wind and the hotter plasma found inside ICMEs, the seed population for the suprathermal particles can be constrained and allow direct comparisons of the competing acceleration mechanisms for these particles. One theory relies on heliospheric shocks to accelerate the bulk plasma into the suprathermal regime, while the other employs local compressions and expansions, potentially caused by turbulence in the magnetic field, to continuously accelerate the local bulk plasma.

If heliospheric shocks accelerate the suprathermal plasma, then the resulting suprathermal ionic composition would be comparable to the ionic composition of the plasma upstream of the shock. However, if an acceleration mechanism which energizes the local plasma is at play, then the suprathermal ionic composition would be comparable to the co-located bulk plasma composition. In a few case studies, we find that the ionic composition of the suprathermal particles resembles the co-located bulk plasma more than the upstream bulk plasma. The suprathermal plasma is most likely being accelerated from the local plasma. However, this alone cannot rule out an acceleration mechanism occurring during the ejection of the CME or in the corona. If this were the case, we would expect a precursor of suprathermal particles, with an ionic composition indicative of ICME plasma. Suprathermal particles generally have velocities at least twice the speed of the local bulk plasma. This implies that the particles could reach the spacecraft quicker than the ICME, much like what is observed from higher energy ions. This is not observed in the cases we investigated, further implying that a continual local acceleration mechanism produces the suprathermal ions.

7.3 Future Work

Many new investigations are possible, directly building upon the work presented in this thesis. First, with the charge state evolution model, we have developed a powerful tool which can predict the coronal plasma environment. We have already discussed the next steps with the model, implementing it as a bridge between spectroscopic measurements and *in situ* observations. However, a number of other investigations should also be conducted. We assume that the electron density distribution is Maxwellian, when estimating the ionization and recombination rates used in the charge state calculation. The electron distribution in the heliosphere actually has a suprathermal tail, taking a kappa distribution shape. To determine the effect of the suprathermal tail of the electron distribution on the charge state evolution, we can incorporate a number of different ionization rates, from varying electron densities, at each radial step of the model. Comparing these results to the results from evolution model using a Maxwellian distribution, we can determine the impact of the suprathermal tail on the frozen-in charge state distribution observed at 1 AU. This is only one example of the new investigations which are possible with the charge state model.

We have only just begun to use the suprathermal plasma observations from the STICS instrument. We have identified a number of time periods where high cadence suprathermal plasma observations can be obtained using the adaptive cadence accumulation method. These periods are not only associated with ICME time periods, but also periods during CIRs and inside the Earth's magnetosphere. Using these time periods, and the full directional capabilities of the instrument, we can investigate the influence of shocks on the suprathermal plasma, at a variety of shock types and strengths. Additionally, periods of heliospheric plasma have been observed inside the magnetosphere of Earth. Using the unique orbit of Wind, we can investigate the processes and effect on solar wind plasma as it leaks into the magnetosphere.

7.4 Final Thoughts

There are many lasting impacts in the work that has been discussed. Charge state composition has long been used as a tool to discriminate between the origin and type of observed plasma populations. It has also been used to probe the coronal electron temperature at the height where the ions become frozen-in. With the advent of our dynamic charge state evolution model, we are able to make estimates of the full coronal electron profile as a function of height from *in situ* composition measurements. This enables us to make important predictions for early coronal heating, expansion, and flow velocities from these composition measurements. Additionally, we investigate the effect of CME expansion on the observed *in situ* composition measurements.

We have presented the first high-cadence observations of the charge state distribution for suprathermal heavy ions present in ICMEs. By using a novel accumulation method, which adaptively sets the cadence for each observation, we determined a number of time periods where high-cadence observations with sufficiently low counting error can be made. Using these ICME time periods, we compared the suprathermal composition to the bulk plasma composition. We find that the suprathermal composition is strongly correlated to the local bulk plasma and not to the bulk plasma upstream of the preceding shock. The suprathermal plasma present in ICMEs is being accelerated from the local bulk plasma and not shock accelerated from the heliospheric plasma the CME is driving through.

The methods introduced in this work can continue to be used in a number of new investigations. Using the charge state evolution model we can bridge the gap between spectroscopic observations and *in situ* composition measurements. This can aid in the end-to-end validation of solar wind models, as well as constrain the early plasma environment to enable further investigations of the heating and acceleration mechanism of the solar wind. The ability to obtain high-cadence observations of suprathermal minor ions, make investigations on the influence of heliospheric features on the suprathermal plasma possible. Wind's unique and long orbit will help to facilitate a wide array of studies, spanning solar cycles as well as plasma environments. This first ICME study is important in the determination of the seed population for the suprathermal plasma, but is only one of the first of many exciting discoveries awaiting to be made from this dataset.

BIBLIOGRAPHY

BIBLIOGRAPHY

Acuña, M. H., K. W. Ogilvie, D. N. Baker, S. A. Curtis, D. H. Fairfield, and W. H. Mish (1995), The Global Geospace Science Program and Its Investigations, *Space Sci. Rev.*, *71*, 5–21, doi:10.1007/BF00751323.

Akmal, A., J. C. Raymond, A. Vourlidas, B. Thompson, A. Ciaravella, Y.-K. Ko, M. Uzzo, and R. Wu (2001), SOHO Observations of a Coronal Mass Ejection, *ApJ*, *553*, 922–934, doi:10.1086/320971.

Antiochos, S. K., R. B. Dahlburg, and J. A. Klimchuk (1994), The magnetic field of solar prominences, *ApJ*, *420*, L41–L44, doi:10.1086/187158.

Antiochos, S. K., C. R. DeVore, and J. A. Klimchuk (1999), A Model for Solar Coronal Mass Ejections, *ApJ*, *510*, 485–493, doi:10.1086/306563.

Aptekar, R. L., et al. (1995), Konus-W Gamma-Ray Burst Experiment for the GGS Wind Spacecraft, *Space Sci. Rev.*, *71*, 265–272, doi:10.1007/BF00751332.

Aulanier, G., N. Srivastava, and S. F. Martin (2000), Model Prediction for an Observed Filament, *ApJ*, *543*, 447–456, doi:10.1086/317095.

Bame, S. J., J. R. Asbridge, W. C. Feldman, and P. D. Kearney (1974), The Quiet Corona: Temperature and Temperature Gradient, *Sol. Phys.*, *35*, 137–152, doi:10.1007/BF00156963.

Bame, S. J., J. R. Asbridge, W. C. Feldman, E. E. Fenimore, and J. T. Gosling (1979), Solar wind heavy ions from flare-heated coronal plasma, *Sol. Phys.*, *62*, 179–201, doi:10.1007/BF00150143.

Bell, A. R. (1978), The acceleration of cosmic rays in shock fronts. I, *MNRAS*, *182*, 147–156.

Blandford, R. D., and J. P. Ostriker (1978), Particle acceleration by astrophysical shocks, *ApJ*, *221*, L29–L32, doi:10.1086/182658.

Boteler, D. H., R. J. Pirjola, and H. Nevanlinna (1998), The effects of geomagnetic disturbances on electrical systems at the earth's surface, *Advances in Space Research*, *22*, 17–27, doi:10.1016/S0273-1177(97)01096-X.

Bougeret, J.-L., et al. (1995), Waves: The Radio and Plasma Wave Investigation on the Wind Spacecraft, *Space Sci. Rev.*, *71*, 231–263, doi:10.1007/BF00751331.

Brueckner, G. E., et al. (1995), The Large Angle Spectroscopic Coronagraph (LASCO), *Sol. Phys.*, *162*, 357–402, doi:10.1007/BF00733434.

Buergi, A., and J. Geiss (1986), Helium and minor ions in the corona and solar wind - Dynamics and charge states, *Sol. Phys.*, *103*, 347–383, doi:10.1007/BF00147835.

Burlaga, L., E. Sittler, F. Mariani, and R. Schwenn (1981), Magnetic loop behind an interplanetary shock - Voyager, Helios, and IMP 8 observations, *J. Geophys. Res.*, *86*, 6673–6684, doi:10.1029/JA086iA08p06673.

Burlaga, L. F., S. P. Plunkett, and O. C. St. Cyr (2002), Successive CMEs and complex ejecta, *Journal of Geophysical Research (Space Physics)*, *107*, 1266, doi:10.1029/2001JA000255.

Canfield, R. C., and K. P. Reardon (1998), The Eruptive Flare of 15 November 1991: Preflare Phenomena, *Sol. Phys.*, *182*, 145–157, doi:10.1023/A:1005086108043.

Chotoo, K. (1998), Measurements of H(+), He(2+), and He(+), in Corotating Interaction Regions at 1 AU, Ph.D. thesis, UNIVERSITY OF MARYLAND COLLEGE PARK.

Chotoo, K., M. R. Collier, A. B. Galvin, D. C. Hamilton, and G. Gloeckler (1998), Extended solar wind helium distribution functions in high-speed streams, *J. Geophys. Res.*, *103*, 17,441–17,446, doi:10.1029/98JA01173.

Chotoo, K., et al. (2000), The suprathermal seed population for corotating interaction region ions at 1 AU deduced from composition and spectra of H(+), He(++), and He(+) observed on Wind, *J. Geophys. Res.*, *105*, 23,107–23,122, doi:10.1029/1998JA000015.

Ciaravella, A., J. C. Raymond, F. Reale, L. Strachan, and G. Peres (2001), 1997 December 12 Helical Coronal Mass Ejection. II. Density, Energy Estimates, and Hydrodynamics, *ApJ*, *557*, 351–365, doi:10.1086/321662.

Ciaravella, A., J. C. Raymond, A. van Ballegooijen, L. Strachan, A. Vourlidas, J. Li, J. Chen, and A. Panasyuk (2003), Physical Parameters of the 2000 February 11 Coronal Mass Ejection: Ultraviolet Spectra versus White-Light Images, *ApJ*, *597*, 1118–1134, doi:10.1086/381220.

Ciaravella, A., et al. (1997), Ultraviolet Coronagraph Spectrometer Observation of the 1996 December 23 Coronal Mass Ejection, *ApJ*, *491*, L59, doi:10.1086/311048.

Cole, D. G. (2003), Space weather: its effects and predictability, *Space Sci. Rev.*, *107*, 295–302, doi:10.1023/A:1025500513499.

Compton, W. D., and C. D. Benson (1983), Living and working in space : a history of Skylab, *NASA Special Publication*, *4208*.

Corona-Romero, P., J. A. Gonzalez-Esparza, and E. Aguilar-Rodriguez (2012), Propagation of Fast Coronal Mass Ejections and Shock Waves Associated with Type II Radio-Burst Emission: An Analytic Study, *Sol. Phys.*, doi:10.1007/s11207-012-0103-9.

Cowan, R. D., and J. B. Mann (1979), Contribution of autoionization to total ionization rates, *ApJ*, *232*, 940–947, doi:10.1086/157357.

Cranmer, S. R., A. A. van Ballegooijen, and R. J. Edgar (2007), Self-consistent Coronal Heating and Solar Wind Acceleration from Anisotropic Magnetohydrodynamic Turbulence, *ApJS*, *171*, 520–551, doi:10.1086/518001.

Culhane, J. L., et al. (2007), The EUV Imaging Spectrometer for Hinode, *Sol. Phys.*, *243*, 19–61, doi:10.1007/s01007-007-0293-1.

Dauphin, C., N. Vilmer, and S. Krucker (2006), Observations of a soft X-ray rising loop associated with a type II burst and a coronal mass ejection in the 03 November 2003 X-ray flare, *A&A*, *455*, 339–348, doi:10.1051/0004-6361:20054535.

Dayeh, M. A., M. I. Desai, J. R. Dwyer, H. K. Rassoul, G. M. Mason, and J. E. Mazur (2009), Composition and Spectral Properties of the 1 AU Quiet-Time Suprathermal Ion Population During Solar Cycle 23, *ApJ*, *693*, 1588–1600, doi:10.1088/0004-637X/693/2/1588.

Dere, K. P., et al. (1997), EIT and LASCO Observations of the Initiation of a Coronal Mass Ejection, *Sol. Phys.*, *175*, 601–612, doi:10.1023/A:1004907307376.

Desai, M. I., G. M. Mason, R. E. Gold, S. M. Krimigis, C. M. S. Cohen, R. A. Mewaldt, J. E. Mazur, and J. R. Dwyer (2006), Heavy-Ion Elemental Abundances in Large Solar Energetic Particle Events and Their Implications for the Seed Population, *ApJ*, *649*, 470–489, doi:10.1086/505649.

Drury, L. O. (1983), An introduction to the theory of diffusive shock acceleration of energetic particles in tenuous plasmas, *Reports on Progress in Physics*, *46*, 973–1027, doi:10.1088/0034-4885/46/8/002.

Edmondson, J. K. (2012), On the Role of Interchange Reconnection in the Generation of the Slow Solar Wind, *Space Sci. Rev.*, *172*, 209–225, doi:10.1007/s11214-011-9767-y.

Fenimore, E. E. (1980), Solar wind flows associated with hot heavy ions, *ApJ*, *235*, 245–257, doi:10.1086/157628.

Fisk, L. A., and G. Gloeckler (2006), The Common Spectrum for Accelerated Ions in the Quiet-Time Solar Wind, *ApJ*, *640*, L79–L82, doi:10.1086/503293.

Fisk, L. A., and G. Gloeckler (2007), Acceleration and Composition of Solar Wind Suprathermal Tails, *Space Sci. Rev.*, *130*, 153–160, doi:10.1007/s11214-007-9180-8.

Fisk, L. A., and G. Gloeckler (2008), Acceleration of Suprathermal Tails in the Solar Wind, *ApJ*, *686*, 1466–1473, doi:10.1086/591543.

Fisk, L. A., and G. Gloeckler (2009), The acceleration of Anomalous Cosmic Rays by stochastic acceleration in the heliosheath, *Advances in Space Research*, *43*, 1471–1478, doi:10.1016/j.asr.2009.02.010.

Fisk, L. A., and G. Gloeckler (2012a), Particle Acceleration in the Heliosphere: Implications for Astrophysics, *Space Sci. Rev.*, *173*, 433–458, doi:10.1007/s11214-012-9899-8.

Fisk, L. A., and G. Gloeckler (2012b), Acceleration of Galactic Cosmic Rays in the Interstellar Medium, *ApJ*, *744*, 127, doi:10.1088/0004-637X/744/2/127.

Fisk, L. A., and M. A. Lee (1980), Shock acceleration of energetic particles in corotating interaction regions in the solar wind, *ApJ*, *237*, 620–626, doi:10.1086/157907.

Forbes, T. G., et al. (2006), CME Theory and Models, *Space Sci. Rev.*, *123*, 251–302, doi:10.1007/s11214-006-9019-8.

Gallagher, P. T., G. R. Lawrence, and B. R. Dennis (2003), Rapid Acceleration of a Coronal Mass Ejection in the Low Corona and Implications for Propagation, *ApJ*, *588*, L53–L56, doi:10.1086/375504.

Galvin, A. B., et al. (2008), The Plasma and Suprathermal Ion Composition (PLASTIC) Investigation on the STEREO Observatories, *Space Sci. Rev.*, *136*, 437–486, doi:10.1007/s11214-007-9296-x.

Geiss, J., et al. (1995), The Southern High-Speed Stream: Results from the SWICS Instrument on Ulysses, *Science*, *268*, 1033–1036, doi:10.1126/science.7754380.

Giacalone, J. (2012), Energetic Charged Particles Associated with Strong Interplanetary Shocks, *ApJ*, *761*, 28, doi:10.1088/0004-637X/761/1/28.

Gibson, S. E., Y. Fan, T. Török, and B. Kliem (2006), The Evolving Sigmoid: Evidence for Magnetic Flux Ropes in the Corona Before, During, and After CMES, *Space Sci. Rev.*, *124*, 131–144, doi:10.1007/s11214-006-9101-2.

Gilbert, H. R., V. H. Hansteen, and T. E. Holzer (2002), Neutral Atom Diffusion in a Partially Ionized Prominence Plasma, *ApJ*, *577*, 464–474, doi:10.1086/342165.

Gilbert, H. R., L. E. Falco, T. E. Holzer, and R. M. MacQueen (2006), Application of a New Technique for Deriving Prominence Mass from SOHO EIT Fe XII (19.5 nm) Absorption Features, *ApJ*, *641*, 606–610, doi:10.1086/500354.

Gilbert, J. A., S. T. Lepri, E. Landi, and T. H. Zurbuchen (2012), First Measurements of the Complete Heavy-ion Charge State Distributions of C, O, and Fe Associated with Interplanetary Coronal Mass Ejections, *ApJ*, *751*, 20, doi:10.1088/0004-637X/751/1/20.

Gloeckler, G., J. Geiss, H. Balsiger, L. A. Fisk, A. B. Galvin, F. M. Ipavich, K. W. Ogilvie, R. von Steiger, and B. Wilken (1993), Detection of interstellar pick-up hydrogen in the solar system, *Science*, *261*, 70–73, doi:10.1126/science.261.5117.70.

Gloeckler, G., L. A. Fisk, S. Hefti, N. A. Schwadron, T. H. Zurbuchen, F. M. Ipavich, J. Geiss, P. Bochsler, and R. F. Wimmer-Schweingruber (1999), Unusual composition of the solar wind in the 2-3 May 1998 CME observed with SWICS on ACE, *Geophys. Res. Lett.*, *26*, 157–160, doi:10.1029/1998GL900166.

Gloeckler, G., L. A. Fisk, T. H. Zurbuchen, and N. A. Schwadron (2000), Sources, injection and acceleration of heliospheric ion populations, in *Acceleration and Transport of Energetic Particles Observed in the Heliosphere*, *American Institute of Physics Conference Series*, vol. 528, edited by R. A. Mewaldt, J. R. Jokipii, M. A. Lee, E. Möbius, and T. H. Zurbuchen, pp. 221–228, doi:10.1063/1.1324316.

Gloeckler, G., T. H. Zurbuchen, and J. Geiss (2003), Implications of the observed anticorrelation between solar wind speed and coronal electron temperature, *Journal of Geophysical Research (Space Physics)*, *108*, 1158, doi:10.1029/2002JA009286.

Gloeckler, G., L. A. Fisk, G. M. Mason, and M. E. Hill (2008), Formation of Power Law Tail with Spectral Index-5 Inside and Beyond the Heliosphere, in *American Institute of Physics Conference Series*, *American Institute of Physics Conference Series*, vol. 1039, edited by G. Li, Q. Hu, O. Verkhoglyadova, G. P. Zank, R. P. Lin, and J. Luhmann, pp. 367–374, doi:10.1063/1.2982473.

Gloeckler, G., et al. (1992), The Solar Wind Ion Composition Spectrometer, *A&AS*, *92*, 267–289.

Gloeckler, G., et al. (1995), The Solar Wind and Suprathermal Ion Composition Investigation on the Wind Spacecraft, *Space Sci. Rev.*, *71*, 79–124, doi:10.1007/BF00751327.

Gloeckler, G., et al. (1998), Investigation of the composition of solar and interstellar matter using solar wind and pickup ion measurements with SWICS and SWIMS on the ACE spacecraft, *Space Sci. Rev.*, *86*, 497–539, doi:10.1023/A:1005036131689.

Goff, C. P., L. van Driel-Gesztelyi, L. K. Harra, S. A. Matthews, and C. H. Mandrini (2005), A slow coronal mass ejection with rising X-ray source, *A&A*, *434*, 761–771, doi:10.1051/0004-6361:20042321.

Gombosi, T. I., D. L. DeZeeuw, C. P. T. Groth, K. G. Powell, and Q. F. Stout (2000), Multiscale MHD simulation of a coronal mass ejection and its interaction with the magnetosphere-ionosphere system, *Journal of Atmospheric and Solar-Terrestrial Physics*, *62*, 1515–1525, doi:10.1016/S1364-6826(00)00091-2.

Gonzalez, W. D., J. A. Joselyn, Y. Kamide, H. W. Kroehl, G. Rostoker, B. T. Tsurutani, and V. M. Vasyliunas (1994), What is a geomagnetic storm?, *J. Geophys. Res.*, *99*, 5771–5792, doi:10.1029/93JA02867.

Gopalswamy, N. (2008), Type II Radio Emission and Solar Energetic Particle Events, in *American Institute of Physics Conference Series*, *American Institute of Physics Conference Series*, vol. 1039, edited by G. Li, Q. Hu, O. Verkhoglyadova, G. P. Zank, R. P. Lin, and J. Luhmann, pp. 196–202, doi:10.1063/1.2982445.

Gopalswamy, N., S. Yashiro, M. L. Kaiser, R. A. Howard, and J.-L. Bougeret (2001), Radio Signatures of Coronal Mass Ejection Interaction: Coronal Mass Ejection Cannibalism?, *ApJ*, *548*, L91–L94, doi:10.1086/318939.

Gopalswamy, N., M. Shimojo, W. Lu, S. Yashiro, K. Shibasaki, and R. A. Howard (2003), Prominence Eruptions and Coronal Mass Ejection: A Statistical Study Using Microwave Observations, *ApJ*, *586*, 562–578, doi:10.1086/367614.

Gopalswamy, N., S. Nunes, S. Yashiro, and R. A. Howard (2004), Variability of solar eruptions during cycle 23, *Advances in Space Research*, *34*, 391–396, doi:10.1016/j.asr.2003.10.054.

Gosling, J. T., V. Pizzo, and S. J. Bame (1973), Anomalously low proton temperatures in the solar wind following interplanetary shock waves–evidence for magnetic bottles?, *J. Geophys. Res.*, *78*, 2001, doi:10.1029/JA078i013p02001.

Gosling, J. T., E. Hildner, R. M. MacQueen, R. H. Munro, A. I. Poland, and C. L. Ross (1974), Mass ejections from the sun - A view from SKYLAB, *J. Geophys. Res.*, *79*, 4581–4587, doi:10.1029/JA079i031p04581.

Gosling, J. T., A. J. Hundhausen, and S. J. Bame (1976), Solar wind stream evolution at large heliocentric distances - Experimental demonstration and the test of a model, *J. Geophys. Res.*, *81*, 2111–2122, doi:10.1029/JA081i013p02111.

Gosling, J. T., J. R. Asbridge, S. J. Bame, W. C. Feldman, and R. D. Zwickl (1980), Observations of large fluxes of He/+/ in the solar wind following an interplanetary shock, *J. Geophys. Res.*, *85*, 3431–3434, doi:10.1029/JA085iA07p03431.

Gosling, J. T., S. J. Bame, E. J. Smith, and M. E. Burton (1988), Forward-reverse shock pairs associated with transient disturbances in the solar wind at 1 AU, *J. Geophys. Res.*, *93*, 8741–8748, doi:10.1029/JA093iA08p08741.

Gosling, J. T., D. J. McComas, J. L. Phillips, L. A. Weiss, V. J. Pizzo, B. E. Goldstein, and R. J. Forsyth (1994), A new class of forward-reverse shock pairs in the solar wind, *Geophys. Res. Lett.*, *21*, 2271–2274, doi:10.1029/94GL02245.

Gruesbeck, J. R., S. T. Lepri, T. H. Zurbuchen, and S. K. Antiochos (2011), Constraints on Coronal Mass Ejection Evolution from in Situ Observations of Ionic Charge States, *ApJ*, *730*, 103, doi:10.1088/0004-637X/730/2/103.

Gruesbeck, J. R., S. T. Lepri, and T. H. Zurbuchen (2012), Two-plasma Model for Low Charge State Interplanetary Coronal Mass Ejection Observations, *ApJ*, *760*, 141, doi:10.1088/0004-637X/760/2/141.

Hansteen, V. H., and E. Leer (1995), Coronal heating, densities, and temperatures and solar wind acceleration, *J. Geophys. Res.*, *100*, 21,577–21,594, doi:10.1029/95JA02300.

Hansteen, V. H., and M. Velli (2012), Solar Wind Models from the Chromosphere to 1 AU, *Space Sci. Rev.*, *172*, 89–121, doi:10.1007/s11214-012-9887-z.

Harrison, R. A. (1995), The nature of solar flares associated with coronal mass ejection., *A&A*, *304*, 585.

Harrison, R. A., et al. (2008), First Imaging of Coronal Mass Ejections in the Heliosphere Viewed from Outside the Sun Earth Line, *Sol. Phys.*, *247*, 171–193, doi:10.1007/s11207-007-9083-6.

Harten, R., and K. Clark (1995), The Design Features of the GGS Wind and Polar Spacecraft, *Space Sci. Rev.*, *71*, 23–40, doi:10.1007/BF00751324.

Henke, T., J. Woch, R. Schwenn, U. Mall, G. Gloeckler, R. von Steiger, R. J. Forsyth, and A. Balogh (2001), Ionization state and magnetic topology of coronal mass ejections, *J. Geophys. Res.*, *106*, 10,597–10,614, doi:10.1029/2000JA900176.

Henke, T., et al. (1998), Differences in the O^{7+}/O^{6+} ratio of magnetic cloud and non-cloud coronal mass ejections, *Geophys. Res. Lett.*, *25*, 3465–3468, doi:10.1029/98GL02632.

Hill, M. E., N. A. Schwadron, D. C. Hamilton, R. D. Di Fabio, and R. K. Squier (2009), Interplanetary Suprathermal He^{+} and He^{++} Observations During Quiet Periods from 1 to 9 AU and Implications for Particle Acceleration, *ApJ*, *699*, L26–L30, doi:10.1088/0004-637X/699/1/L26.

Hirshberg, J., and D. S. Colburn (1969), Interplanetary field and geomagnetic variations-a unified view, *Planet. Space Sci.*, *17*, 1183, doi:10.1016/0032-0633(69)90010-5.

Hirshberg, J., J. R. Asbridge, and D. E. Robbins (1971), The Helium-Enriched Interplanetary Plasma from the Proton Flares of August/September, 1966, *Sol. Phys.*, *18*, 313–320, doi:10.1007/BF00145946.

House, L. L., W. J. Wagner, E. Hildner, C. Sawyer, and H. U. Schmidt (1981), Studies of the corona with the Solar Maximum Mission coronagraph/polarimeter, *ApJ*, *244*, L117–L121, doi:10.1086/183494.

Hundhausen, A. (1972), *Coronal Expansion and Solar Wind*, *Physics and Chemistry in Space*, vol. 5, Springer, Berlin; New York.

Hundhausen, A. J. (1987), The Origin and Propagation of Coronal Mass Ejections (R), in *Sixth International Solar Wind Conference*, edited by V. J. Pizzo, T. Holzer, and D. G. Sime, p. 181.

Hundhausen, A. J., and J. T. Gosling (1976), Solar wind structure at large heliocentric distances - an interpretation of Pioneer 10 observations, *J. Geophys. Res.*, *81*, 1436–1440, doi:10.1029/JA081i007p01436.

Hundhausen, A. J., H. E. Gilbert, and S. J. Bame (1968), Ionization state of the interplanetary plasma, *J. Geophys. Res.*, *73*, 5485, doi:10.1029/JA073i017p05485.

Illing, R. M. E., and A. J. Hundhausen (1985), Observation of a coronal transient from 1.2 to 6 solar radii, *J. Geophys. Res.*, *90*, 275–282, doi:10.1029/JA090iA01p00275.

Illing, R. M. E., and A. J. Hundhausen (1986), Disruption of a coronal streamer by an eruptive prominence and coronal mass ejection, *J. Geophys. Res.*, *91*, 10,951–10,960, doi:10.1029/JA091iA10p10951.

Jian, L., C. T. Russell, J. G. Luhmann, and R. M. Skoug (2006), Properties of Interplanetary Coronal Mass Ejections at One AU During 1995 2004, *Sol. Phys.*, *239*, 393–436, doi:10.1007/s11207-006-0133-2.

Jin, M., et al. (2012), A Global Two-temperature Corona and Inner Heliosphere Model: A Comprehensive Validation Study, *ApJ*, *745*, 6, doi:10.1088/0004-637X/745/1/6.

Jokipii, J. R., and M. A. Lee (2010), Compression Acceleration in Astrophysical Plasmas and the Production of f(v) vprop v $^{-5}$ Spectra in the Heliosphere, *ApJ*, *713*, 475–483, doi:10.1088/0004-637X/713/1/475.

Kaiser, M. L., T. A. Kucera, J. M. Davila, O. C. St. Cyr, M. Guhathakurta, and E. Christian (2008), The STEREO Mission: An Introduction, *Space Sci. Rev.*, *136*, 5–16, doi:10.1007/s11214-007-9277-0.

Karpen, J. T., S. K. Antiochos, M. Hohensee, J. A. Klimchuk, and P. J. MacNeice (2001), Are Magnetic Dips Necessary for Prominence Formation?, *ApJ*, *553*, L85–L88, doi:10.1086/320497.

Kilpua, E. K. J., L. K. Jian, Y. Li, J. G. Luhmann, and C. T. Russell (2011), Multipoint ICME encounters: Pre-STEREO and STEREO observations, *Journal of Atmospheric and Solar-Terrestrial Physics*, *73*, 1228–1241, doi:10.1016/j.jastp.2010.10.012.

Kilpua, E. K. J., et al. (2009), Multispacecraft Observations of Magnetic Clouds and Their Solar Origins between 19 and 23 May 2007, *Sol. Phys.*, *254*, 325–344, doi:10.1007/s11207-008-9300-y.

Klein, L. W., and L. F. Burlaga (1982), Interplanetary magnetic clouds at 1 AU, *J. Geophys. Res.*, *87*, 613–624, doi:10.1029/JA087iA02p00613.

Ko, Y.-K., L. A. Fisk, J. Geiss, G. Gloeckler, and M. Guhathakurta (1997), An Empirical Study of the Electron Temperature and Heavy Ion Velocities in the South Polar Coronal Hole, *Sol. Phys.*, *171*, 345–361.

Koskinen, H. E. J., and K. E. J. Huttunen (2006), Geoeffectivity of Coronal Mass Ejections, *Space Sci. Rev.*, *124*, 169–181, doi:10.1007/s11214-006-9103-0.

Krucker, S., H. S. Hudson, L. Glesener, S. M. White, S. Masuda, J.-P. Wuelser, and R. P. Lin (2010), Measurements of the Coronal Acceleration Region of a Solar Flare, *ApJ*, *714*, 1108–1119, doi:10.1088/0004-637X/714/2/1108.

Krymskii, G. F. (1977), A regular mechanism for the acceleration of charged particles on the front of a shock wave, *Akademiia Nauk SSSR Doklady*, *234*, 1306–1308.

Laming, J. M., and S. T. Lepri (2007), Ion Charge States in the Fast Solar Wind: New Data Analysis and Theoretical Refinements, *ApJ*, *660*, 1642–1652, doi:10.1086/513505.

Laming, J. M., J. D. Moses, Y.-K. Ko, C. K. Ng, C. E. Rakowski, and A. J. Tylka (2013), On the Remote Detection of Suprathermal Ions in the Solar Corona and their Role as Seeds for Solar Energetic Particle Production, *ApJ*, *770*, 73, doi:10.1088/0004-637X/770/1/73.

Landi, E., R. L. Alexander, J. R. Gruesbeck, J. A. Gilbert, S. T. Lepri, W. B. Manchester, and T. H. Zurbuchen (2012a), Carbon Ionization Stages as a Diagnostic of the Solar Wind, *ApJ*, *744*, 100, doi:10.1088/0004-637X/744/2/100.

Landi, E., J. R. Gruesbeck, S. T. Lepri, and T. H. Zurbuchen (2012b), New Solar Wind Diagnostic Using Both in Situ and Spectroscopic Measurements, *ApJ*, *750*, 159, doi:10.1088/0004-637X/750/2/159.

Landi, E., J. R. Gruesbeck, S. T. Lepri, T. H. Zurbuchen, and L. A. Fisk (2012c), Charge State Evolution in the Solar Wind. Radiative Losses in Fast Solar Wind Plasmas, *ApJ*, *758*, L21, doi:10.1088/2041-8205/758/1/L21.

Landi, E., J. R. Gruesbeck, S. T. Lepri, T. H. Zurbuchen, and L. A. Fisk (2012d), Charge State Evolution in the Solar Wind. II. Plasma Charge State Composition in the Inner Corona and Accelerating Fast Solar Wind, *ApJ*, *761*, 48, doi:10.1088/0004-637X/761/1/48.

Larson, W. J., and J. R. Wertz (2005), *Space Mission and Design*, Space Technology Series, third ed., Microsom Press, El Segundo; Califronia.

Lee, M. A. (1983), Coupled hydromagnetic wave excitation and ion acceleration at interplanetary traveling shocks, *J. Geophys. Res.*, *88*, 6109–6119, doi:10.1029/JA088iA08p06109.

Lee, M. A., R. A. Mewaldt, and J. Giacalone (2012), Shock Acceleration of Ions in the Heliosphere, *Space Sci. Rev.*, *173*, 247–281, doi:10.1007/s11214-012-9932-y.

Lepping, R. P., L. F. Burlaga, and J. A. Jones (1990), Magnetic field structure of interplanetary magnetic clouds at 1 AU, *J. Geophys. Res.*, *95*, 11,957–11,965, doi:10.1029/JA095iA08p11957.

Lepping, R. P., et al. (1995), The Wind Magnetic Field Investigation, *Space Sci. Rev.*, *71*, 207–229, doi:10.1007/BF00751330.

Lepri, S. T., and T. H. Zurbuchen (2004), Iron charge state distributions as an indicator of hot ICMEs: Possible sources and temporal and spatial variations during solar maximum, *J. Geophys. Res.*, *109*, A01112, doi:10.1029/2003JA009954.

Lepri, S. T., and T. H. Zurbuchen (2010), Direct Observational Evidence of Filament Material Within Interplanetary Coronal Mass Ejections, *ApJ*, *723*, L22–L27, doi:10.1088/2041-8205/723/1/L22.

Lepri, S. T., T. H. Zurbuchen, L. A. Fisk, I. G. Richardson, H. V. Cane, and G. Gloeckler (2001), Iron charge distribution as an identifier of interplanetary coronal mass ejections, *J. Geophys. Res.*, *106*, 29,231–29,238, doi:10.1029/2001JA000014.

Lepri, S. T., J. M. Laming, C. E. Rakowski, and R. von Steiger (2012), Spatially Dependent Heating and Ionization in an ICME Observed by Both ACE and Ulysses, *ApJ*, *760*, 105, doi:10.1088/0004-637X/760/2/105.

Li, Y., B. J. Lynch, G. Stenborg, J. G. Luhmann, K. E. J. Huttunen, B. T. Welsch, P. C. Liewer, and A. Vourlidas (2008), The Solar Magnetic Field and Coronal Dynamics of the Eruption on 2007 May 19, *ApJ*, *681*, L37–L40, doi:10.1086/590340.

Lin, R. P., et al. (1995), A Three-Dimensional Plasma and Energetic Particle Investigation for the Wind Spacecraft, *Space Sci. Rev.*, *71*, 125–153, doi:10.1007/BF00751328.

Lin, R. P., et al. (2003), RHESSI Observations of Particle Acceleration and Energy Release in an Intense Solar Gamma-Ray Line Flare, *ApJ*, *595*, L69–L76, doi:10.1086/378932.

Linker, J. A., G. van Hoven, and D. D. Schnack (1990), MHD simulations of coronal mass ejections - Importance of the driving mechanism, *J. Geophys. Res.*, *95*, 4229–4238, doi:10.1029/JA095iA04p04229.

Low, B. C. (1996), Solar Activity and the Corona, *Sol. Phys.*, *167*, 217–265, doi:10.1007/BF00146338.

Low, B. C. (1999), Coronal Mass Ejections, flares and prominences, in *American Institute of Physics Conference Series*, *American Institute of Physics Conference Series*, vol. 471, edited by S. R. Habbal, R. Esser, J. V. Hollweg, and P. A. Isenberg, pp. 109–114, doi:10.1063/1.58788.

Low, B. C., R. H. Munro, and R. R. Fisher (1982), The initiation of a coronal transient, *ApJ*, *254*, 335–342, doi:10.1086/159737.

Low, B. C., B. Fong, and Y. Fan (2003), The Mass of a Solar Quiescent Prominence, *ApJ*, *594*, 1060–1067, doi:10.1086/377042.

Lynch, B. J., S. K. Antiochos, P. J. MacNeice, T. H. Zurbuchen, and L. A. Fisk (2004), Observable Properties of the Breakout Model for Coronal Mass Ejections, *ApJ*, *617*, 589–599, doi:10.1086/424564.

Lynch, B. J., et al. (2011), Ionic Composition Structure of Coronal Mass Ejections in Axisymmetric Magnetohydrodynamic Models, *ApJ*, *740*, 112, doi:10.1088/0004-637X/740/2/112.

MacQueen, R. M., J. A. Eddy, J. T. Gosling, E. Hildner, R. H. Munro, G. A. Newkirk, Jr., A. I. Poland, and C. L. Ross (1974), The Outer Solar Corona as Observed from Skylab: Preliminary Results, *ApJ*, *187*, L85, doi:10.1086/181402.

MacQueen, R. M., A. Csoeke-Poeckh, E. Hildner, L. House, R. Reynolds, A. Stanger, H. Tepoel, and W. Wagner (1980), The High Altitude Observatory Coronagraph/Polarimeter on the Solar Maximum Mission, *Sol. Phys.*, *65*, 91–107, doi:10.1007/BF00151386.

Mall, U., E. Kirsch, K. Cierpka, B. Wilken, A. Söding, F. Neubauer, G. Gloeckler, and A. Galvin (1998), Direct observation of lunar pick-up ions near the Moon, *Geophys. Res. Lett.*, *25*, 3799–3802, doi:10.1029/1998GL900003.

Manchester, W. B., and T. H. Zurbuchen (2006), Are high-latitude forward-reverse shock pairs driven by CME overexpansion?, *Journal of Geophysical Research (Space Physics)*, *111*, A05101, doi:10.1029/2005JA011461.

Marsch, E., R. von Steiger, and P. Bochsler (1995), Element fractionation by diffusion in the solar chromosphere., *A&A*, *301*, 261.

Mason, G. M., M. I. Desai, and G. Li (2012), Solar Cycle Abundance Variations in Corotating Interaction Regions: Evidence for a Suprathermal Ion Seed Population, *ApJ*, *748*, L31, doi:10.1088/2041-8205/748/2/L31.

Mazzotta, P., G. Mazzitelli, S. Colafrancesco, and N. Vittorio (1998), Ionization balance for optically thin plasmas: Rate coefficients for all atoms and ions of the elements H to NI, *A&AS*, *133*, 403–409, doi:10.1051/aas:1998330.

McComas, D. J., J. L. Phillips, S. J. Bame, J. T. Gosling, B. E. Goldstein, and M. Neugebauer (1995), Ulysses solar wind observations to 56° south, *Space Sci. Rev.*, *72*, 93–98, doi:10.1007/BF00768760.

McComas, D. J., S. J. Bame, P. Barker, W. C. Feldman, J. L. Phillips, P. Riley, and J. W. Griffee (1998), Solar Wind Electron Proton Alpha Monitor (SWEPAM) for the Advanced Composition Explorer, *Space Sci. Rev.*, *86*, 563–612, doi:10.1023/A:1005040232597.

Mewaldt, R. A., C. M. S. Cohen, and G. M. Mason (2006), The Source Material for Large Solar Energetic Particle Events, *Washington DC American Geophysical Union Geophysical Monograph Series*, *165*, 115–126.

Mewaldt, R. A., et al. (2001), Long-term fluences of energetic particles in the heliosphere, in *Joint SOHO/ACE workshop "Solar and Galactic Composition"*, *American Institute of Physics Conference Series*, vol. 598, edited by R. F. Wimmer-Schweingruber, pp. 165–170, doi:10.1063/1.1433995.

Mulligan, T., and C. T. Russell (2001), Multispacecraft modeling of the flux rope structure of interplanetary coronal mass ejections: Cylindrically symmetric versus nonsymmetric topologies, *J. Geophys. Res.*, *106*, 10,581–10,596, doi: 10.1029/2000JA900170.

Munro, R. H., J. T. Gosling, E. Hildner, R. M. MacQueen, A. I. Poland, and C. L. Ross (1979), The association of coronal mass ejection transients with other forms of solar activity, *Sol. Phys.*, *61*, 201–215, doi:10.1007/BF00155456.

Neugebauer, M., and C. W. Snyder (1962), Solar Plasma Experiment, *Science*, *138*, 1095–1097, doi:10.1126/science.138.3545.1095-a.

Neugebauer, M., P. C. Liewer, E. J. Smith, R. M. Skoug, and T. H. Zurbuchen (2002), Sources of the solar wind at solar activity maximum, *Journal of Geophysical Research (Space Physics)*, *107*, 1488, doi:10.1029/2001JA000306.

Neukomm, R. O., and P. Bochsler (1996), Diagnostics of Closed Magnetic Structures in the Solar Corona Using Charge States of Helium and of Minor Ions, *ApJ*, *465*, 462, doi:10.1086/177433.

Ogilvie, K. W., et al. (1995), SWE, A Comprehensive Plasma Instrument for the Wind Spacecraft, *Space Sci. Rev.*, *71*, 55–77, doi:10.1007/BF00751326.

Ontiveros, V., and A. Vourlidas (2009), Quantitative Measurements of Coronal Mass Ejection-Driven Shocks from LASCO Observations, *ApJ*, *693*, 267–275, doi: 10.1088/0004-637X/693/1/267.

Owens, M. J., N. U. Crooker, N. A. Schwadron, T. S. Horbury, S. Yashiro, H. Xie, O. C. St. Cyr, and N. Gopalswamy (2008), Conservation of open solar magnetic flux and the floor in the heliospheric magnetic field, *Geophys. Res. Lett.*, *35*, L20108, doi:10.1029/2008GL035813.

Palmer, D. M., et al. (1995), First Results from the TGRS High-Resolution GRB Spectrometer, *Ap&SS*, *231*, 161–164, doi:10.1007/BF00658608.

Parker, E. N. (1958), Dynamics of the Interplanetary Gas and Magnetic Fields., *ApJ*, *128*, 664, doi:10.1086/146579.

Parker, E. N. (1965), Dynamical Theory of the Solar Wind, *Space Sci. Rev.*, *4*, 666–708, doi:10.1007/BF00216273.

Patsourakos, S., A. Vourlidas, and G. Stenborg (2010), The Genesis of an Impulsive Coronal Mass Ejection Observed at Ultra-high Cadence by AIA on SDO, *ApJ*, *724*, L188–L193, doi:10.1088/2041-8205/724/2/L188.

Posner, A., N. A. Schwadron, T. H. Zurbuchen, J. U. Kozyra, M. W. Liemohn, and G. Gloeckler (2002), Association of Low-Charge-State Heavy Ions up to 200 R_e upstream of the Earth's bow shock with geomagnetic disturbances, *Geophys. Res. Lett.*, *29*, 1099, doi:10.1029/2001GL013449.

Posner, A., M. W. Liemohn, and T. H. Zurbuchen (2003), Upstream magnetospheric ion flux tube within a magnetic cloud: Wind/STICS, *Geophys. Res. Lett.*, *30*, 1346, doi:10.1029/2002GL016116.

Press, W. H., S. A. Teukolsky, W. T. Vetterling, and B. P. Flannery (2002), *Numerical recipes in C++ : the art of scientific computing*, Cambridge University Press.

Rakowski, C. E., J. M. Laming, and S. T. Lepri (2007), Ion Charge States in Halo Coronal Mass Ejections: What Can We Learn about the Explosion?, *ApJ*, *667*, 602–609, doi:10.1086/520914.

Reames, D. V. (2013), The Two Sources of Solar Energetic Particles, *Space Sci. Rev.*, doi:10.1007/s11214-013-9958-9.

Reinard, A. (2005), Comparison of Interplanetary CME Charge State Composition with CME-associated Flare Magnitude, *ApJ*, *620*, 501–505, doi:10.1086/426109.

Reinard, A., T. Mulligan, and B. Lynch (2010), Quadrature comparisons of remote and in-situ CME ejecta, in *38th COSPAR Scientific Assembly*, *COSPAR Meeting*, vol. 38, p. 1874.

Reinard, A. A., B. J. Lynch, and T. Mulligan (2012), Composition Structure of Interplanetary Coronal Mass Ejections From Multispacecraft Observations, Modeling, and Comparison with Numerical Simulations, *ApJ*, *761*, 175, doi:10.1088/0004-637X/761/2/175.

Reitz, G., R. Beaujean, C. Heilmann, J. Kopp, M. Leicher, and K. Strauch (1998), Results of dosimetric measurements in space missions, *Advances in Space Research*, *22*, 495–500, doi:10.1016/S0273-1177(98)01069-2.

Richardson, I. G., and H. V. Cane (1995), Regions of abnormally low proton temperature in the solar wind (1965-1991) and their association with ejecta, *J. Geophys. Res.*, *100*, 23,397–23,412, doi:10.1029/95JA02684.

Richardson, I. G., and H. V. Cane (2004), Identification of interplanetary coronal mass ejections at 1 AU using multiple solar wind plasma composition anomalies, *J. Geophys. Res.*, *109*, A09104, doi:10.1029/2004JA010598.

Richardson, I. G., and H. V. Cane (2010), Near-Earth Interplanetary Coronal Mass Ejections During Solar Cycle 23 (1996 - 2009): Catalog and Summary of Properties, *Sol. Phys.*, *264*, 189–237, doi:10.1007/s11207-010-9568-6.

Richardson, I. G., D. Berdichevsky, M. D. Desch, and C. J. Farrugia (2000), Solar-cycle variation of low density solar wind during more than three solar cycles, *Geophys. Res. Lett.*, *27*, 3761–3764, doi:10.1029/2000GL000077.

Riley, P., C. Schatzman, H. V. Cane, I. G. Richardson, and N. Gopalswamy (2006), On the Rates of Coronal Mass Ejections: Remote Solar and In Situ Observations, *ApJ*, *647*, 648–653, doi:10.1086/505383.

Riley, P., R. Lionello, Z. Mikić, and J. Linker (2008), Using Global Simulations to Relate the Three-Part Structure of Coronal Mass Ejections to In Situ Signatures, *ApJ*, *672*, 1221–1227, doi:10.1086/523893.

Rodgers, J. L., and W. A. Nicewander (1988), Thirteen ways to look at the correlation coefficient, *The American Statistician*, *42*(1), pp. 59–66.

Rodriguez, L., J. Woch, N. Krupp, M. FräNz, R. von Steiger, R. J. Forsyth, D. B. Reisenfeld, and K.-H. GlaßMeier (2004), A statistical study of oxygen freezing-in temperature and energetic particles inside magnetic clouds observed by Ulysses, *J. Geophys. Res.*, *109*, A01108, doi:10.1029/2003JA010156.

Rouillard, A. P. (2011), Relating white light and in situ observations of coronal mass ejections: A review, *Journal of Atmospheric and Solar-Terrestrial Physics*, *73*, 1201–1213, doi:10.1016/j.jastp.2010.08.015.

Russell, C. T., and A. A. Shinde (2003), ICME Identification from Solar Wind Ion Measurements, *Sol. Phys.*, *216*, 285–294, doi:10.1023/A:1026108101883.

Ruzmaikin, A., J. Feynman, and E. J. Smith (1997), Turbulence in coronal mass ejections, *J. Geophys. Res.*, *102*, 19,753–19,760, doi:10.1029/97JA01558.

Schmahl, E., and E. Hildner (1977), Coronal mass-ejections-kinematics of the 19 December 1973 event, *Sol. Phys.*, *55*, 473–490, doi:10.1007/BF00152588.

Schwenn, R., H. Rosenbauer, and K.-H. Muehlhaeuser (1980), Singly-ionized helium in the driver gas of an interplanetary shock wave, *Geophys. Res. Lett.*, *7*, 201–204, doi:10.1029/GL007i003p00201.

Sime, D. G., and A. J. Hundhausen (1987), The coronal mass ejection of July 6, 1980 - A candidate for interpretation as a coronal shock wave, *J. Geophys. Res.*, *92*, 1049–1055, doi:10.1029/JA092iA02p01049.

Singh, A. K., D. Siingh, and R. P. Singh (2010), Space Weather: Physics, Effects and Predictability, *Surveys in Geophysics*, *31*, 581–638, doi:10.1007/s10712-010-9103-1.

Skoug, R. M., et al. (1999), A prolonged He^+ enhancement within a coronal mass ejection in the solar wind, *Geophys. Res. Lett.*, *26*, 161–164, doi:10.1029/1998GL900207.

Smith, C. W., J. L'Heureux, N. F. Ness, M. H. Acuña, L. F. Burlaga, and J. Scheifele (1998), The ACE Magnetic Fields Experiment, *Space Sci. Rev.*, *86*, 613–632, doi:10.1023/A:1005092216668.

Smith, Z., W. Murtagh, and C. Smithtro (2004), Relationship between solar wind low-energy energetic ion enhancements and large geomagnetic storms, *Journal of Geophysical Research (Space Physics)*, *109*, A01110, doi:10.1029/2003JA010044.

St. Cyr, O. C., et al. (2000), Properties of coronal mass ejections: SOHO LASCO observations from January 1996 to June 1998, *J. Geophys. Res.*, *105*, 18,169–18,186, doi:10.1029/1999JA000381.

Stone, E. C., A. M. Frandsen, R. A. Mewaldt, E. R. Christian, D. Margolies, J. F. Ormes, and F. Snow (1998), The Advanced Composition Explorer, *Space Sci. Rev.*, *86*, 1–22, doi:10.1023/A:1005082526237.

Tandberg-Hanssen, E. (Ed.) (1995), *The nature of solar prominences*, *Astrophysics and Space Science Library*, vol. 199.

Telloni, D., R. D'Amicis, and E. Antonucci (2010), SOHO/UVCS Detection of Turbulence in a Coronal Mass Ejection, *Twelfth International Solar Wind Conference*, *1216*, 432–435, doi:10.1063/1.3395896.

Temmer, M., A. M. Veronig, E. P. Kontar, S. Krucker, and B. Vršnak (2010), Combined STEREO/RHESSI Study of Coronal Mass Ejection Acceleration and Particle Acceleration in Solar Flares, *ApJ*, *712*, 1410–1420, doi:10.1088/0004-637X/712/2/1410.

Tsurutani, B. T., E. J. Smith, W. D. Gonzalez, F. Tang, and S. I. Akasofu (1988), Origin of interplanetary southward magnetic fields responsible for major magnetic storms near solar maximum (1978-1979), *J. Geophys. Res.*, *93*, 8519–8531, doi:10.1029/JA093iA08p08519.

Tylka, A. J., C. M. S. Cohen, W. F. Dietrich, M. A. Lee, C. G. Maclennan, R. A. Mewaldt, C. K. Ng, and D. V. Reames (2005), Shock Geometry, Seed Populations, and the Origin of Variable Elemental Composition at High Energies in Large Gradual Solar Particle Events, *ApJ*, *625*, 474–495, doi:10.1086/429384.

van der Holst, B., W. B. Manchester, IV, R. A. Frazin, A. M. Vásquez, G. Tóth, and T. I. Gombosi (2010), A Data-driven, Two-temperature Solar Wind Model with Alfvén Waves, *ApJ*, *725*, 1373, doi:10.1088/0004-637X/725/1/1373.

Veenadhari, B., R. Selvakumaran, R. Singh, A. K. Maurya, N. Gopalswamy, S. Kumar, and T. Kikuchi (2012), Coronal mass ejection-driven shocks and the associated sudden commencements/sudden impulses, *Journal of Geophysical Research (Space Physics)*, *117*, A04210, doi:10.1029/2011JA017216.

von Rosenvinge, T. T., et al. (1995), The Energetic Particles: Acceleration, Composition, and Transport (EPACT) investigation on the WIND spacecraft, *Space Sci. Rev.*, *71*, 155–206, doi:10.1007/BF00751329.

von Steiger, R. (2008), The solar wind throughout the solar cycle, in *The Heliosphere through the Solar Activity Cycle*, edited by A. Balogh, L. J. Lanzerotti, and S. T. Suess, p. 41, Praxis Publishing, doi:10.1007/978-3-540-74302-6_3.

von Steiger, R., N. A. Schwadron, L. A. Fisk, J. Geiss, G. Gloeckler, S. Hefti, B. Wilken, R. F. Wimmer-Schweingruber, and T. H. Zurbuchen (2000), Composition of quasi-stationary solar wind flows from Ulysses/Solar Wind Ion Composition Spectrometer, *J. Geophys. Res.*, *105*, 27,217–27,238, doi:10.1029/1999JA000358.

von Steiger, R., T. H. Zurbuchen, and D. J. McComas (2010), Oxygen flux in the solar wind: Ulysses observations, *Geophys. Res. Lett.*, *37*, L22101, doi:10.1029/2010GL045389.

Vourlidas, A., S. T. Wu, A. H. Wang, P. Subramanian, and R. A. Howard (2003), Direct Detection of a Coronal Mass Ejection-Associated Shock in Large Angle and Spectrometric Coronagraph Experiment White-Light Images, *ApJ*, *598*, 1392–1402, doi:10.1086/379098.

Vourlidas, A., R. A. Howard, E. Esfandiari, S. Patsourakos, S. Yashiro, and G. Michalek (2010), Comprehensive Analysis of Coronal Mass Ejection Mass and Energy Properties Over a Full Solar Cycle, *ApJ*, *722*, 1522, doi:10.1088/0004-637X/722/2/1522.

Vršnak, B., D. Sudar, and D. Ruždjak (2005), The CME-flare relationship: Are there really two types of CMEs?, *A&A*, *435*, 1149–1157, doi:10.1051/0004-6361:20042166.

Webb, D. F., and T. A. Howard (2012), Coronal Mass Ejections: Observations, *Living Reviews in Solar Physics*, *9*, 3.

Webb, D. F., and A. J. Hundhausen (1987), Activity associated with the solar origin of coronal mass ejections, *Sol. Phys.*, *108*, 383–401, doi:10.1007/BF00214170.

Wenzel, K. P., R. G. Marsden, D. E. Page, and E. J. Smith (1992), The ULYSSES Mission, *A&AS*, *92*, 207.

Wiik, J. E., B. Schmieder, T. Kucera, A. Poland, P. Brekke, and G. Simnett (1997), Eruptive prominence and associated CME observed with SUMER, CDS and LASCO (SOHO), *Sol. Phys.*, *175*, 411–436, doi:10.1023/A:1004925024794.

Wilhelm, K., E. Marsch, B. N. Dwivedi, D. M. Hassler, P. Lemaire, A. H. Gabriel, and M. C. E. Huber (1998), The Solar Corona above Polar Coronal Holes as Seen by SUMER on SOHO, *ApJ*, *500*, 1023, doi:10.1086/305756.

Wilhelm, K., et al. (1995), SUMER - Solar Ultraviolet Measurements of Emitted Radiation, *Sol. Phys.*, *162*, 189–231, doi:10.1007/BF00733430.

Zurbuchen, T. H., and I. G. Richardson (2006), In-Situ Solar Wind and Magnetic Field Signatures of Interplanetary Coronal Mass Ejections, *Space Sci. Rev.*, *123*, 31–43, doi:10.1007/s11214-006-9010-4.

Zurbuchen, T. H., L. A. Fisk, S. T. Lepri, and R. von Steiger (2003), The Composition of Interplanetary Coronal Mass Ejections, in *Solar Wind Ten*, *American Institute of Physics Conference Series*, vol. 679, edited by M. Velli, R. Bruno, F. Malara, and B. Bucci, pp. 604–607, doi:10.1063/1.1618667.

Zurbuchen, T. H., R. von Steiger, J. Gruesbeck, E. Landi, S. T. Lepri, L. Zhao, and V. Hansteen (2012), Sources of Solar Wind at Solar Minimum: Constraints from Composition Data, *Space Sci. Rev.*, *172*, 41–55, doi:10.1007/s11214-012-9881-5.

Zwickl, R. D., J. R. Asbridge, S. J. Bame, W. C. Feldman, and J. T. Gosling (1982), He/+/ and other unusual ions in the solar wind - A systematic search covering 1972-1980, *J. Geophys. Res.*, *87*, 7379–7388, doi:10.1029/JA087iA09p07379.